HOKKAIDO UNIVERSITY

DOCTORAL THESIS

Mathematical Study on Fluorescence Diffuse Optical Tomography — Recovering the Distribution of Fluorophores Using Cuboid Approximation

(蛍光拡散トモグラフィの数理的研究
— 直方体近似を用いた蛍光体分布同定)

Chunlong SUN

A thesis submitted for the degree of Doctor of Philosophy

in the

Department of Mathematics
Graduate School of Science

2020 June

HOKKAIDO
UNIVERSITY

HOKKAIDO UNIVERSITY

Abstract

Department of Mathematics
Graduate School of Science

Doctor of Philosophy

Mathematical Study on Fluorescence Diffuse Optical Tomography — Recovering the Distribution of Fluorophores Using Cuboid Approximation

by Chunlong SUN

In this thesis the time-domain fluorescence diffuse optical tomography (FDOT) is theoretically and numerically investigated based on analytical expressions for a three space dimensional diffusion equation model (DE model). Physically the radiative transfer equation model (RTE model) is a better model to describe the physical process behind the measurement of the FDOT. We carefully analyzed the derivation of the DE model from RTE model to consider about the modelling error. Since the distance between the source and detectors are short, the initial boundary value problem for the DE can be considered in the half space. Here there are two diffusion equations coupled in one of its source term. Each of them describes the emission of angularly averaged excited photon density (i.e. excited light) and that of emitted photon density (i.e. emitted light). Usually for the excited light the distribution of fluorophores in biological tissue is ignored and have the so called linearized DE model. The emission light is analytically calculated by solving an initial boundary value problem for coupled diffusion equations in the half space. Based on the analytic expression of the solution to this initial boundary value problem, we establish an error estimate for linearizing the DE model.

Our FDOT is to recover the distribution of fluorophores in biological tissue based on the linearized DE model by using the time-resolved measurement data on the boundary surface. We theoretically analyzed the identifiability of this inverse absorption problem.

Aiming a fast and robust algorithm for our FDOT inverse problem, we identify the location of a fluorescence target by assuming that it has a cuboidal shape neglecting its precise shape. We proposed and verified our inversion strategy which is a combination of theoretical arguments and numerical arguments for an inversion, which enables to obtain a stable inversion and accelerate the speed of convergence. Its effectivity and performance were tested numerically using simulated data and experimental data obtained from ex vivo beef phantoms.

Acknowledgements

First, the author is gratitude to Prof. Hideo Kubo, his supervisor as well as mentor at Hokkaido University, who has furnished selfless instructions and successive encouragements to the author.

Second, I would like to show my greatest appreciation to Prof. Gen Nakamura (Professor Emeritus, Hokkaido University) and Prof. Goro Nishimura (Research Institute for Electronic Science, Hokkaido University), who are also my advisers and gave me a lot of advices to write this thesis. The author has benefited a lot not only from their conviction and attitude toward academic researches, but also from their foresight and enthusiasm on multidisciplinary collaborations.

I am also grateful to the faculty members of Department of Mathematics, Graduate School of Science, Hokkaido University, whose densely academic atmosphere and excellent work attitude has kept impressing the author during his doctoral program. The author also appreciates the helpful communications with Prof. Nagayama and those related to his laboratory, especially Dr. Yikan Liu.

Next, the author would like to give heartfelt thanks to his colleagues, who share their expertise and diligence in pursuit of high qualities of the joint works. Chapter 2–3 are mainly based on the yet unpublished joint paper [65] with Prof. Jijun Liu, the author's supervisor at Southeast University, who provided him with the opportunity to study in Japan and has given consistent cares. The author also thanks members of the inverse problem group in Southeast University, especially Prof. Haibing Wang, Dr. Liyan Wang and Dr. Min Zhong, for valuable suggestions. Chapter 4 and a part of Chapter 6 are based on the joint paper [17] with Dr. Manabu Machida (Hamamatsu University School of Medicine) and Dr. Y. Jiang (Shanghai University of Finance and Economics).

The author has been financially supported by Grant-in-Aid for Scientific Research of the Japan Society for the Promotion of Science and Japan Student Services Organization (JASSO, Japan). The author benefited a lot from Prof. Masahiro Yamamoto (The University of Tokyo) during his stay in The University of Tokyo and A3 meeting in Okinawa.

Last but not least, the author is deeply indebted to his beloved family, especially his parents, for their warm considerations and great supports all through these years. They have raised up the author to overcome difficulties on his road to advance.

—— Chunlong Sun, 2020,02,02

Contents

Abstract **iii**

Acknowledgements **v**

1 Introduction to FDOT **1**
- 1.1 Fluorescence Diffuse Optical Tomography 1
- 1.2 Photon Transport Models in Strong Scattering Media 2
- 1.3 FDOT as an Ill-posed Inverse Problem 4
- 1.4 Summary of Thesis 8

2 Linearized Diffusion Equation Model **11**
- 2.1 From RTE Model to Linearized DE Model 11
  - 2.1.1 RTE model and our FDOT 11
  - 2.1.2 Derivation of the diffusion equation 14
  - 2.1.3 Boundary condition for the diffusion approximation 15
  - 2.1.4 Nonlinear DE model and its linearization 16
- 2.2 Error Estimations for Model Approximation 19
  - 2.2.1 Analytical solutions using Green functions 19
  - 2.2.2 Error estimation for excitation 21
  - 2.2.3 Error estimation for inversion solutions 23
- 2.3 Numerical Verifications for Model Approximation 26
- 2.4 Chapter Summary 30

3 Parameter Identification for FDOT **31**
- 3.1 Identifiability of the Absorption Coefficient 31
- 3.2 Long-time Behavior of Emission Light 35
- 3.3 Chapter Summary 36

4 FDOT Using Cuboid Approximation **37**
- 4.1 The Idea of Cuboid Approximation 37
  - 4.1.1 Analytical solution to real experiment 38
  - 4.1.2 Fast solver by assuming cuboid 39
- 4.2 Testing the Rationality of Cuboid Approximation 43
- 4.3 Simulation and Property of Measured Data 45
- 4.4 Chapter Summary 47

5 Local Analysis for FDOT Using Cuboid Approximation **49**
- 5.1 The Determinant Condition 50
- 5.2 Local Solvability and Its Lipschitz Stability 57
- 5.3 Convergence of Levenberg-Marquardt method 58
- 5.4 Numerical implementations 60
- 5.5 Chapter Summary 62

6 Inversion Strategy and Numerical Inversions Using Simulation Data 63
6.1 Step-wise Inversion Strategy 63
6.2 Numerical Inversion Using Simulation Data 64
6.2.1 Good sets of measurements 64
6.2.2 Results of inversion for ellipsoidal target 66
6.2.3 Results of inversion for cylindrical target 71
6.3 Chapter Summary 73

7 Numerical Inversions Using Experimental Data 75
7.1 Experimental Demonstration with a Beef Phantom 75
7.2 Results of Inversion for Beef Experiment I 76
7.3 Results of Inversion for Beef Experiment II 81
7.4 Chapter Summary 83

8 Conclusion and Remark 85

A The Gradient of Zero-lifetime Emission 87

Bibliography 88

List of Figures

1.1 Light propagation in turbid media. 2

2.1 Horizontal projection of the configuration: the red circle with center $(0, 0)$ is the projection of a sphere target to the boundary $\partial\Omega$, the boundary source locates at xs, and the measurements are taken at points $x1$ and $x2$. 27
2.2 Comparisons of two sides of (2.3.1) at two points x_1 and x_2. Left: Distributions of two sides at two points after taking logarithm; Right: Relative error at two points. 28
2.3 Comparisons of two sides of (2.3.2) at two points x_1 and x_2. Left: Distributions of two sides at two points after taking logarithm; Right: Relative error at two points. 29

4.1 (a) The values of $\lim_{s\to 0_+} \widetilde{u}_1(x_{d1}, x_{s1}, t, s; a_1, b_1)$ with fixed $x_{d1} = 1$ and $x_{s1} \in [0, 10]$. (b) The values of $\lim_{s\to t_-} \widetilde{u}_1(x_{d1}, x_{s1}, t, s; a_1, b_1)$ with fixed $x_{s1} = 1$ and $x_{d1} \in [0, 10]$. 42
4.2 The spherical target and three cubic targets approximated to the spherical target; Cube1 is the inscribed cubic target, Cube2 is the cubic target which has same volume and Cube3 is the circumscribed cubic target. 43
4.3 TPSFs (i.e. temporal profile of the emission) corresponding to the spherical target indicated by circles and three approximate cube targets indicated by lines. Two figures are corresponding to the different detection points at (0,0,0) and (19,-11, 0). 44
4.4 (a) The positions of four sources (small red circles) and twelve detectors (small blue points). The big red circle is the projection of spherical target to the boundary. (b), (c) are the TPSFs (the logarithm value) to different detectors corresponding to source S_1. 45
4.5 (a) Scan the S-D pair on the boundary $\partial\Omega$; The red rectangular shape shows the fluorescence target. (b) The emission intensities given by (4.3.1) with different position $x1$. 46
4.6 TPSFs and three indexes of emission light with different S-D pairs. 46
4.7 The distribution of emission intensity with different S-D pairs. 47

5.1 (a) A set of S-D pairs and the projection of cuboidal target to $\partial\Omega$; (b) The rank of sensitivity matrix with different selected 7 S-D pairs. 61
5.2 The sensitivities on different parameters on t_{start} and t_{peak}. 61

6.1 (Left) The holder of source-detector pairs at a position P_1; (Right) All positions on the boundary surface. 65
6.2 The S-D pairs corresponding to the positions of holder at P1, P3, P5 and P7 in Ex.6.1, respectively. 67
6.3 The prior information Γ on the boundary $\partial\Omega$ in Ex.6.1. 67
6.4 The 10-times recoveries with different noise levels. 69

6.5 The different views of exact ellipsoidal target (red) and average recovered cube (blue) ($\epsilon = 5\%$). . . . 69
6.6 The different views of exact ellipsoidal target (red) and recovered cuboid (blue) in Ex.1 ($\epsilon = 5\%$). (a) Front view; (b) Vertical view; (c) Side view. . . 70
6.7 The recovered width, length and thickness at each recovery of the 100-time recoveries. The black lines are the corresponding mean of the 100-time recoveries. . . . 71
6.8 The relative error for width, length and thickness at each recovery of the 100-time recoveries. . . . 71
6.9 The TPSFs $\widetilde{u}_m^{\mathrm{cylinder}}(t,\omega)$ (blue line) and $\widetilde{u}_m(\mathbf{a}_{\mathrm{noisy}}^{\mathrm{cuboid}})(t,\omega)$ (red line) to two S-D pairs. Here $\mathbf{a}_{\mathrm{noisy}}^{\mathrm{cuboid}}$ was recovered by the noisy data with $\epsilon = 5\%$. . . 72

7.1 The block diagram of the experiment and the geometry of the fibers. . . . 75
7.2 The IRF measurement adapter. The adapter holds some attenuation filters and a small diffuser to homogenize the light. . . . 76
7.3 Beef experiment I: (Left) A cylinder of fluorescence target was placed inside the beef. (Middle) The cylinder was embedded at depth about 16 mm. (Right) Boundary measurements were performed using optical fibers attached to a holder on the top of beef. . . . 77
7.4 The positions of S-D pairs in Beef Experiment I. Red small disks show sources and blue circles show detectors. The sources and detectors for the holder at position P1 (i.e, 1) are distinguished by purple squares. . . . 77
7.5 The positions of holder at P3, P4, P13 and P16 in Experiment I. . . . 78
7.6 TPSFs (the logarithm value) with the position of holder at P1, P3, P5, P7, P8, P13, P15 and P16. . . . 79
7.7 The initial guess (small yellow cube) and recovery (big red cube) in Step 2. 79
7.8 The initial guess (red cube obtained from Step 2) and recovery (green cuboid) in Step 3. . . . 80
7.9 Schematic figure of measurements on the boundary. Red small disks show sources and blue circles show detectors. The source-detector pairs are denoted by pink lines. The green rectangle shows the position of the reconstructed tube projected on the x-y(x_1-x_2) plane. . . . 80
7.10 Beef experiment II: (Left) A cylindrical fluorescence target was inserted in the beef meat. (Middle) The cylinder was embedded at depth about $x_3 = 10$ mm. (Right) Scanned on the meat surface to obtain the boundary measurements. . . . 81
7.11 The TPSFs (the logarithm value) to above 10 S-D pairs given in (7.3.1). . 82
7.12 Red disks show the positions of holder. The blue and green rectangular are the positions of the expected cylinder target and recovered cuboid projected on the boundary plane, respectively. . . . 83

List of Tables

1.1 Error distribution with different discrete level n. 6

6.1 The emission intensities ($\times 10^{-8}$) with different S-D pairs in Ex. 6.1. 66
6.2 Recoveries using different initial guesses in Step 2 for Ex. 6.1 ($\epsilon = 5\%$). . . 68
6.3 The average recoveries with different noise level ϵ in Step 2 for Ex. 6.1. . . 68
6.4 Recoveries from exact measured data in Step 3 for Ex.6.1 ($\epsilon = 0$). 69
6.5 Recoveries from noisy measured data in Step 3 for Ex. 6.1 ($\epsilon = 5\%$). . . . 70
6.6 The 100-time recoveries from different noisy data sets with $\epsilon = 1\%$ for Ex.6.1. 70
6.7 Recoveries from noisy measured data in Step 3 for Ex.6.2 72
6.8 The 100-time recoveries from different noisy data sets with $\epsilon = 1\%$ for Ex.6.2. 73

7.1 The emission intensities ($\times 10^{3}$ counts) with different S-D pairs. 78
7.2 The reconstructed results with different initial guesses. 79
7.3 The exact cylinder and recovered cuboid (unit: mm). 80
7.4 The positions of the holder in Beef Experiment II (unit: mm). 81
7.5 The exact cylinder and recovered cuboid (unit: mm). 83

List of Abbreviations

FDOT	**F**luorescence **D**iffuse **O**ptical **T**omography
DOT	**D**iffuse **O**ptical **T**omography
RTE	**R**adiative **T**ransfer **E**quation
DE	**D**iffusion **E**quation
NIR	**N**ear-infrared
CT	**C**omputed **T**omography
MRI	**M**agnetic **R**esonance **I**maging
CW	**C**ontinuous **W**ave
FD	**F**requency **D**omain
TD	**T**ime **D**omain
LM	**L**evenberg-**M**arquardt
MC	**M**onte **C**arlo
TPSFs	**T**emporal **P**oint **S**pread **F**unctions
IRF	**I**nstrumental **R**esponse **F**unction
S-D	**S**ource-**D**etector
SVD	**S**ingular **V**alue **D**ecomposition
ICG	**I**ndocyanine **G**reen

Physical Constants

In Simulation Examples:

Speed of Light in the Medium	$c = 0.219\,\mathrm{mm/ps}$
The Quantum Efficiency of the Fluorescence	$\gamma = 1$
Absorption of the Medium	$\mu_a = 0.01\,\mathrm{mm}^{-1}$
Scattering of the Medium	$\mu_s = 10\,\mathrm{mm}^{-1}$
Average Scattering Cosine	$g = 0.9$
Reduced Scattering Coefficient	$\mu_s' = 1.0\,\mathrm{mm}^{-1}$
Fluorescence Lifetime	$\tau = 0\,\mathrm{ps}$
Photon Diffusion Coefficient	$D = 1/3\,\mathrm{mm}^2/\mathrm{ps}$
Robin coefficient	$\beta = 0.549\,\mathrm{mm}^{-1}$

In Beef Experiments:

Speed of Light in the Medium	$c = 0.219\,\mathrm{mm/ps}$
The Quantum Efficiency of the Fluorescence	$\gamma = 1$
Absorption of the Medium	$\mu_a = 0.023\,\mathrm{mm}^{-1}$
Reduced Scattering Coefficient	$\mu_s' = 0.92\,\mathrm{mm}^{-1}$
Photon Diffusion Coefficient	$D = 0.362\,\mathrm{mm}^2/\mathrm{ps}$
Fluorescence Lifetime	$\tau = 600\,\mathrm{ps}$
Robin coefficient	$\beta = 0.5\,\mathrm{mm}^{-1}$

List of Symbols

symbol	*definition*	*name*
Ω		half space
Ω_0		support of fluorophore
$\partial\Omega$		boundary surface
$\mathbb{R}$		real number set
$\mathbb{R}^n$		n-dimensional real number space
$\mathbb{S}^2$		unit sphere
x_d		position of detector
x_s		position of excitation source
Φ		radiant intensity
Φ_e		radiant intensity of excitation
Φ_m		radiant intensity of emission
U		photon density (or fluence rate)
U_e		photon density of excitation for nonlinear DE model
U_m		photon density of of emission for nonlinear DE model
u_e		photon density of excitation for linearized DE model
u_m		photon density of emission for linearized DE model
$\widetilde{u}_m$		photon density of zero-lifetime emission
μ_a		absorption coefficient of medium
μ_f		absorption coefficient of fluorescence
μ_s		scattering coefficient of medium
g		anisotropy parameter (or average scattering cosine)
μ_s'	$(1-g)\mu_s$	reduced scattering coefficient
D	$\frac{1}{3\mu_s'}$	photon diffusion coefficient
$\mathbf{J}$	$-D\nabla U$	photon flux
θ		angular direction variable (or solid angle)
γ		the quantum efficiency of the fluorescence
τ		fluorescence lifetime
c		speed of light in the medium
$\eta(\theta,\theta')$		scatter phase function from direction θ into θ'
ν		unit outward normal vector
R		Fresnel reflection coefficient
β		Robin coefficient
erf		error function
erfc		complementary error function
G		functional solution to heat equation
K		Green function to diffusion equation
$\widetilde{R}$		response function
$\mathbf{I}$		emission intensity
ω		position of source-detector pair
t_{peak}		peak time at which the photon density is strongest
C		some positive constant

Chapter 1

Introduction to FDOT

This chapter is intended as an introduction into the basic characteristics on Fluorescence Diffuse Optical Tomography (FDOT). As a medical imaging technique, we give a short description of its background in section 1.1 and the photon transfer model in section 1.2. As an ill-posed inverse problem, we give the concept of ill-posedness and an introduction to regularization methods commonly used for treating ill-posed problems in section 1.3. We summarize the main results of this thesis in section 1.4.

1.1 Fluorescence Diffuse Optical Tomography

Fluorescence imaging using short wavelength *near-infrared* (NIR) light (700–1000 nm) is rapidly gaining acceptance as an important diagnostic and monitoring tool of symptoms in medical applications [1–4]. The *fluorescence contrast agents* allow tracking non-invasively and quantitatively specific molecular events or provides some clinically important information *in vivo*. Fluorescence imaging is generally high-sensitive and there are some additional advantages in *NIR fluorescence imaging*, such as the weak background from tissue and the longer penetration depth compared with those in the visible wavelength region. More precisely, in tissue, light is strongly attenuated in the visible region (450 to 700 nm) and can penetrate less than one centimeter, but at NIR wavelengths (700 to 1000 nm) the *absorption* is significantly lower and with sensitive instrumentation it is possible to detect light that has traversed up to 8 centimeters of tissue.

However, the NIR fluorescence imaging is still limited in a region near the surface of tissue because the *strong scattering* significantly blurs images and the absorption attenuates the fluorescence intensity. In the clinical applications, the imaging in a *thick* (> 1 cm) or *large volume tissue* ($>$ few 10 cm^3) is highly demanded because the clinically important region is not limited on the surface. Thus, the imaging technique under the strong scattering condition is essential to extend the optical imaging method in many of the clinical applications. In this condition, the light propagation is considered as an energy dissipation by the random scattering and the spatial information is significantly lost, resulting the *image blurring*. Thus, the *three-dimensional image reconstruction* of the fluorescence from the blurred images is essential, which is very important but really challenging.

In order to recover the three-dimensional distribution of the fluorophores in strong scattering media, it is necessary to consider an *inverse problem* (We will explain the meaning of "inverse problem" later) based on a *photon transport model* which leads the so-called *diffuse optical tomography* (DOT) [25, 26]. For the fluorescence, as shown in Figure 1.1, two physical processes are coupled, namely, *excitation* and *fluorescence* (*emission*). The excitation photons injected at the boundary of the medium propagate to the fluorophores and then some photons are absorbed by them which excite the fluorophore molecules. After a moment of the absorption, the fluorophores emit other photons, fluorescence, at more longer wavelength than the wavelength of the excitation photons, and then these again propagate until they are observed by the detectors at the surface of the medium. Therefore, two kinds of the propagation, excitation and fluorescence (emission), are involved and they are described by the photon transport model.

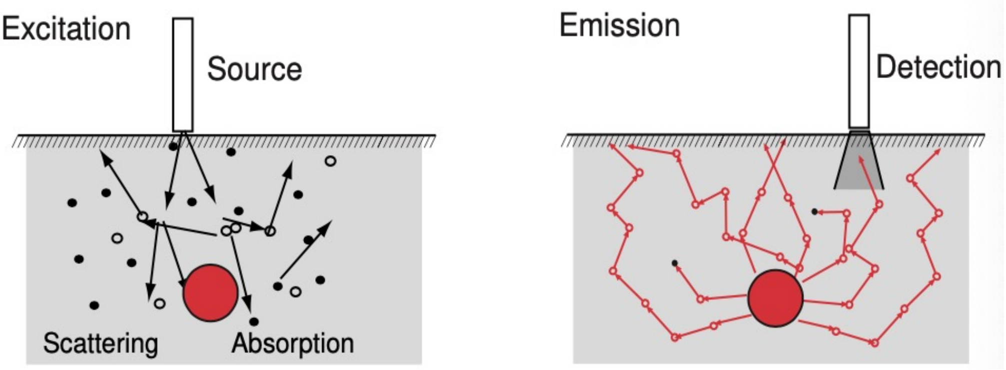

FIGURE 1.1: Light propagation in turbid media.

Fluorescence diffuse optical tomography (FDOT) is one type of optical tomography which makes use of fluorescence light from fluorophore. It aims to recover the fluorophores quantitatively from some measurement specified on the medium surface, which is an inverse problem. FDOT should be inexpensive and portable compared to *X-ray computed tomography* (CT), *magnetic resonance imaging* (MRI) and *positron emission tomography* (PET) and therefore could be an important diagnostic and monitoring tool of symptoms at the bedside.

1.2 Photon Transport Models in Strong Scattering Media

Light propagation is rigorously described by *Maxwell's equations* that describe the relation of electric and magnetic waves in space and time. However, because the wave property of the photon is lost by multiple scattering in strongly turbid medium such as biological tissue, the photon propagation through turbid media for both excitation and emission are governed by the Boltzmann radiative transfer equation or shortly the *radiative transfer equation* (RTE) [18–21], which is originally developed to describe the light energy propagations in turbulent atmosphere [18, 21] and has been generalized to describe different kinds of waves in random inhomogeneous medium [20]. We start from the *linearized Boltzmann radiative transport equation.*

Linearized Boltzmann radiative transfer

The propagation of photon in scattering media can be described with

$$\begin{aligned}\frac{1}{c}\frac{\partial}{\partial t}\Phi(x,\theta,t) &= -\theta\cdot\nabla\Phi(x,\theta,t) - (\mu_a+\mu_f+\mu_s)\Phi(x,\theta,t)\\ &\quad + \mu_s\int_{\mathbb{S}^2}\eta(\theta,\theta')\Phi(x,\theta',t)\,\mathrm{d}\theta' + \widetilde{S}(x,\theta,t),\end{aligned} \tag{1.2.1}$$

where $\Phi(x,\theta,t)$ is the *radiant intensity* (i.e., angular dependent density) at x in time t with θ is a unit vector pointing in the direction of interest. $\widetilde{S}(x,\theta,t)$ is the source term. The absorption and scattering coefficients of medium, μ_a and μ_s, are the inverses of the mean free paths for scattering and absorption, respectively. μ_f denotes the absorption coefficient of the fluorophores inside the medium, and c is the speed of photon inside the medium. The scattering phase function $\eta(\theta\cdot\theta')$ describing the probability that a photon traveling in direction θ is scattered within the unit solid angle around the direction θ', is given by 3-dimensional Henyey-Greenstein function

$$\eta(\theta,\theta') := \frac{1-g^2}{4\pi(1+g^2-2g\theta\cdot\theta')^{3/2}}, \tag{1.2.2}$$

where the anisotropy parameter (or average scattering cosine) g is the mean cosine of the scattering angle, i.e., $g := \int_{\mathbb{S}^2}(\theta\cdot\theta')\eta(\theta\cdot\theta')\,\mathrm{d}\theta$ and hence $-1 < g < 1$.

We recognize the left hand side of (1.2.1) as the change of the radiant intensity in time. The equation says that this change should equal to the sum of the right hand terms [8].

The first term in the right hand side in (1.2.1) is negative so it decreases the number of photons. This term represents the *out-flowing* photons due to a local gradient (i.e., "true" diffusion). The second term is also negative and also decreases the photon density. This term represents the loss of photons in direction θ either due to the absorption or scattering. The third term represents the photons that are scattered into the volume at direction θ and the fourth term represents a light source that creates new photons. So the RTE simply states that the sum of these terms equals to the change in time of the radiant intensity.

Although the derivation of the RTE was not difficult from a physical point of view (see the Appendix A in [8]), this RTE system is still considered as a phenomenological and heuristic theory that lacks a rigorous mathematical formulation capable to take into account all the physical effects involved in light propagations [19]. On the other hand, solving RTE requires a large amount of computations. Therefore there are practical requirements on developing the approximate model of RTE for fluorescence imaging, for which a cheap solver is available.

Diffusion approximation in radiative transfer

The *diffusion equation* (DE) [19, 23, 24] is the most popular and most useful approximation to the RTE, which was shown a sufficiently good approximation to the RTE but much easier to calculate, and therefore has been applied in engineering communities for a long time. When scattering is much stronger than absorption, the radiant intensity, Φ, can be expressed as an isotropic fluence rate U (*photon density*) plus a small directional flux $\mathbf{J}$ (*photon flux*) which is the so-called P_1-*approximation*, and transport equation (1.2.1) reduces to a diffusion equation.

We write the radiant intensity as

$$\Phi(x,\theta,t) = \frac{1}{4\pi}U(x,t) + \frac{3}{4\pi}\theta\cdot\mathbf{J}(x,t), \quad \theta\in\mathbb{S}^2, \tag{1.2.3}$$

with

$$U(x,t) := \int_{\mathbb{S}^2}\Phi(x,\theta,t)\,\mathrm{d}\theta, \;\; \mathbf{J}(x,t) := \int_{\mathbb{S}^2}\theta\cdot\Phi(x,\theta,t)\,\mathrm{d}\theta, \tag{1.2.4}$$

where $\mathbb{S}^2 := \{x\in\mathbb{R}^3, \|x\| = 1\}$.

Notice the physical fact $\frac{\partial}{\partial t}|\mathbf{J}| \ll c(\mu_a+\mu_f+\mu_s)|\mathbf{J}|$. Under the assumption that sources $\widetilde{S}(x,\theta,t)$ are isotropic, we have

$$\mathbf{J}(x,t) = -D(x)\nabla U(x,t) \tag{1.2.5}$$

with the *photon diffusion coefficient*, $D(x)$, by

$$D(x) := \frac{1}{3(\mu_a + \mu_f + \mu_s')} \equiv \frac{1}{3\mu_s'}, \tag{1.2.6}$$

where the reduced scattering coefficient is defined by $\mu_s' := \mu_s(1-g)$ with g is the anisotropy parameter. Here we used the fact that $\mu_a, \mu_f \ll \mu_s'$ due to the strong scattering in medium. Then based on (1.2.3), we can derive the *diffusion equation* from RTE as [19, 26, 30]

$$\left[\frac{1}{c}\frac{\partial}{\partial t} - D\Delta + \big(\mu_a(x) + \mu_f(x)\big)\right] U(x,t) = S_0(x,t), \tag{1.2.7}$$

where S_0 is the isotropic source. The detail derivation from (1.2.1) to (1.2.7) can be found in [19, 31, 32] or Chapter 2.

In addition, by ignoring μ_f in (1.2.7), one has the following simplified *diffusion equation*

$$\left[\frac{1}{c}\frac{\partial}{\partial t} - D\Delta + \mu_a(x)\right] u(x,t) = S_0(x,t), \tag{1.2.8}$$

which plays a very important role in diffuse optical tomography problems and will be the photon transport model in the rest of this thesis. (1.2.8) can be considered the approximate model of (1.2.7). However, as far as we know, there is no rigorous mathematical analysis of the error due to the approximation from (1.2.7) to (1.2.8).

In this thesis, we will analyze the error estimations for such approximations from the view of mathematics. Due to our experimental setup, we simplify the geometric setup which allows to use an analytic solution of DE. Then, based on these analytic expressions of excitation and emission, we will establish the estimations of errors on the excitation field and the solution to the *inverse problem*, which ensures the reasonability of the simplification from (1.2.7) to (1.2.8) (see Theorem 2.1 and Theorem 2.2 in Chapter 2). Moreover, we also qualitatively validate the approximation from RTE to DE in section 2.3.

1.3 FDOT as an Ill-posed Inverse Problem

The general task of *image reconstruction* is to compute an image from the specified measured data. Image reconstruction can be regarded as a parameter identification problem or so called *inverse problem* as we mentioned before, which is generally *ill-posed*. Now we are ready to give the mathematical descriptions for *inverse problems* and *ill-posed problems*.

Inverse problems and ill-posed problems

Suppose the data is described by a general vector h and that the image can be described by a general vector z. Suppose that we also have a physical model $\mathcal{P}$ that describes the relation between h and z, that is,

$$\mathcal{P}z = h. \tag{1.3.1}$$

The *forward problem* is to determine the data h for a given image z within the domain $\mathcal{Z}$ of $\mathcal{P}$, whereas the *inverse problem* is to reconstruct the image z from the data h for a given model $\mathcal{P}$.

Inverse problems are hard to be defined. According to Keller [77] a pair of problems are defined as inverse to each other, if the formulation (i.e.,the data) of each of them requires complete or partial knowledge of the solution of the other problem. Thus inverse problems come paired with direct problems. We may say inverse problems are looking for images or causes of an observed data or desired effect, which can be characterized by three points: *large scale*, *nonlinear* and *ill-posedness*.

The forward problems are usually well-posed and have been intensively studied. In the sense of Hadamard, we say a mathematical problem is well-posed if it satisfies following conditions [6, 7].

Definition 1.1. (WELL-POSEDNESS) *Let $\mathcal{Z}$ and $\mathcal{H}$ be normed spaces and let $\mathcal{P} : \mathcal{Z} \to \mathcal{H}$ be a (possibly nonlinear) continuous operator from $\mathcal{Z}$ into $\mathcal{H}$. The problem $h = \mathcal{P}z$ is well-posed in the sense of Hadamard if the following three conditions are satisfied:*

- *1. There exists a solution $z \in \mathcal{Z}$ for any $h \in \mathcal{H}$ such that $\mathcal{P}z = h$ (existence).*
- *2. There exists at most one solution $z \in \mathcal{Z}$ for any $h \in \mathcal{H}$ with $\mathcal{P}z = h$ (uniqueness).*
- *3. Any sequence $z_1, z_2, \cdots \in \mathcal{Z}$ with $\mathcal{P}z_n \to \mathcal{P}z$ for $n \to \infty$ implies $z_n \to z, n \to \infty$ (stability).*

A problem for which at least one of the three conditions above fails to hold is termed ill-posed.

The first two conditions ensure the unique existence of a solution to the problem, which can, in theory, be accomplished by choosing the domain and range satisfying $\mathcal{P}(\mathcal{Z}) = \mathcal{H}$, i.e., the model $\mathcal{P}$ is fully characterized. Here we focus on the stability requirement, which probably is the most important condition. If the solution does not depend continuously on the data, then unavoidable perturbations in the data may lead to uncontrolled perturbations in the solution.

The following two simple examples illustrate the typical problems encountered when solving ill-posed inverse problems.

Example 1.1. (Cauchy Problem for Laplace Equations) *Consider the Cauchy problem for two-dimensional Laplace equation [6]*

$$\begin{cases} \Delta u(x,y) = \frac{\partial^2 u(x,y)}{\partial x^2} + \frac{\partial^2 u(x,y)}{\partial y^2} = 0, \quad (x,y) \in \mathbb{R} \times [0, +\infty), \\ u(x,0) = a(x), \quad x \in \mathbb{R}, \\ \frac{\partial u}{\partial y}(x,0) = b(x), \quad x \in \mathbb{R}. \end{cases} \tag{1.3.2}$$

Let $a(x) = 0$ and $b(x) = \frac{1}{n}\sin(nx)$. Then above Cauchy problem admits unique solution

$$u(x,y) = \frac{1}{n^2}\sin(nx)\sinh(ny). \tag{1.3.3}$$

Obviously $\sup_{x\in\mathbb{R}} \{|a(x)| + |b(x)|\} = \frac{1}{n} \to 0$ as $n \to \infty$. However, for any $y > 0$ there holds

$$\sup_{x\in\mathbb{R}} |u(x,y)| = \frac{1}{n^2}\sinh(ny) \to \infty, \quad n \to \infty, \tag{1.3.4}$$

implying that the solution does NOT depend on the input data $a(x)$, $b(x)$ continuously.

Example 1.2. (Fredholm Integral Equations of the First kind) *Let $\mathcal{Z}$ and $\mathcal{H}$ be norm spaces and assume $\mathcal{P} : \mathcal{Z} \to \mathcal{H}$ is a continuous linear operator from $\mathcal{Z}$ into $\mathcal{H}$ with a continuous square integrable kernel $k(\cdot,\cdot)$ on $\bar{\mathcal{Z}} \times \bar{\mathcal{H}}$, where $\bar{\mathcal{Z}}$ denotes the closure of $\mathcal{Z}$. Then the classical Fredholm integral equation of the first kind has the following form*

$$\mathcal{P}z(t) = \int_0^1 k(t,s)z(s)\,\mathrm{d}s = h(t), \quad t \in [0,1]. \tag{1.3.5}$$

The forward problem here is to determine the data h for a known kernel k and a given image z, while the inverse problem is to find the image z from the given data h.

The kernel of (1.3.5) is of important consequence for the degree of ill-posedness of the inverse problem as the integration with k has a smoothing influence on h. The natural dynamic range in data h, i.e. the transitions, extremes and other essential characteristics, is therefore deteriorated by the integration operation. Conversely, this smoothing effect implies that even small perturbations in the observed data h may cause unacceptably large perturbations in the estimate of the sought solution.

To be precise, we give one numerical example. Let the kernel be $k(t,s) = e^{ts}$ and the observed data be $h(t) = \frac{e^{t+1}-1}{t+1}$. Equation (1.3.5) admits unique exact solution $z(t) = e^t$. On the other hand, we consider to solve equation (1.3.5) numerically for given k and h, by approximating the integral operator $\mathcal{P}$ directly using compound trapezoidal formula

$$\int_0^1 e^{ts} z(s)\,\mathrm{d}s \approx t_\tau \left(\frac{1}{2} z(0) + \frac{1}{2} e^t z(1) + \sum_{j=1}^{n-1} e^{j\tau t} z(jt_\tau) \right) \tag{1.3.6}$$

with discrete level n and step size $t_\tau = \frac{1}{n}$, which yields the linear algebra system

$$t_\tau \left(\frac{1}{2} z_0 + \frac{1}{2} e^t z_n + \sum_{j=1}^{n-1} e^{j\tau t} z_j \right) = h(jt_\tau), \quad j = 0, 1, \cdots, n. \tag{1.3.7}$$

We compute the approximate value z_j of exact value $z(jt_\tau)$ by applying the collocation method for (1.3.7). The error between numerical solution and exact solution $z_j - z(jt_\tau)$ at different time $t = jt_\tau$ with different n are listed in following table.

Table 1.1: Error distribution with different discrete level n.

t	$n=4$	$n=8$	$n=16$	$n=32$
0	0.44	-3.08	1.08	-38.21
0.25	-0.67	-38.16	-25.17	50.91
0.5	0.95	-75.44	31.24	-116.45
0.75	-1.02	-22.15	20.03	103.45
1	1.09	-0.16	20.03	103.45

Table 1.1 shows that the error between numerical solution and exact solution becomes large as the discrete level increasing, which is obviously a meaningless result [76, 83]. Therefore, equation (1.3.5) can NOT be solved directly by dividing $[0, 1]$ with large n, and the reason can be attributed to the ill-posedness of solving Fredholm integral equations of the first kind (It is the same for Volterra integral equations of the first kind).

Classical regularization methods

In practice, we only have the noisy data h^δ of exact data h satisfying

$$\left\| h^\delta - h \right\| \leq \delta$$

with $\delta > 0$. Then, for solving equation (1.3.1), the question is how to obtain the approximate solution z^δ of z from the noisy data h^δ of h? Actually, as shown before, we can not directly obtain z^δ by solving its corresponding problem

$$\mathcal{P}z^\delta = h^\delta. \tag{1.3.8}$$

This is because the ill-posedness of the inverse problem. That is

- 1. If $h^\delta \notin \mathcal{P}(\mathcal{Z})$, there exists not a solution $z^\delta \in \mathcal{Z}$ to (1.3.8);
- 2. Even if $h^\delta \in \mathcal{P}(\mathcal{Z})$, it does not guarantee the solution z^δ obtained by (1.3.8) satisfies $z^\delta \to z$ as $\delta \to 0$, since the inverse operator $\mathcal{P}^{-1}$ of $\mathcal{P}$ is unbounded.

Thus, to obtain an approximate solution z^δ satisfying $z^\delta \to z$ as $\delta \to 0$ even for $h^\delta \notin \mathcal{P}(\mathcal{Z})$, we introduce the *regularization method*, the basic idea of which is that, instead of trying to solve the *ill-posed* problem (1.3.8) exactly, one seeks to construct its *well-posed* approximated problem that is uniquely solvable and small errors in the data do not corrupt excessively this approximate solution. In short, the objective in regularization is to construct an appropriate bounded approximation $\mathcal{R} : \mathcal{H} \to \mathcal{Z}$ of the, possibly unbounded

$$\mathcal{P}^{-1} : \mathcal{H} \to \mathcal{Z}.$$

Definition 1.2. (Regularization) *A family of continuous operators* $\mathcal{R}_\alpha : \mathcal{H} \to \mathcal{Z}$ *are called regularization operators with regularization parameter* $\alpha > 0$ *if*

$$\lim_{\alpha\to 0} \mathcal{R}_\alpha \mathcal{P} z = z, \quad \forall z \in \mathcal{Z}.$$

We note that $\mathcal{R}_\alpha$ is a bound operator for any fixed $\alpha > 0$. $\mathcal{R}_\alpha\mathcal{P}$ converges pointwise to the identity as $\alpha \to 0$.

Definition 1.3. (Regularization parameter) *Let* $\delta > 0$. *The choice of regularization parameter* $\alpha(\delta)$ *is called admissible if*

$$\alpha(\delta) \to 0, \quad \sup_{z\in\mathcal{Z}} \left\{ \left\| \mathcal{R}_{\alpha(\delta)} h^\delta - z \right\| : \left\| \mathcal{P}z - h^\delta \right\| \le \delta \right\} \to 0$$

whenever $\delta \to 0$.

The probably most well-known method for solving linear or nonlinear ill-posed problems is *Tikhonov regularization*: it consists in approximating a solution of (1.3.1) by a minimizer z_α^δ of the *Tikhonov functional*

$$\mathcal{J}_{\alpha,\delta} := \left\| \mathcal{P}z - h^\delta \right\|^2 + \alpha \left\| z - z_0 \right\|^2, \tag{1.3.9}$$

where $z_0 \in \mathcal{Z}$ typically unifies all available *a-priori* information on the solution and $\alpha > 0$ is a regularization parameter. There are two kinds of strategies for choosing α. The *a-priori choice*: based on the information about the smoothness of exact solution. The *a-posteriori choice*: based on the noisy data and the error level. The introduction given here is necessarily brief. For a more comprehensive study of ill-posed problems and some general methods for solving ill-posed problems can be found in [77–83].

Overview of FDOT

We have given a brief introduction to forward problem, inverse problem and the classical Tikhonov regularization method. Also, for FDOT, it consists of two parts of the problems: the modeling of the fluorescence photon propagation in the tissue, so-called *forward problem*, and solving an *inverse problem* with measurement specified on the tissue surface to identify an unknown target.

For the forward problem of FDOT, F.Marttelli et al [19] and H.B.Jiang [26] summarized the principles and applications of light propagation through biological tissue and other diffusive media, and gave the theory, solutions and software codes, respectively. We can also refer [23, 24, 29, 34, 35] for the knowledge of forward diffusion model.

For the inverse problem of FDOT, as theoretical results, in addition to the usual L^2 regularization, the L^1 regularization was tested [36–39] and the total variation was considered [40]. An improvement of image quality was reported with the total variation by making use of the Bregman distance [41]. In data acquisition the measured fluorescence light can be divided by the measured excitation light to cancel unknown constants, which was introduced as normalized measurement [42].

FDOT has three different modes depending on the type of the measurement: *continuous wave* (CW) [43–46], *frequency domain* (FD) [47–50] and *time-domain* (TD) [51–55]. Here, we follow the conventional terminology, CW, meaning steady-state or zero-frequency of FD. In the rest of thesis we focus our attention to the investigation on FDOT using TD technique. Usually, TD method is measuring the temporal response of fluorescence excited by the pulsed excitation light injection. On the other hand, FD is measuring the modulation amplitude and phase of fluorescence with respect to the modulated excitation source and is the Fourier transform of TD. CW is the particular case of FD when the frequency is zero. Thus, TD technique basically provides the richest information compared with CW technique and FD technique [33]. We can refer to [23, 56] for the choice of data types in time-resolved FDOT. [23, 24] presented a review of methods for the forward and inverse problems in optical tomography. In [57], the time-resolved FDOT was considered but the fundamental solution was used simply by ignoring the presence of boundaries. Many of these works are focusing on small animal measurements and employing the trans-illumination scheme. We are here focusing on a epi-illumination scheme of the detection for more larger tissues. We summarize our main results below.

1.4 Summary of Thesis

We focus on the fluorescence and study on its aforementioned inverse problem based on DE model using time-domain measurements. In our case, measurements are a set of excitation and detection pair on the surface of tissue like chest and the distance between excitation and detection points is usually limited less than 2–3 cm because of the strong attenuation of fluorescence intensity. This distance range is very small rather than the tissue size and thus we are assuming the half space for the modeling of tissue. Then, we will study three-dimensional FDOT using the analytical solution of its initial boundary value problem in the half space.

In addition, aiming at a fast and robust numerical algorithm, we focus on the recovery of the position of a fluorophore target neglecting its precise shape. Then we try to find the cuboid which represents the true target, by which we can obtain the approximate position, approximate shape and approximate size of fluorophores in the tissue. Due to the assumption of the cuboid shape, the recovery of our FDOT can be done by identifying only several unknown parameters. We note here that throughout the thesis we will use “cuboid" and “cuboidal" for rectangular parallelepiped and its adjective for our convenience, respectively. We will numerically evaluate the rationality of approximating unknown target by cuboid and theoretically consider the local analysis of FDOT using *cuboid approximation*, which will give us some theoretical supports for our inversion scheme based on cuboid approximation. For the inversion in my thesis, the well-known

Levenberg-Marquardt (LM) scheme [11–14] will be employed, which is simple and easy to accomplish but still sensitive to the initial guess.

Thus, for the robustness and fast convergence of our inversion scheme, we separate the inversion process by three steps [17]. That is, we narrow the region of interest during the inversion process. Before assuming a cuboid, we use a cube to have a good initial guess. The initial guess for the cube is chosen using the spatial knowledge of the intensity from boundary measurements. The proposed inversion scheme will be tested both numerically and experimentally. We will consider the three-dimensional FDOT using the time-dependent diffusion equation, which is the most computationally expensive FDOT. Using the proposed method, we show that the three-dimensional FDOT in time domain is feasible on a laptop computer (Apple MacBook Pro, 2.7 GHz Intel Core i5). We note that if we consider continuous-wave or frequency-domain measurements, two numerical integrals could be removed in our formulation (see U_m^{exp} in (4.1) in Chapter 4) and the computational time will be further reduced.

We tried hard to put all the arguments mathematically logical and rigorous as much as possible, and also in the concepts of mathematics. This will clarify the arguments and present the features of the inverse problem more clearly. Our approach using a simplified target model and step-wise processing algorithm to find a good initial guess is a very reliable and fast algorithm. Since in the clinical applications producing a fast reliable images is very important, we believe that our algorithm is giving an important step for further study of FDOT.

The remainder of my thesis is organized as follows:

- Chapter 2: we introduce the *linearized DE model* and analyze its reasonability of the approximation from (1.2.7) to (1.2.8). We establish the error estimate rigorously for the excitation field due to ignoring the effect of fluorescence absorption and the corresponding error estimate for recovering the distribution of fluorophores in biological tissue from the linearized DE model.

- Chapter 3: we establish the identifiability of the fluorophore and reveal the physical difficulty of the 3-dimensional imaging model by the back scattering diffusive system. We also analyze the long-time behavior of emission light, by which we can estimate the fluorescence lifetime.

- Chapter 4: we consider the FDOT based on linearized DE model and propose the idea of *cuboid approximation*, which is reasonable and fast in computation by numerically testing.

- Chapter 5: from the view of mathematics, we describe our FDOT inverse problem using cuboid approximation and show its local analysis including local solvability and local Lipschitz stability, which is also essential for the convergence of iteration methods.

- Chapter 6: based on the simulation and property of measurement in Chapter 4, we propose our *inversion strategy* to accelerate the speed of convergence of LM iteration scheme, followed by two numerical examples illustrating the performance of the proposed strategy.

- Chapter 7: we further validate our inversion strategy using experimental data obtained from ex vivo beef phantoms. By the results of inversion using simulated data and experimental data, we verify that our proposed strategy is fast and robust against the choice of initial guesses.

- Chapter 8: Conclusion and future directions

Chapter 2

Linearized Diffusion Equation Model

In this chapter, we introduce the *linearized inverse problem* based on diffusion equation (DE) model for FDOT and analyze the reasonability of the model approximation from radiative transfer equation (RTE) model to *linearized DE model.* In section 2.1, by transforming the radiative transfer system into coupled diffusion equations for the averaged fields, we first introduce a nonlinear inverse problem to identify the absorption coefficient for a fluorophore by this system using time resolved boundary measurement. In section 2.2, for the linearized inverse problem obtained by ignoring the absorption by the fluorophores on the excitation field, we next establish the estimations of errors on the excitation field and the solution to the inverse problem, which ensures the reasonability of the model approximation qualitatively. Some numerical verifications are presented to show the validity of such a linearizing process quantitatively in section 2.3. Finally, section 2.4 is devoted to conclusion and remark of this chapter.

2.1 From RTE Model to Linearized DE Model

We first give the RTE model for our FDOT and then introduce the nonlinear FDOT inverse problem based on DE model which is nonlinear and named *nonlinear DE model.* By ignoring the absorption coefficient of fluorophores in the DE equation for excitation, we obtain the simplified DE model for FDOT which yields the *linearized DE model* in this chapter.

2.1.1 RTE model and our FDOT

Fluorescence imaging aims to identify some fluorophores with absorption coefficient $\mu_f(x)$ which occupies an interior bounded domain Ω_0 together with its boundary in Ω filled with a known background medium, for which we denote by $\Omega_0 \Subset \Omega$ in the following. Let us begin with the radiative transfer equation which can accurately describe the light propagation through strong turbid media.

Radiative transfer equations: As we explained in Figure 1.1, two physical processes in FDOT are coupled, namely, excitation and fluorescence (emission). Each propagation of them in scattering media can be described with the Boltzmann transport equation (1.2.1). Describing the photon propagations of the excitation light (subscript e) and the corresponding emission light (subscript m), these two kinds of the propagation are involved and described by the following coupled RTEs

$$\frac{1}{c}\frac{\partial \Phi_e}{\partial t} + \theta \cdot \nabla \Phi_e + (\mu_{ae} + \mu_f(x) + \mu_{se})\Phi_e - \mu_{se}\int_{\mathbb{S}^2} \eta(\theta \cdot \theta')\Phi_e(x, \theta', t)\, \mathrm{d}\theta' = 0, \quad (2.1.1)$$

and

$$\frac{1}{c}\frac{\partial \Phi_m}{\partial t} + \theta \cdot \nabla \Phi_m + (\mu_{am} + \mu_{sm})\Phi_m - \mu_{sm} \int_{\mathbb{S}^2} \eta(\theta \cdot \theta')\Phi_m(x, \theta', t)\,\mathrm{d}\theta' = q_m, \tag{2.1.2}$$

where $\Phi_e(x, \theta, t)$ and $\Phi_m(x, \theta, t)$ represent the angularly resolved *radiant intensity* of the excitation and emission light, respectively, c is the speed of light in the medium. The source term for Φ_m in (2.1.2) coming from the excitation field is specified by

$$q_m(x, t) = \frac{\gamma \mu_f(x)}{4\pi\tau} \int_0^t \int_{\mathbb{S}^2} \exp\left(-\frac{t - t'}{\tau}\right) \Phi_e(x, \theta', t')\,\mathrm{d}\theta' dt', \tag{2.1.3}$$

where $\tau > 0$ is the *fluorescence lifetime* and $0 < \gamma \leq 1$ is the quantum efficiency of the fluorescence. The scattering phase function $\eta(\theta \cdot \theta')$ meets the conditions

$$\int_{\mathbb{S}^2} \eta(\theta \cdot \theta')\,\mathrm{d}\theta = 1, \qquad \int_{\mathbb{S}^2} \theta \eta(\theta \cdot \theta')\,\mathrm{d}\theta = g\theta'$$

for the average scattering cosine $g \in (-1, 1)$.

Suppose that both the absorption and scattering coefficients of the background medium are constants in Ω. Furthermore we assume that the absorption and scattering coefficients for the excitation and emission light are the same. That is, $\mu_{ae} = \mu_{am} \equiv \mu_a$ and $\mu_{se} = \mu_{sm} \equiv \mu_s$, with constants $\mu_a > 0, \mu_s > 0$. Define the reduced scattering coefficient $\mu_s' := (1 - g)\mu_s$. The absorption coefficient for the fluorophore is given by $\mu_f(x) = \epsilon N(x)$, where ϵ is the molar extinction coefficient, and $N(x)$ is the *fluorophore concentration* with support Ω_0, which is relatively small compared with Ω. Thus, $\mu_f(x)$ is proportional to the amount of the fluorophores.

Semi-infinite medium: In noninvasive clinical applications of FDOT, the source and the detector must be placed on the surface of the tissue to be examined. Perhaps the most common FDOT geometry can be approximated by a semi-infinite medium with a planar boundary. Thus, in this thesis, we consider the case that Ω is the half space, i.e.,

$$\Omega := \mathbb{R}^3_+ = \{(x_1, x_2, x_3) : (x_1, x_2) \in \mathbb{R}^2, x_3 > 0\}$$

with the boundary $\partial\Omega := \{(x_1, x_2, 0) : (x_1, x_2) \in \mathbb{R}^2\}$ and the unit outward normal vector $\nu = (0, 0, -1)$.

Initial and boundary conditions: Both transport equation and diffusion equation to be solvable uniquely need to specify appropriate initial conditions and boundary conditions. Assuming that the excitation field Φ_e is generated by an infinitely short pulse in time and a point source directed to the normal on the boundary. Then the Fresnel reflection law [29, 59] leads to the boundary conditions

$$\Phi_e(x, \theta, t) = R_e(|\theta \cdot \nu|)\Phi_e(x, \theta^\top, t) + \delta(x - x_s)\delta(\theta + \nu)\delta(t), \ x \in \partial\Omega, \tag{2.1.4}$$

$$\Phi_m(x, \theta, t) = R_m(|\theta \cdot \nu|)\Phi_m(x, \theta^\top, t), \ x \in \partial\Omega \tag{2.1.5}$$

for $\theta \cdot \nu < 0$. Here, $\delta(\cdot)$ is the Dirac δ-function, $\theta^\top \in \mathbb{S}^2$ is the angle symmetric to θ about ν, R_e, R_m are the Fresnel reflection coefficients, which we assume $R := R_e = R_m$. Let n_1 and n_2 with $n_1 > n_2$ be the refractive indices inside and outside of the medium, respectively. For the unpolarized light, we have [19]

$$R(\cos\xi) := \begin{cases} \frac{1}{2}(R_s(\cos\xi) + R_p(\cos\xi)), & 0 \leq \xi \leq \xi_c, \\ 1, & \xi_c \leq \xi \leq \pi/2, \end{cases} \tag{2.1.6}$$

where R_s and R_p denote the Fresnel reflection of the perpendicular and parallel polarizations given as

$$R_s(\cos\xi) := \left|\frac{n_1\cos\xi - n_2\cos\xi_t}{n_1\cos\xi + n_2\cos\xi_t}\right|^2, \quad R_p(\cos\xi) := \left|\frac{n_1\cos\xi_t - n_2\cos\xi}{n_1\cos\xi_t + n_2\cos\xi}\right|^2,$$

with the critical angle $\xi_c := \arcsin\frac{n_2}{n_1}$, while $\cos\xi_t = (1-(\frac{n_1}{n_2}\sin\xi)^2)^{1/2}$. The initial conditions are given by

$$\Phi_e(x,\theta,0) = 0, \quad (x,\theta)\in\Omega\times\mathbb{S}^2, \tag{2.1.7}$$

$$\Phi_m(x,\theta,0) = 0, \quad (x,\theta)\in\Omega\times\mathbb{S}^2. \tag{2.1.8}$$

Thus we have formed an initial boundary value problem with governed equations (2.1.1)-(2.1.2), boundary conditions (2.1.4)-(2.1.5) and initial conditions (2.1.7)-(2.1.8).

The radiant intensity of the measurements on the boundary: Note n_1 and n_2 are the refractive indices inside and outside of the medium, respectively. Let θ be the direction for outgoing light inside and $\tilde{\theta}$ be its corresponding direction of light outside the medium. For $x\in\partial\Omega$, let $\Phi_m(x,\theta,t)$ and $\tilde{\Phi}_m(x,\tilde{\theta},t)$ be the radiant intensity of emission light on the internal boundary and external boundary of the medium, respectively. We further assume ξ and $\tilde{\xi}$ be the polar angle for the direction θ and $\tilde{\theta}$, respectively ($\theta\cdot\nu = \cos\xi$, $\tilde{\theta}\cdot\nu = \cos\tilde{\xi}$). From Snell's law, $\tilde{\xi}$ is related to ξ and satisfies

$$n_1\sin\xi = n_2\sin\tilde{\xi}. \tag{2.1.9}$$

Usually, the outside of medium is the air and the refractive index is almost 1, i.e, $n_2 = 1$. Further, by the Fresnel reflection law, the radiance on the external boundary surface, expressed as the fraction of the internal radiance transmitted in the external medium, can be written as

$$\tilde{\Phi}_m(x,\tilde{\theta},t) = \left(\frac{n_2}{n_1}\right)^2[1-R(|\theta\cdot\nu|)]\Phi_m(x,\theta,t), \quad x\in\partial\Omega,\ t\in(0,T), \tag{2.1.10}$$

where R is the Fresnel reflection coefficient.

Note (2.1.10). For the measurement, the quantity actually measured at the boundary point $x\in\partial\Omega$ is the outgoing radiance accepted by the detection system, which is

$$H(x,t) = \tilde{\Phi}_m(x,\nu,t) = \left(\frac{n_2}{n_1}\right)^2[1-R(1)]\Phi_m(x,\nu,t), \quad (x,t)\in\partial\Omega\times(0,T) \tag{2.1.11}$$

along the normal direction $\nu = (0,0,-1)$, or the average field

$$H(x,t) = \int_{\mathbb{S}^2_-}\tilde{\Phi}_m(x,\tilde{\theta},t)\,\mathrm{d}\tilde{\theta}, \quad (x,t)\in\partial\Omega\times(0,T), \tag{2.1.12}$$

where $\tilde{\Phi}_m(x,\tilde{\theta},t)$ is given by (2.1.10) and $\mathbb{S}^2_-$ is the set of all unit vectors with negative x_3-components, i.e., $\tilde{\theta}\cdot\nu\geq 0$.

Our FDOT: Suppose μ_a, μ_s, g are known. The FDOT problem for fluorescence imaging is to recover the unknown $\mu_f(x)$ from the measurement either (2.1.11) or (2.1.12).

Since (Φ_e,Φ_m) depends on the scattering direction $\theta\in\mathbb{S}^2$, the imaging in terms of (2.1.2)-(2.1.12) is of large amount of numerical computations, which are often intractable. So people are motivated to consider the DE model for FDOT, which is the approximation of RTE model and will be shown in the following subsections.

2.1.2 Derivation of the diffusion equation

We first describe the approximation of RTE: *diffusion equation* (DE), which is a consequence of a combination of following three different approximations regarded as three steps.

Step 1: (P_1-approximation) First two terms of the expansions of the radiance Φ_e and Φ_m in spherical harmonics upon the angular variable θ yield

$$\Phi_e(x,\theta,t) = \frac{1}{4\pi}U_e(x,t) + \frac{3}{4\pi}\theta\cdot\mathbf{J}_e(x,t), \quad \theta\in\mathbb{S}^2,\ (x,t)\in\Omega\times(0,T), \tag{2.1.13}$$

$$\Phi_m(x,\theta,t) = \frac{1}{4\pi}U_m(x,t) + \frac{3}{4\pi}\theta\cdot\mathbf{J}_m(x,t), \quad \theta\in\mathbb{S}^2,\ (x,t)\in\Omega\times(0,T). \tag{2.1.14}$$

We see the new unknown variables arising: respectively the *photon density*, (U_e, U_m), and the *photon flux*, $(\mathbf{J}_e, \mathbf{J}_m)$. Note that their definitions follows directly by integration over all solid angles to (2.1.1) and (2.1.2), respectively. We have

$$U_e(x,t) := \int_{\mathbb{S}^2}\Phi_e(x,\theta,t)\,\mathrm{d}\theta, \quad U_m(x,t) := \int_{\mathbb{S}^2}\Phi_m(x,\theta,t)\,d\theta, \tag{2.1.15}$$

$$\mathbf{J}_e(x,t) := \int_{\mathbb{S}^2}\theta\cdot\Phi_e(x,\theta,t)\,\mathrm{d}\theta, \quad \mathbf{J}_m(x,t) := \int_{\mathbb{S}^2}\theta\cdot\Phi_m(x,\theta,t)\,\mathrm{d}\theta. \tag{2.1.16}$$

This, so-called, P_1-approximation disregards terms of quadratic and higher order in θ. Such approximate expansions are reasonable, since the angular dependence of (Φ_e, Φ_m) become weak at a large scale.

We note that the source $q_m(x,t)$ given by (2.1.3) has no angular dependence. It is safe to substitute (2.1.15)-(2.1.16) into the transport equations of (2.1.1)-(2.1.2), respectively, such that we have [19, 30]

$$\begin{aligned}
\frac{1}{c}\frac{\partial U_e(x,t)}{\partial t} + \nabla\cdot\mathbf{J}_e(x,t) + (\mu_a+\mu_f(x))U_e(x,t) &= 0, && (2.1.17)\\
\frac{1}{c}\frac{\partial \mathbf{J}_e(x,t)}{\partial t} + \frac{1}{3}\nabla U_e(x,t) + (\mu_a+\mu_f(x)+\mu_s')\mathbf{J}_e(x,t) &= 0, && (2.1.18)\\
\frac{1}{c}\frac{\partial U_m(x,t)}{\partial t} + \nabla\cdot\mathbf{J}_m(x,t) + \mu_a U_m(x,t) &= S(x,t), && (2.1.19)\\
\frac{1}{c}\frac{\partial \mathbf{J}_m(x,t)}{\partial t} + \frac{1}{3}\nabla U_m(x,t) + (\mu_a+\mu_s')\mathbf{J}_m(x,t) &= 0 && (2.1.20)
\end{aligned}$$

with

$$S(x,t) := \int_{\mathbb{S}^2} q_m(x,t)\,\mathrm{d}\theta'' = 4\pi q_m(x,t). \tag{2.1.21}$$

Step 2: ($\frac{\partial}{\partial t}|\mathbf{J}| \ll c\mu_s'|\mathbf{J}|$) The photon flux $(\mathbf{J}_e, \mathbf{J}_m)$ change only slowly in time compared to the mean collision time. Then by (2.1.18) and (2.1.20) we derive

$$\mathbf{J}_e = -\frac{1}{3(\mu_a+\mu_f(x)+\mu_s')}\nabla U_e, \quad \mathbf{J}_m = -\frac{1}{3(\mu_a+\mu_s')}\nabla U_m.$$

Step 3: (μ_a, $\mu_f \ll \mu_s'$) In fact the diffusion coefficient is rigorously independent of μ_a [74] and $\mu_f \ll \mu_s'$ in most cases of the application. Thus we can approximate

$$\mathbf{J}_e = -D\nabla U_e, \quad \mathbf{J}_m = -D\nabla U_m \tag{2.1.22}$$

with $D := \frac{1}{3\mu_s'}$ is the *photon diffusion coefficient*. Substituting (2.1.22) into (2.1.17) and (2.1.19) we immediately have the *diffusion equations* for excitation and emission that

$$\left(\frac{1}{c}\frac{\partial}{\partial t} - D\Delta + \mu_a + \mu_f(x)\right) U_e(x,t) = 0, \quad (x,t) \in \Omega \times (0,T), \tag{2.1.23}$$

and

$$\left(\frac{1}{c}\frac{\partial}{\partial t} - D\Delta + \mu_a\right) U_m(x,t) = S(x,t), \quad (x,t) \in \Omega \times (0,T). \tag{2.1.24}$$

Recalling the definitions (2.1.3) for $q_m(x,t)$ and (2.1.21) for $S(x,t)$. By (2.1.13) and (2.1.22) there holds

$$\begin{aligned} S(x,t) = 4\pi q_m &= \frac{\gamma\mu_f(x)}{\tau}\int_0^t \int_{\mathbb{S}^2} e^{-\frac{t-t'}{\tau}} \left[\frac{1}{4\pi}U_e(x,t') - \frac{3D}{4\pi}\theta' \cdot \nabla U_e(x,t')\right] \mathrm{d}\theta' \mathrm{d}t' \\ &= \frac{\gamma\mu_f(x)}{\tau}\int_0^t e^{-\frac{t-t'}{\tau}} U_e(x,t')\,\mathrm{d}t'. \end{aligned}$$

2.1.3 Boundary condition for the diffusion approximation

Next we will derive the boundary conditions for (U_e, U_m) in terms of (2.1.4) and (2.1.5). To this end, we unify (2.1.4) and (2.1.5) for $\theta \cdot \nu < 0$ (i.e., $\theta \in \mathbb{S}^2_+$) as the form

$$\Phi(x,\theta,t) = R(|\theta\cdot\nu|)\Phi(x,\theta^\top,t) + \kappa(x-x_s,t)\delta(\theta+\nu) \text{ on } x_3 = 0,$$

where $\kappa(x-x_s,t)$ is either $\delta(x-x_s)\delta(t)$ or 0. Then the representation $\Phi(x,\theta,t) = \frac{1}{4\pi}U(x,t) + \frac{3}{4\pi}\theta\cdot\mathbf{J}$ with $\mathbf{J} = -D\nabla U$ leads to the boundary condition

$$\begin{aligned} \frac{1}{4\pi}U + \frac{3}{4\pi}\theta\cdot\mathbf{J} = R(|\theta\cdot\nu|)&\left(\frac{1}{4\pi}U + \frac{3}{4\pi}\theta^\top\cdot\mathbf{J}\right) \\ &+ \kappa(x-x_s,t)\delta(\theta+\nu), \quad x_3 = 0. \end{aligned} \tag{2.1.25}$$

In terms of the expression

$$\theta = (\cos\varphi\sin\xi, \sin\varphi\sin\xi, \cos\xi) \in \mathbb{S}^2_+, \quad \theta^\top = (\cos\varphi\sin\xi, \sin\varphi\sin\xi, -\cos\xi), \tag{2.1.26}$$

the polar angle and azimuthal angle are $\xi \in [0,\pi/2)$, $\varphi \in [0, 2\pi)$. Moreover, $\theta\cdot\nu = -\cos\xi$. Thus the first and the second components of $\int_{\mathbb{S}^2_+} \cos\xi\ \theta\,\mathrm{d}\theta$ and $\int_{\mathbb{S}^2_+} \cos\xi\ R(|\theta\cdot\nu|)\theta^\top\,\mathrm{d}\theta$ are zero. Let us introduce $\mu := \cos\xi$. By multiplying both sides of (2.1.25) by μ and integrating with respect to $\theta \in \mathbb{S}^2_+$, we have

$$\begin{aligned} \int_{\mathbb{S}^2_+}\left(\frac{1}{4\pi}U + \frac{3}{4\pi}\theta\cdot\mathbf{J}\right)\mu\,\mathrm{d}\mu\mathrm{d}\varphi = &\int_{\mathbb{S}^2_+} R(\mu)\mu\left(\frac{1}{4\pi}U + \frac{3}{4\pi}\theta^\top\cdot\mathbf{J}\right)\mathrm{d}\mu\mathrm{d}\varphi \\ &+ \int_{\mathbb{S}^2_+}\kappa(x-x_s,t)\delta(\theta+\nu)\mu\,\mathrm{d}\mu\mathrm{d}\varphi. \end{aligned}$$

After the integration over φ and then over $\mu = \cos\xi$, we obtain

$$\frac{1}{4}U + \frac{1}{2}J_3 = \frac{1}{2}U\int_0^1 R(\mu)\mu\,\mathrm{d}\mu - \frac{3}{2}J_3\int_0^1 R(\mu)\mu^2\,\mathrm{d}\mu + \kappa(x-x_s,t),$$

where $J_3 := -D\frac{\partial U}{\partial x_3}$. Therefore we obtain the partial current boundary condition (PCBC) for (U_e, U_m) as follows

$$\begin{aligned} -D\frac{\partial U_e}{\partial x_3} + \frac{1}{2A}U_e &= \omega_e \delta(x - x_s)\delta(t), \quad x \in \partial\Omega, && (2.1.27) \\ -D\frac{\partial U_m}{\partial x_3} + \frac{1}{2A}U_m &= 0, \quad x \in \partial\Omega, && (2.1.28) \end{aligned}$$

where the coefficients are defined by

$$A := \frac{1 + 3\int_0^1 R(\mu)\mu^2 \,\mathrm{d}\mu}{1 - 2\int_0^1 R(\mu)\mu \,\mathrm{d}\mu}, \quad \omega_e := \frac{2}{A\big(1 - 2\int_0^1 R(\mu)\mu \,\mathrm{d}\mu\big)}. \tag{2.1.29}$$

The first term of the left hand side in (2.1.27) and (2.1.28) are the mathematical expression of Fick's law, which expresses how much photon flux exist with respect to x_3. Then $\frac{1}{2A}$ means the reflection at the boundary. The constant ω_e in the right hand side of (2.1.27) is the injected photon density.

Define $\beta := \frac{1}{2AD}$ and $\widetilde{\omega}_e := \omega_e/D$, which are proportional to the reflection and the injected photon density but scaled by D. Then we obtain the traditional Robin boundary conditions in mathematics, i.e.,

$$\begin{aligned} -\frac{\partial U_e}{\partial x_3} + \beta U_e &= \widetilde{\omega}_e \delta(x - x_s)\delta(t), \quad x \in \partial\Omega, && (2.1.30) \\ -\frac{\partial U_m}{\partial x_3} + \beta U_m &= 0, \quad x \in \partial\Omega, && (2.1.31) \end{aligned}$$

respectively. The initial conditions are given by

$$\begin{aligned} U_e(x, 0) = 0, \quad x \in \Omega, && (2.1.32) \\ U_m(x, 0) = 0, \quad x \in \Omega. && (2.1.33) \end{aligned}$$

2.1.4 Nonlinear DE model and its linearization

Combining above results together, we have obtained an initial boundary value problem for (U_e, U_m) which consists of the equations (2.1.23), (2.1.24), (2.1.30), (2.1.31) and (2.1.32), (2.1.33). That is

$$\begin{cases} \left(\frac{1}{c}\frac{\partial}{\partial t} - D\Delta + \mu_a + \mu_f(x)\right) U_e = 0, & (x,t) \in \Omega \times (0,T), \\ \nu \cdot \nabla U_e + \beta U_e = \delta(x - x_s)\delta(t), & x, x_s \in \partial\Omega, t \in (0,T), \\ U_e(x, 0) = 0, & x \in \Omega, \end{cases} \tag{2.1.34}$$

and

$$\begin{cases} \left(\frac{1}{c}\frac{\partial}{\partial t} - D\Delta + \mu_a\right) U_m = S[\mu_f, U_e](x,t), & (x,t) \in \Omega \times (0,T), \\ \nu \cdot \nabla U_m + \beta U_m = 0, & (x,t) \in \partial\Omega \times (0,T), \\ U_m(x, 0) = 0, & x \in \Omega, \end{cases} \tag{2.1.35}$$

where

$$D := \frac{1}{3\mu_s'}, \quad \beta := \frac{1}{2AD}$$

with A given by (2.1.29) and the source term in (2.1.35) for U_m is

$$S[\mu_f, U_e](x,t) := \frac{\gamma\mu_f(x)}{\tau}\int_0^t e^{-\frac{t-s}{\tau}} U_e(x,s)\,\mathrm{d}s. \tag{2.1.36}$$

We remark here we ignored the constant $\widetilde{\omega}_e$ in the initial boundary value problem (2.1.34). This factor only affects the scaling of the photon density and thus the discussions through the thesis will not change even if ignoring $\widetilde{\omega}_e$.

Now we transform (2.1.11) or (2.1.12), which we call the *inversion input data*, into the inversion input for $U_m(x,t)$. Using the expansion (2.1.14) together with (2.1.22) for $\tilde{\theta} = \nu = (0,0,-1)$, it follows that

$$\begin{aligned} H(x,t) = \tilde{\Phi}_m(x,\nu,t) &= \left(\frac{n_2}{n_1}\right)^2 [1-R(1)]\Phi_m(x,\nu,t) \\ &= \left(\frac{n_2}{n_1}\right)^2 [1-R(1)]\left(\frac{1}{4\pi}U_m(x,t) + \frac{3D}{4\pi}\frac{\partial U_m(x,t)}{\partial x_3}\right) \end{aligned}$$

for $x \in \partial\Omega$. So the boundary condition in (2.1.35) yields

$$U_m(x,t) = \left[\left(\frac{n_2}{n_1}\right)^2 [1-R(1)]\left(\frac{1}{4\pi} + \frac{3D}{4\pi}\beta\right)\right]^{-1} H(x,t) \tag{2.1.37}$$

for $(x,t) \in \partial\Omega \times (0,T)$.

Now we are ready to transform the measurement (2.1.12), where the integration is for $\tilde{\theta}$ satisfying $\tilde{\theta}\cdot\nu \geq 0$ with $\nu = (0,0,-1)$. By (2.1.14) and (2.1.26) we have for $x \in \partial\Omega$ that

$$\begin{aligned} \Phi_m(x,\theta,t) &= \frac{1}{4\pi}U_m(x,t) + \frac{3}{4\pi}\theta\cdot\mathbf{J}_m(x,t) \\ &= \frac{1}{4\pi}U_m(x,t) + \frac{3}{4\pi}(J_{m\nu}\cos\xi + J_{m\omega}\cos\varphi\sin\xi), \end{aligned} \tag{2.1.38}$$

where $J_{m\nu}$ and $J_{m\omega}$ are the normal and the tangential component of the flux for emission light, and ξ and φ are the polar and azimuthal angle for θ, respectively, i.e., $\theta\cdot\omega = \cos\varphi\sin\xi$ and $\theta\cdot\nu = \cos\xi$ with ω denotes the tangential direction at $x \in \partial\Omega$. Similarly, denote

$$\tilde{\theta} = (\cos\tilde{\varphi}\sin\tilde{\xi}, \sin\tilde{\varphi}\sin\tilde{\xi}, \cos\tilde{\xi}) \in \mathbb{S}^2_-.$$

Substituting (2.1.38) into (2.1.10) and averaging over the azimuthal angle $\tilde{\varphi}$ ($\tilde{\varphi} = \varphi$), we obtain for $(x,t) \in \partial\Omega \times (0,T)$ that

$$\tilde{\Phi}_m(x,\tilde{\xi},t) = \left(\frac{n_2}{n_1}\right)^2 [1-R(|\theta\cdot\nu|)]\left(\frac{1}{4\pi}U_m(x,t) + \frac{3}{4\pi}J_{m\nu}\cos\xi\right), \tag{2.1.39}$$

where $\tilde{\Phi}_m(x,\tilde{\xi},t)$ is the radiance outgoing along $\tilde{\theta}$ averaged over $\tilde{\varphi}$. Further, by (2.1.22) and the boundary condition in (2.1.35) again, the expression for $\tilde{\Phi}_m(x,\tilde{\xi},t)$ can be simplified as

$$\tilde{\Phi}_m(x,\tilde{\xi},t) = \left(\frac{n_2}{n_1}\right)^2 [1-R(|\theta\cdot\nu|)]\left(\frac{1}{4\pi} + \frac{3D}{4\pi}\beta\cos\xi\right)U_m(x,t), \tag{2.1.40}$$

implying that

$$
\begin{aligned}
H(x,t) &= \int_{\mathbb{S}^2_-} \tilde{\Phi}_m(x,\tilde{\theta},t)\,\mathrm{d}\tilde{\theta} \\
&= \int_{\mathbb{S}^2_-} \left[\left(\frac{n_2}{n_1}\right)^2 [1 - R(\cos\xi)] \left(\frac{1}{4\pi} + \frac{3D}{4\pi}\beta\cos\xi \right) \right] \mathrm{d}\tilde{\xi}\, U_m(x,t)
\end{aligned}
$$

with $\xi = \arcsin\left(\frac{n_2}{n_1}\sin\tilde{\xi}\right)$ due to (2.1.9). Therefore, by (2.1.12), the inversion input data become

$$
U_m(x,t) = \left\{ \int_{\mathbb{S}^2_-} \left[\left(\frac{n_2}{n_1}\right)^2 [1 - R(\cos\xi)] \left(\frac{1}{4\pi} + \frac{3D}{4\pi}\beta\cos\xi \right) \right] \mathrm{d}\tilde{\xi} \right\}^{-1} H(x,t) \tag{2.1.41}
$$

for $(x,t) \in \partial\Omega \times (0,T)$, where $\xi = \arcsin\left(\frac{n_2}{n_1}\sin\tilde{\xi}\right)$.

Thus we have transformed our FDOT inverse problem to identify $\mu_f(x)$ into the DE model (2.1.34)-(2.1.35) from the specified boundary measurement data

$$
U_m(x,t) = C^* H(x,t), \quad (x,t) \in \partial\Omega \times (0,T), \tag{2.1.42}
$$

where the constant C^* depends on the inversion input data (2.1.11) or (2.1.12).

Since $U_e(x,t)$ satisfying (2.1.34) depends on the unknown $\mu_f(x)$ nonlinearly, the above inverse problem for $\mu_f(x)$ in terms of $U_m(x,t)$ is nonlinear. Note that $\|\mu_f\|_{L^2(\Omega_0)} \ll \mu_a$ can be assumed in many applications, one possible way of removing the nonlinearity is to ignore $\mu_f(x)$ in (2.1.34). Then we have the following *linearized DE model*

$$
\begin{cases}
\left(\frac{1}{c}\frac{\partial}{\partial t} - D\Delta + \mu_a\right) u_e = 0, & (x,t) \in \Omega \times (0,T), \\
\nu \cdot \nabla u_e + \beta u_e = \delta(x - x_s)\delta(t), & x, x_s \in \partial\Omega, t \in (0,T), \\
u_e(x,0) = 0, & x \in \Omega,
\end{cases} \tag{2.1.43}
$$

and

$$
\begin{cases}
\left(\frac{1}{c}\frac{\partial}{\partial t} - D\Delta + \mu_a\right) u_m = S[\mu_f, u_e](x,t), & (x,t) \in \Omega \times (0,T), \\
\nu \cdot \nabla u_m + \beta u_m = 0, & (x,t) \in \partial\Omega \times (0,T), \\
u_m(x,0) = 0, & x \in \Omega,
\end{cases} \tag{2.1.44}
$$

with the inversion input data

$$
u_m(x,t) = C^* H(x,t), \quad (x,t) \in \partial\Omega \times (0,T). \tag{2.1.45}
$$

The system (2.1.43)-(2.1.45) constitutes a *linear inverse problem* for identifying $\mu_f(x)$ from the inversion input (2.1.45) with known $u_e(x,t)$.

For the above model, we must consider following issue. When we ignore μ_f in (2.1.34) to yield a linear inverse problem (2.1.43)-(2.1.45), what is the error due to such a linearization for our imaging?

Although the above linearized DE model has been applied in engineering communities for a long time, as far as we know, there is no answer to the above question, to say nothing of the rigorous mathematical analysis. To ensure the efficiency of the linearized DE model, it is necessary and important to consider this issue, which will be given in the following section.

2.2 Error Estimations for Model Approximation

To establish the error for our inverse problem due to the linearization process, we need the explicit solution to the initial boundary value problems in the half space Ω with Robin boundary condition at $x_3 = 0$.

2.2.1 Analytical solutions using Green functions

An analytical solution is mostly given in the form of Green function that correspond to the solution arising from a point source in space and time for simple geometries such as infinite bulk media, homogeneous cylinders or semi-infinite slabs. For given point source located at $y \in \Omega$, we introduce the Green function $K(x, y; t)$ defined by

$$\begin{cases} \left(\frac{1}{c}\frac{\partial}{\partial t} - D\Delta + \mu_a\right) K = \delta(x-y)\delta(t), & (x,t) \in \Omega \times (0,T), \\ K = 0, & x \in \Omega,\ t = 0, \\ \nu \cdot \nabla K + \beta K = 0, & (x,t) \in \partial\Omega \times (0,T). \end{cases} \tag{2.2.1}$$

One can obtain the analytical expression of $K(x, y; t)$ by the functional solution of heat equation, which has been investigated extensively in the scientific community. Denote by

$$G_k(x,t) := \begin{cases} \frac{1}{\sqrt{(4\pi cDt)^k}}\, e^{-\frac{|x|^2}{4cDt}}, & t > 0, \\ 0, & t \le 0, \end{cases} \tag{2.2.2}$$

the fundamental solution to heat equation $\frac{1}{c}\frac{\partial u}{\partial t} - D\Delta u = 0$ in $(x,t) \in \mathbb{R}^k \times \mathbb{R}^1$ for $k = 1, 2, 3$. Then $K(x, y; t)$ has the representation [27, 28]

$$\begin{aligned} K(x,y;t) = {} & ce^{-c\mu_a t}\left(G_3(x-\bar{y},t) + G_3(x-y,t)\right) \\ & - 2c\beta e^{\beta y_3 - c\mu_a t}\int_{y_3}^{+\infty} e^{-\beta\zeta} G_3(x - y(\zeta), t)\,\mathrm{d}\zeta \end{aligned} \tag{2.2.3}$$

for $t > 0$ and $K(x, y; t) \equiv 0$ for $t \le 0$ due to (2.2.2), where $\bar{y} := (y_1, y_2, -y_3)$ and $y(\zeta) := (y_1, y_2, -\zeta)$ for $y = (y_1, y_2, y_3)$.

See Arridge [22] for a summary of Green functions for other geometries: infinite slab, 2D circle, finite and infinite cylinders and spheres. The derivation of Green functions for slab geometries follows the method of *mirror images* where a virtual point source with equal but negative strength is placed mirror-wise opposite to the real source [75].

Corollary 2.1. *For $x = (\tilde{x}, x_3), y = (\tilde{y}, y_3) \in \mathbb{R}^2 \times \mathbb{R}^1_+$, the Green function $K(x, y; t)$ for $t > 0$ has the decomposition*

$$K(x,y;t) = \frac{ce^{-c\mu_a t}}{\sqrt{(4\pi cDt)^3}} e^{-\frac{|\tilde{x}-\tilde{y}|^2}{4cDt}} K_3(x_3, y_3; t), \tag{2.2.4}$$

where $K_3(x_3, y_3; t)$ is given by

$$\begin{aligned} K_3(x_3,y_3;t) = {} & e^{-\frac{(x_3+y_3)^2}{4cDt}} + e^{-\frac{(x_3-y_3)^2}{4cDt}} \\ & - 2\beta\sqrt{\pi cDt}\, e^{\beta(x_3+y_3)+\beta^2 cDt}\,\mathrm{erfc}\left(\frac{x_3+y_3+2\beta cDt}{\sqrt{4cDt}}\right) \end{aligned} \tag{2.2.5}$$

with the complementary error function

$$\operatorname{erfc}(\xi) = \frac{2}{\sqrt{\pi}} \int_{\xi}^{\infty} e^{-s^2}\,\mathrm{d}s,\ \ \xi \in \mathbb{R}. \tag{2.2.6}$$

Proof. By the representations of $G_k(\cdot,\cdot)$ for $k = 1, 2, 3$ and (2.2.3), the verification of this identity is equivalent to show the identity

$$\int_{y_3}^{+\infty} e^{-\beta\zeta} e^{-\frac{(x_3+\zeta)^2}{4cDt}}\,\mathrm{d}\zeta \equiv \sqrt{\pi cDt}\; e^{\beta x_3+\beta^2 cDt} \times \operatorname{erfc}\left(\frac{x_3+y_3+2\beta cDt}{\sqrt{4cDt}}\right),\ \ t>0,$$

which can be derived by the variable transform $z = \frac{x_3+\zeta}{\sqrt{4cDt}} + \beta\sqrt{cDt}$ for the left hand side. □

We firstly state the representation formula for the parabolic system in terms of its Green function (for example, see Chapter 7 in [15]).

Lemma 2.1. *For $\rho(x) > 0, p(x) > 0, q(x) \geq 0, a(x) > 0, b(x) > 0$, the solution to the initial boundary value problem*

$$\begin{cases} \rho(x)\frac{\partial u}{\partial t} - \nabla\cdot(p(x)\nabla u) + q(x)u = \rho(x)F(x,t), & (x,t)\in\Omega\times(0,T),\\ b(x)\frac{\partial u}{\partial \nu} + a(x)u = B(x,t), & (x,t)\in\partial\Omega\times(0,T),\\ u(x,0) = f(x), & x\in\Omega \end{cases} \tag{2.2.7}$$

has the expression

$$u(y,s) = \int_0^T \int_{\Omega} \widetilde{K}(x,t;y,s)\rho(x)F(x,t)\,\mathrm{d}x\mathrm{d}t + \int_0^T \int_{\partial\Omega} \frac{p(x)}{b(x)} B(x,t)\widetilde{K}(x,t;y,s)\,\mathrm{d}x\mathrm{d}t + \int_{\Omega} \rho(x)f(x)\widetilde{K}(x,0;y,s)\,\mathrm{d}x,$$

where $\widetilde{K}(x,t;y,s)$ is the Green function determined by

$$\begin{cases} -\rho(x)\frac{\partial \widetilde{K}}{\partial t} - \nabla\cdot(p(x)\nabla \widetilde{K}) + q(x)\widetilde{K} = \delta(x-y)\delta(t-s), & (x,t)\in\Omega\times(0,T),\\ b(x)\frac{\partial \widetilde{K}}{\partial \nu} + a(x)\widetilde{K} = 0, & (x,t)\in\partial\Omega\times(0,T),\\ \widetilde{K}(x,T;y,s) = 0, & x\in\Omega \end{cases}$$

for point source located at $(y,s)\in\Omega\times(0,T)$. Here $\frac{\partial u}{\partial\nu}$ denotes $\nu\cdot\nabla u$.

By applying Lemma 2.1 to (2.1.43) and (2.1.44) we are ready to give the analytical expressions of u_e and u_m.

Lemma 2.2. *Suppose $\Omega_0 \Subset \Omega$ be the support of $\mu_f(x)$. For a given source located at $x_s \in \partial\Omega$, we have*

$$u_e(x,t;x_s) = D\times K(x,x_s;t),\quad (x,t)\in\overline{\Omega}\times[0,T], \tag{2.2.8}$$

$$u_m(x,t;x_s) = \int_0^t \int_0^s \frac{\gamma D e^{-(s-t')/\tau}}{\tau} \int_{\Omega_0} \mu_f(y) \times K(x,y;t-s)K(y,x_s;t')\,\mathrm{d}y\mathrm{d}t'\mathrm{d}s,\quad (x,t)\in\overline{\Omega}\times[0,T], \tag{2.2.9}$$

where $K(x,y;t)$ is the Green function satisfying (2.2.1).

Proof. Taking $\rho(x) \equiv 1/c$, $p(x) \equiv D$, $q(x) \equiv \mu_a$, $f(x) \equiv 0$ as well as $b(x) \equiv 1, a(x) \equiv \beta$ in Lemma 2.1, and noting that $\mu_f(x) \equiv 0$ in $\Omega \setminus \overline{\Omega}_0$, we have

$$u_e(x,t;x_s) = D \times \widetilde{K}(x_s,0;x,t) \tag{2.2.10}$$

and

$$u_m(x,t;x_s) = \int_0^t \int_{\Omega_0} \widetilde{K}(y,s;x,t) S[\mu_f,u_e](y,s)\,\mathrm{d}y\mathrm{d}s \tag{2.2.11}$$

for $(x,t) \in \overline{\Omega} \times [0,T]$, where $\widetilde{K}(x,t;y,s)$ satisfies

$$\begin{cases} -\frac{1}{c}\frac{\partial \widetilde{K}}{\partial t} - D\Delta\widetilde{K} + \mu_a\widetilde{K} = \delta(x-y)\delta(t-s), & (x,t) \in \Omega \times (0,T), \\ \frac{\partial \widetilde{K}}{\partial \nu} + \beta\widetilde{K} = 0, & (x,t) \in \partial\Omega \times (0,T), \\ \widetilde{K}(x,T;y,s) = 0, & x \in \Omega. \end{cases}$$

By a formal argument we have $\widetilde{K}(y,s;x,t) = K(x,y;t-s)$ with $K(x,y;t)$ satisfying (2.2.1). Then (2.2.10) and (2.2.11) imply (2.2.8) and (2.2.9) respectively. □

Remark 2.1. *The reason why the diffusion coefficient D explicitly appeared in* (2.2.8) *and* (2.2.9) *is that we ignored the constant $\widetilde{\omega}_e = \omega_e/D$ in the right hand side of the boundary condition in* (2.1.34). *Let u_e^ε, $\varepsilon > 0$ be the solution of the following initial boundary value problem with a transient point source:*

$$\begin{cases} \left(\frac{1}{c}\frac{\partial}{\partial t} - D\Delta + \mu_a\right) u_e^\varepsilon = \delta(x_1 - x_{s1})\delta(x_2 - x_{s2})\delta(x_3 - \varepsilon)\delta(t), & (x,t) \in \Omega \times (0,T), \\ u_e^\varepsilon(x,0) = 0, & x \in \Omega, \\ \nu \cdot \nabla u_e^\varepsilon + \beta u_e^\varepsilon = 0, & (x,t) \in \partial\Omega \times (0,T). \end{cases}$$

The solution u_e of (2.1.43) is a limit of the solution $D \times u_e^\varepsilon$, i.e., the distribution Du_e^ε converges to the distribution u_e as $\varepsilon \to 0$ [64].

2.2.2 Error estimation for excitation

The error on our imaging solution due to the linearization process comes from the approximation error $U_e - u_e$ for the excitation field, which can be estimated by the following.

Theorem 2.1. *For $\mu_f(x) \geq 0$ with support $\Omega_0 \Subset \Omega$, the error for the excitation field by ignoring $\mu_f(x)$ has the estimate*

$$\|U_e - u_e\|_{L^2((0,T)\times\Omega)} \leq C(\Omega_0,T,c,D) \left\| \frac{\mu_f(\cdot)}{\mu_a} \right\|_{L^2(\Omega_0)}, \tag{2.2.12}$$

where $U_e(x,t;x_s)$ meets the DE system (2.1.34) and $u_e(x,t;x_s)$ satisfying (2.1.43) is its approximation by ignoring $\mu_f(x)$ in (2.1.34), and the known constant $C > 0$ independent on μ_a is given by

$$C(\Omega_0,T,c,D) := \frac{1}{\sqrt{4cD\pi^3}} \left(\int_0^T \frac{1}{t^3} e^{-\frac{C_0^2}{2cDt}}\,\mathrm{d}t \right)^{1/2} \tag{2.2.13}$$

with the positive constant $C_0 = C_0(\Omega_0) := \min_{x\in\Omega_0}\{dist(x,\partial\Omega)\}$.

Proof. For the simplicity of notations, we write $U_e(x,t;x_s), u_e(x,t;x_s)$ as $U_e(x,t)$, $u_e(x,t)$, respectively. Define $V(x,t) := u_e(x,t) - U_e(x,t)$ which satisfies

$$\begin{cases} \left(\frac{1}{c}\frac{\partial}{\partial t} - D\Delta + \mu_a + \mu_f(x)\right) V = \mu_f(x)u_e(x,t), & (x,t) \in \Omega \times (0,T), \\ \nu \cdot \nabla V + \beta V = 0, & (x,t) \in \partial\Omega \times (0,T), \\ V(x,0) = 0, & x \in \Omega. \end{cases}$$

Then by the standard energy estimate [15] for the solution of the initial boundary value problem for the diffusion equation and using $\mu_f(x) \geq 0$, we have

$$\begin{aligned} & \frac{1}{2c}\|V(\cdot,T)\|^2_{L^2(\Omega)} + D\beta\|V\|^2_{L^2((0,T)\times\partial\Omega)} \\ & +D\int_0^T\int_\Omega |\nabla V|^2 \,\mathrm{d}x\mathrm{d}t + \mu_a\|V\|^2_{L^2((0,T)\times\Omega)} \\ \leq \; & \int_0^T\int_\Omega \mu_f(x)u_e(x,t)V(x,t)\,\mathrm{d}x\mathrm{d}t \\ \leq \; & \frac{1}{2}\mu_a\int_0^T\int_\Omega |V(x,t)|^2\,\mathrm{d}x\mathrm{d}t + \frac{1}{2\mu_a}\int_0^T\int_\Omega \mu_f^2(x)u_e^2(x,t)\,\mathrm{d}x\mathrm{d}t, \end{aligned}$$

which leads to

$$\|U_e - u_e\|^2_{L^2((0,T)\times\Omega)} \leq \int_{\Omega_0}\left(\frac{\mu_f(x)}{\mu_a}\right)^2\int_0^T u_e^2(x,t)\,\mathrm{d}t\mathrm{d}x, \tag{2.2.14}$$

by ignoring the first three terms in the left hand side and then moving the first term in the right hand side into the left hand side, noticing $\mu_f(x) \equiv 0$ in $\Omega \setminus \overline{\Omega}_0$.

Now let us estimate u_e in Ω_0. By (2.2.3) and Lemma 2.2, we have

$$u_e(x,t) = D \times K(x,x_s;t) = cDe^{-c\mu_a t}K^0(x,x_s;t), \tag{2.2.15}$$

where

$$K^0(x,x_s;t) := 2G_3(x-x_s,t) - 2\beta\int_0^{+\infty} e^{-\beta\zeta}G_3(x-x_s(\zeta),t)\,\mathrm{d}\zeta \tag{2.2.16}$$

with $x_s(\zeta) := (x_{s1}, x_{s2}, -\zeta)$ for $x_s = (x_{s1}, x_{s2}, 0) \in \partial\Omega$ by the definition. Since $\Omega_0 \Subset \Omega$ is bounded, the distance between Ω_0 and $\partial\Omega$ satisfying $dist(\Omega_0, \partial\Omega) \geq C_0 > 0$ for a constant $C_0 = C_0(\Omega_0) := \min_{x\in\Omega_0}\{dist(x,\partial\Omega)\}$ depending only on Ω_0. So we have $|x - x_s| \geq C_0 > 0$ and $x_3 > 0$ uniformly for all $x \in \Omega_0$ and $x_s \in \partial\Omega$. Hence, by the definition of $G_3(x,t)$, (2.2.16) yields for $x \in \Omega_0$ and $t > 0$ that

$$\begin{aligned} 0 &< K^0(x,x_s;t) \\ &\leq 2|G_3(x-x_s,t)| + 2\beta\int_0^{+\infty} e^{-\beta\zeta}|G_3(x-x_s(\zeta),t)|\,\mathrm{d}\zeta \\ &= \frac{2}{\sqrt{(4\pi cDt)^3}}\left(e^{-\frac{|x-x_s|^2}{4cDt}} + \beta\int_0^\infty e^{-\beta\zeta}e^{-\frac{|x-x_s|^2+\zeta^2+2\zeta x_3}{4cDt}}\,\mathrm{d}\zeta\right) \\ &\leq \frac{2}{\sqrt{(4\pi cDt)^3}}e^{-\frac{C_0^2}{4cDt}}\left(1 + \beta\int_0^\infty e^{-\beta\zeta}e^{-\frac{\zeta^2+2\zeta x_3}{4cDt}}\,\mathrm{d}\zeta\right) \\ &\leq \frac{2}{\sqrt{(4\pi cDt)^3}}e^{-\frac{C_0^2}{4cDt}}\left(1 + \beta\int_0^\infty e^{-\beta\zeta}\,\mathrm{d}\zeta\right) = \frac{4}{\sqrt{(4\pi cDt)^3}}e^{-\frac{C_0^2}{4cDt}} \end{aligned} \tag{2.2.17}$$

from $0 < e^{-\frac{\zeta^2+2\zeta x_3}{4cDt}} \le 1$ due to $\zeta \ge 0, x_3 > 0$. By (2.2.15), this estimate immediately implies for $x \in \Omega_0$ that

$$\begin{aligned} \|u_e(x,\cdot)\|^2_{L^2(0,T)} &= \|D \times K(x,x_s;\cdot)\|^2_{L^2(0,T)} \\ &\le \int_0^T \left(\frac{1}{\sqrt{4cD(\pi t)^3}} e^{-\frac{C_0^2}{4cDt} - c\mu_a t} \right)^2 \mathrm{d}t \\ &\le \int_0^T \left(\frac{1}{\sqrt{4cD(\pi t)^3}} e^{-\frac{C_0^2}{4cDt}} \right)^2 \mathrm{d}t, \end{aligned} \tag{2.2.18}$$

since $0 \le e^{-c\mu_a t} \le 1$ for $t \ge 0$.

Finally (2.2.14) and (2.2.18) lead to (2.2.12), which completes the proof. ☐

By the error estimate (2.2.12), it can be observed that the excitation u_e from the DE model (2.1.43), which is independent of $\mu_f(x)$, can approximate the excitation U_e satisfying (2.1.34) well, if $\mu_a^{-1}\|\mu_f\|_{L^2(\Omega_0)}$ is small.

2.2.3 Error estimation for inversion solutions

Now we can consider the linearized inverse problem (2.1.43)-(2.1.45) from the inversion input data specified in $\partial\Omega$. The *inversion solution* (i.e., the solution of inverse problem) from (2.1.43)-(2.1.45) is just an approximation to the nonlinear DE model constituted by (2.1.34)-(2.1.36) and (2.1.42). We will use the notation $\tilde{\mu}_f(x)$ for the inversion solution to the linearized model (2.1.43)-(2.1.45).

Now we can estimate the error $\mu_f(x) - \tilde{\mu}_f(x)$ by the following result.

Theorem 2.2. *Assume $\mu_f(x)$ is the inversion solution from the system constituted by (2.1.34)-(2.1.36) and (2.1.42), while $\tilde{\mu}_f(x)$ is the inversion solution from the linearized system (2.1.43)-(2.1.45). Then it follows that*

$$\|\tilde{\mu}_f - \mu_f\|_{L^1(\Omega_0)} \le \mu_a \tilde{C} \left\| \frac{\mu_f(\cdot)}{\mu_a} \right\|^2_{L^2(\Omega_0)} \tag{2.2.19}$$

with a constant $\tilde{C} = \tilde{C}(T, \Omega_0, \Gamma_0, c, D, \tau, \gamma) > 0$ for $\mu_f(x), \tilde{\mu}_f(x) \in L^2(\Omega)$ with known $\Gamma_0 \Subset \partial\Omega$ and support $\Omega_0 \Subset \Omega$.

Remark 2.2. *Since either $\mu_f(x)$ or $\tilde{\mu}_f(x)$ may not be unique for specified point source located at $x_s \in \partial\Omega$, the estimate (2.2.19) can be considered as an inequality which holds for any possible $\mu_f(x)$, $\tilde{\mu}_f(x)$.*

Proof. For fixed $x_s \in \partial\Omega$, define $Z(x,t;x_s) := u_m(x,t;x_s) - U_m(x,t;x_s)$, which satisfies

$$\begin{cases} \left(\frac{1}{c}\frac{\partial}{\partial t} - D\Delta + \mu_a\right) Z = \widetilde{S}(x,t), & (x,t) \in \Omega \times (0,T), \\ \nu \cdot \nabla Z + \beta Z = 0, & (x,t) \in \partial\Omega \times (0,T), \\ Z(x,0) = 0, & x \in \Omega, \end{cases} \tag{2.2.20}$$

with the source term expressed by

$$\begin{aligned} \widetilde{S}(x,t) &:= S[\tilde{\mu}_f, u_e](x,t) - S[\mu_f, U_e](x,t) \\ &= S[\tilde{\mu}_f - \mu_f, u_e](x,t) - S[\mu_f, u_e - U_e](x,t) \end{aligned} \tag{2.2.21}$$

from straightforward computations. By Lemma 2.2, the solution to (2.2.20) is

$$Z(x,t;x_s)=\int_0^T\int_{\Omega_0}K(x,y;t-s)\widetilde{S}(y,s)\,\mathrm{d}y\mathrm{d}s,\quad (x,t)\in\overline{\Omega}\times[0,T]. \tag{2.2.22}$$

On the other hand, we have the extra boundary condition

$$Z(x,t;x_s)=0,\quad x\in\partial\Omega, t\in(0,T), \tag{2.2.23}$$

since we apply the same inversion input data for u_m and U_m. So (2.2.21)-(2.2.23) lead to the following identity

$$\begin{aligned}&\int_0^T\int_{\Omega_0}K(x,y;t-s)S[\tilde{\mu}_f-\mu_f,u_e](y,s)\,\mathrm{d}y\mathrm{d}s\\ =\ &\int_0^T\int_{\Omega_0}K(x,y;t-s)S[\mu_f,u_e-U_e](y,s)\,\mathrm{d}y\mathrm{d}s,\quad (x,t)\in\partial\Omega\times[0,T].\end{aligned} \tag{2.2.24}$$

For $h_\tau(t):=\frac{\gamma}{\tau}e^{-\frac{t}{\tau}}$, define the operator

$$I[u_e](x,t):=h_\tau(t)*_t u_e(x,t)=\int_0^t h_\tau(s)u_e(x,t-s)\,\mathrm{d}s$$

for $x\in\bar{\Omega}$. Then, by the expression of $S[\cdot,\cdot](x,t)$ in (2.1.36), we have

$$S[\mu_f,u_e](x,t)=\mu_f(x)I[u_e](x,t). \tag{2.2.25}$$

Notice $u_e\geq 0$, $K(x,y;t-s)>0$ for $t>s$ and $K(x,y;t-s)\equiv 0$ for $t\leq s$, it follows by (2.2.24) and Theorem 2.1 that

$$\begin{aligned}&\int_0^t\int_{\Omega_0}K(x,y;t-s)S[|\tilde{\mu}_f-\mu_f|,u_e](y,s)\,\mathrm{d}y\mathrm{d}s\\ &\leq\left(\int_0^t\int_{\Omega_0}[K(x,y;t-s)\mu_f(y)]^2\,\mathrm{d}y\mathrm{d}s\right)^{1/2}\|I[u_e-U_e]\|_{L^2((0,T),L^2(\Omega_0))}\\ &\leq\left(\int_0^t\int_{\Omega_0}[K(x,y;t-s)\mu_f(y)]^2\,\mathrm{d}y\mathrm{d}s\right)^{1/2}\|h_\tau\|_{L^1(0,T)}\,\|u_e-U_e\|_{L^2((0,T),L^2(\Omega))}\\ &\leq C(\Omega_0,T,c,D)\,\|h_\tau\|_{L^1(0,T)}\left(\int_0^t\int_{\Omega_0}[K(x,y;t-s)\mu_f(y)]^2\,\mathrm{d}y\mathrm{d}s\right)^{1/2}\left\|\frac{\mu_f(\cdot)}{\mu_a}\right\|_{L^2(\Omega_0)}\\ &=C_1(\Omega_0,T,c,D,\tau,\gamma)\left(\int_0^t\int_{\Omega_0}[K(x,y;t-s)\mu_f(y)]^2\,\mathrm{d}y\mathrm{d}s\right)^{1/2}\left\|\frac{\mu_f(\cdot)}{\mu_a}\right\|_{L^2(\Omega_0)}\end{aligned} \tag{2.2.26}$$

for $(x,t)\in\partial\Omega\times[0,T]$, where the positive constant $C_1:=C(\Omega_0,T,c,D)\times\|h_\tau\|_{L^1(0,T)}$ with $C>0$ defined by (2.2.13).

We note that $x\in\partial\Omega$ and $y\in\Omega_0$. Likewise we did in (2.2.17), we have for all $x\in\partial\Omega, y\in\Omega_0$ that

$$0\leq K(x,y;t-s)\leq\frac{1}{\sqrt{4c\pi^3D^3(t-s)^3}}e^{-\frac{C_0^2}{4cD(t-s)}} \tag{2.2.27}$$

with $C_0 := C_0(\Omega_0) := \min_{y\in\Omega_0}\{dist(y,\partial\Omega)\}$. Then (2.2.26) becomes

$$\begin{aligned}
&\int_0^t\int_{\Omega_0} K(x,y;t-s)S[|\tilde{\mu}_f-\mu_f|,u_e](y,s)\,\mathrm{d}y\mathrm{d}s\\
\leq\ & \frac{C_1}{\sqrt{4c\pi^3D^3}}\left(\int_0^t \frac{1}{s^3}e^{-\frac{C_0^2}{2cDs}}\,\mathrm{d}s\right)^{1/2}\|\mu_f(\cdot)\|_{L^2(\Omega_0)}\left\|\frac{\mu_f(\cdot)}{\mu_a}\right\|_{L^2(\Omega_0)}\\
\leq\ & C_2\mu_a\left\|\frac{\mu_f(\cdot)}{\mu_a}\right\|^2_{L^2(\Omega_0)} \qquad (2.2.28)
\end{aligned}$$

with a constant $C_2 = C_2(T,\Omega_0,c,D,\tau,\gamma) > 0$.

This estimate holds for all $x\in\partial\Omega$ by (2.2.23). To get a positive lower bound on the left hand side of (2.2.28), we consider (2.2.28) for x in a bounded domain of $\partial\Omega$. For all $x=(\tilde{x},0), x_s=(\tilde{x}_s,0)\in\Gamma_0\Subset\partial\Omega$ and all $y=(\tilde{y},0)\in\Omega_0\Subset\Omega$ satisfying

$$|\tilde{x}-\tilde{y}|,\ |\tilde{x}_s-\tilde{y}|\leq c_*(\Omega_0,\Gamma_0),\quad 0<C_0\leq y_3\leq\tilde{C}_0 \qquad (2.2.29)$$

with $\tilde{C}_0=\tilde{C}_0(\Omega_0):=\max_{y\in\Omega_0}\{dist(y,\partial\Omega)\}$, we have by Corollary 2.1 that

$$\begin{aligned}
K(x,y;t-s) &= \frac{ce^{-c\mu_a(t-s)}}{\sqrt{(4\pi cD(t-s))^3}}e^{-\frac{|\tilde{x}-\tilde{y}|^2}{4cD(t-s)}}K_3(0,y_3;t-s)\\
&\geq \frac{ce^{-c\mu_a(t-s)}}{\sqrt{(4\pi cD(t-s))^3}}e^{-\frac{c_*^2(\Omega_0,\Gamma_0)}{4cD(t-s)}}K_3^{\min}(0,y_3;t-s),\quad t>s
\end{aligned}\qquad (2.2.30)$$

and

$$\begin{aligned}
K(y,x_s;t') &= \frac{ce^{-c\mu_a t'}}{\sqrt{(4\pi cDt')^3}}e^{-\frac{|\tilde{y}-\tilde{x}_s|^2}{4cDt'}}K_3(y_3,0;t')\\
&\geq \frac{ce^{-c\mu_a t'}}{\sqrt{(4\pi cDt')^3}}e^{-\frac{c_*^2(\Omega_0,\Gamma_0)}{4cDt'}}K_3^{\min}(y_3,0;t'),\quad t'>0,
\end{aligned}\qquad (2.2.31)$$

where we define

$$\begin{aligned}
K_3^{\min}(t) &= K_3^{\min}(0,y_3;t)=K_3^{\min}(y_3,0;t)\\
&= \min_{y_3\in[C_0,\tilde{C}_0]}\left\{2e^{-\frac{y_3^2}{4cDt}}-2\beta\sqrt{\pi cDt}e^{\beta y_3+\beta^2cDt}\operatorname{erfc}\left(\frac{y_3+2\beta cDt}{\sqrt{4cDt}}\right)\right\}>0.
\end{aligned}$$

Hence we have

$$\begin{aligned}
K(x,y;t-s)I[u_e](y,s) &= D\times K(x,y;t-s)\int_0^s h_\tau(s-t')K(y,x_s;t')\,\mathrm{d}t'\\
&\geq \frac{Dce^{-c\mu_a(t-s)}}{\sqrt{(4\pi cD(t-s))^3}}e^{-\frac{c_*^2(\Omega_0,\Gamma_0)}{4cD(t-s)}}K_3^{\min}(t-s)\\
&\quad\times\int_0^s h_\tau(s-t')\frac{ce^{-c\mu_a t'}}{\sqrt{(4\pi cDt')^3}}e^{-\frac{c_*^2(\Omega_0,\Gamma_0)}{4cDt'}}K_3^{\min}(t')\,\mathrm{d}t'
\end{aligned}$$

for all $y \in \overline{\Omega}_0$. Using this lower bound, the left hand side of (2.2.28) for $x \in \Gamma_0$ can be estimated as

$$\begin{aligned}
& \int_0^t \int_{\Omega_0} K(x,y;t-s) S[|\tilde{\mu}_f - \mu_f|, u_e](y,s)\, \mathrm{d}y \mathrm{d}s \\
= \; & \int_0^t \int_{\Omega_0} |\tilde{\mu}_f(y) - \mu_f(y)| K(x,y;t-s) I[u_e](y,s)\, \mathrm{d}y \mathrm{d}s \\
\geq \; & D \times N(t) *_t (h_\tau(t) *_t N(t)) \int_{\Omega_0} |\tilde{\mu}_f(y) - \mu_f(y)|\, \mathrm{d}y \\
=: \; & D \times M(t) \int_{\Omega_0} |\tilde{\mu}_f(y) - \mu_f(y)|\, \mathrm{d}y,
\end{aligned} \tag{2.2.32}$$

where $N(t) := \frac{ce^{-c\mu_a t}}{\sqrt{(4\pi c D t)^3}} e^{-\frac{c_*^2(\Omega_0,\Gamma_0)}{4cDt}} K_3^{\min}(t)$. By (2.2.28) and (2.2.32), we have

$$D\, M(t) \int_{\Omega_0} |\tilde{\mu}_f(y) - \mu_f(y)|\, \mathrm{d}y \leq C_3 \mu_a \left\| \frac{\mu_f(\cdot)}{\mu_a} \right\|^2_{L^2(\Omega_0)}.$$

Since $0 \leq M(t) \not\equiv 0$ in $[0,T]$, we have by integrating this estimate in $(x,t) \in \Gamma_0 \times (0,T)$ that

$$\int_{\Omega_0} |\tilde{\mu}_f(y) - \mu_f(y)|\, \mathrm{d}y \leq \mu_a \widetilde{C} \left\| \frac{\mu_f(\cdot)}{\mu_a} \right\|^2_{L^2(\Omega_0)},$$

with a positive constant $\widetilde{C} := \widetilde{C}(T, \Omega_0, \Gamma_0, c, D, \tau, \gamma)$. The proof is complete. ☐

This result shows that, in the case of $\|\mu_f\|_{L^2(\Omega_0)} \ll \mu_a$, the linearized model for recovering $\mu_f(x)$ is reasonable, with the L^1 error estimate bounded by $\left\| \frac{\mu_f(\cdot)}{\mu_a} \right\|^2_{L^2(\Omega_0)}$.

2.3 Numerical Verifications for Model Approximation

The linearized inverse problem in terms of $u_m(x,t)$ for identifying $\mu_f(x)$ is obtained by two steps, firstly transform the RTE system (2.1.1)-(2.1.2) for (Φ_e, Φ_m) to the diffusion model for (U_e, U_m) under the approximate expansions (2.1.13)-(2.1.14), and then ignore $\mu_f(x)$ for the excitation field U_e to consider the system (u_e, u_m) for recovering $\mu_f(x)$ linearly. In other words, we have in fact the model approximation errors due to the transform of the RTE model to DE model and the linearizing error from the approximation of U_e by u_e. Although the first approximation has been applied extensively [19, 30], and the error for the second approximation is estimated in the above section, here we give some numerical tests to partially verify the total error from two approximations. The verification is based on the comparisons between u_m and Φ_m in $\partial\Omega$ for small $\mu_f(x)$, where Φ_m are generated by approximating the experimental condition for the RTE model (2.1.1)-(2.1.2) with this nonzero $\mu_f(x)$ using a *Monte Carlo* (MC) simulation. Such an error represents the total error by two approximations, namely, the error of approximating RTE model by DE model and the error by linearizing process for U_e, from which we consider the linear inverse problem in terms of (u_e, u_m).

By the diffusion approximation developed in section 2.1.4, (u_e, u_m) and (Φ_e, Φ_m) in the boundary have the relations

$$u_e(x,t) \approx C^* \int_{\mathbb{S}^2_-} \tilde{\Phi}_e(x, \tilde{\theta}, t)\, \mathrm{d}\tilde{\theta}, \quad (x,t) \in \partial\Omega \times (0,T), \tag{2.3.1}$$

$$u_m(x,t) \approx C^* \int_{\mathbb{S}^2_-} \tilde{\Phi}_m(x,\tilde{\theta},t)\,\mathrm{d}\tilde{\theta}, \quad (x,t) \in \partial\Omega \times (0,T), \tag{2.3.2}$$

where the constant C^* is given in (2.1.41), the outgoing radiance $\tilde{\Phi}_e(x,\tilde{\theta},t)$ and $\tilde{\Phi}_m(x,\tilde{\theta},t)$ along direction $\tilde{\theta} \in \mathbb{S}^2_-$ depend on the relative refractive index $\frac{n_2}{n_1}$, the Fresnel reflection coefficient, inside radiance $\Phi_e(x,\theta,t)$ and $\Phi_m(x,\theta,t)$, respectively, as shown in (2.1.10). Then we will validate the model approximation numerically by comparing two sides of (2.3.1) and (2.3.2) for two observation points in $\partial\Omega$.

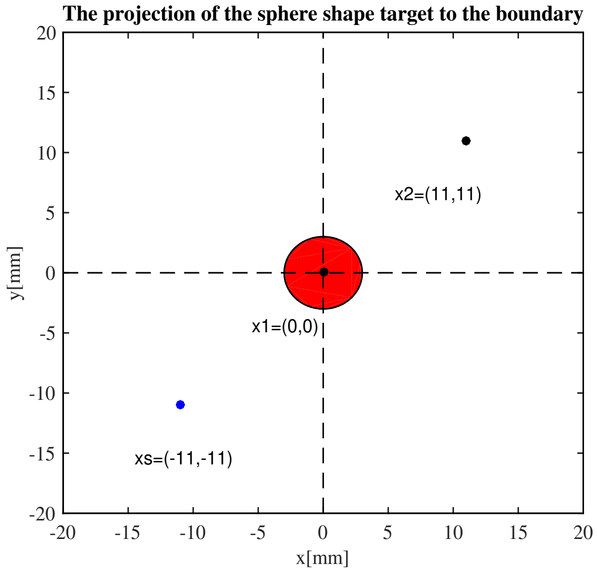

FIGURE 2.1: Horizontal projection of the configuration: the red circle with center $(0,0)$ is the projection of a sphere target to the boundary $\partial\Omega$, the boundary source locates at xs, and the measurements are taken at points $x1$ and $x2$.

For parameters configuration in the MC simulation, we take

$$c = 0.219 \text{ mm/ps},\ \mu_a = 0.01 \text{ mm}^{-1},\ \mu_s = 10 \text{ mm}^{-1},\ g = 0.9,\ \beta = 0.5493 \text{ mm}^{-1} \tag{2.3.3}$$

and $n_1 = 1.37, n_2 = 1$, which are typical values of biological tissues [66]. We set $\gamma = 1$. Now we are ready to give some numerical implementations for the following example.

Example 2.1. *The geometrical configuration is shown in Figure 2.1, where a sphere-shaped fluorosence target with diameter 6 mm and absorption coefficient* $\mu_f(x) = 0.0017$ *mm*$^{-1}$ *is located at* $(0,0,11)$. *We put the boundary point source at* $x_s = (-11,-11)$ *and two boundary measurement detectors at* $x_1 = (0,0)$ *and* $x_2 = (11,11)$ *for* $t \in (0,T)$ *with* $T = 3.3$ *ns for measurement time.*

Simulating RTE using Monte Carlo method

Monte Carlo (MC) simulations definitely are powerful in that they are easy to implement and can deal with very complex geometries. A major drawback is their huge computational requirements. Typical MC simulations of optical diffusion can take several days or weeks of computation.

The values in the right hand side of (2.3.1) and (2.3.2) will be obtained from the MC method simulating the physical process, which traces the photons in the diffusive medium. The idea was firstly used for the steady state light transport with a multi-layered system by Wang [72] and similarly for the time-domain transport with a semi-infinite system [71] and now widely used to test theories and experiments. Our simulation was conducted by a modified code for the time-domain fluorescence based on the code developed for general purpose computing on graphics processing unit (GPGPU) [73]. Firstly, the excitation photon is injected from the source point and then randomly travels until absorbed by the background absorber or the fluorophore at the target. If the excitation photon is absorbed by the fluorophore, the excitation photon is eliminated and the fluorescence photon is generated at the point. Then, the fluorescence photon is traveling until absorbed or exited from the boundary. For the detection of the photon, the travel distance from the injection point to the exit point together with the exit point itself is recorded, but the exit angle is not recorded. Then, the histogram of the photons detected with respect to the distance, which is corresponding to the time, at a small area is obtained by repeating the above process. The detail simulation method can be found in paper [67]. Therefore, the objective of the simulation is not to directly calculate the right hand side of (2.3.1) and (2.3.2) but to approximate the experimental condition for this system.

Numerical verification for excitation

We first evaluate the relation (2.3.1) for excitation light. The values of two sides of (2.3.1) at observation points x_1 and x_2 in time interval $(0,T)$, after taking logarithm, are shown in Figure 2.2 (a), where an artificial constant has been introduced to re-scale the simulation data, representing the signal collection efficiency of measurements. This constant scaled the peak of the results. It can be observed that the red and green curves increase slightly faster than the corresponding curves shown by blue and black colors at the early time, which represent the limitation effect of DE approximation. At most of the time instants $t \in (0,T)$, two sides of (2.3.1) are consistent very well. To describe the inconsistency of two sides of (2.3.1) quantitatively, we compute the relative error defined by

$$Err_i^e(t) := \frac{C^* \int_{\mathbb{S}^2_-} \tilde{\Phi}_e(x_i,\tilde{\theta},t)\,\mathrm{d}\tilde{\theta} - u_e(x_i,t)}{u_e(x_i,t)}, \quad t \in (0,T)$$

at points x_i for $i = 1, 2$, which are shown in Figure 2.2 (b) and Figure 2.2 (c), respectively.

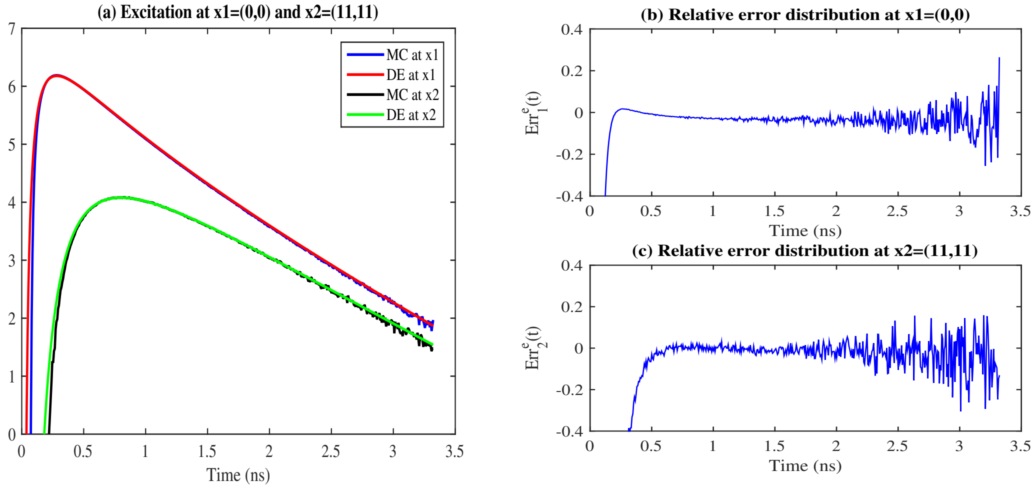

FIGURE 2.2: Comparisons of two sides of (2.3.1) at two points x_1 and x_2. Left: Distributions of two sides at two points after taking logarithm; Right: Relative error at two points.

Numerical verification for emission

We next evaluate the relation (2.3.2) for the emission light. Similarly, the values of two sides of (2.3.2) at two observation points x_1 and x_2 in time interval $(0, T)$, after taking logarithm, are shown in Figure 2.3 (a). It should be pointed out that, in our simulations, we in fact take the lifetime $\tau = 0$. Such a comparison can also reveal the validation of (2.3.2) with any $\tau > 0$, since two sides of (2.3.2) for any fixed $\tau > 0$ are just the convolutions of $\frac{1}{\tau}e^{-\frac{t}{\tau}}$ with those values for $\tau = 0$ (see (2.2.9) below). It can be observed from Figure 2.3 (a) that the red and green curves increase slightly faster than the corresponding curves shown by blue and black colors at the early time, which is consistent to the limitation effect of DE approximation what we observed in Figure 2.2. Nevertheless, at most of the time instants $t \in (0, T)$, except small t and large t, two sides of (2.3.2) are consistent very well. To describe the inconsistency of two sides of (2.3.2) quantitatively, we compute the relative error defined by

$$Err_i^m(t) := \frac{C^* \int_{\mathbb{S}^2_-} \tilde{\Phi}_m(x_i, \tilde{\theta}, t)\, \mathrm{d}\tilde{\theta} - u_m(x_i, t)}{u_m(x_i, t)}, \quad t \in (0, T)$$

at points x_i for $i = 1, 2$, which are shown in Figure 2.3 (b) and Figure 2.3 (c), respectively.

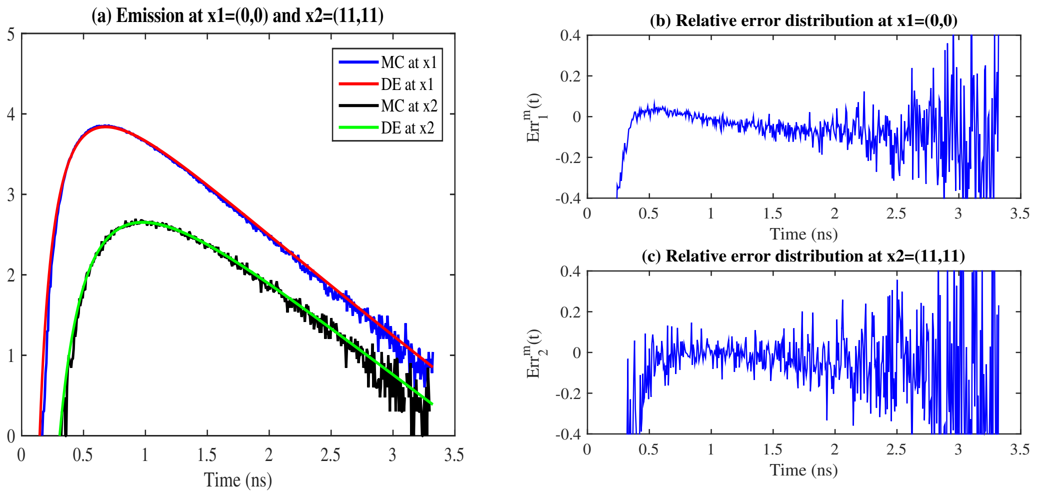

FIGURE 2.3: Comparisons of two sides of (2.3.2) at two points x_1 and x_2. Left: Distributions of two sides at two points after taking logarithm; Right: Relative error at two points.

An interesting observation on $Err_i^m(t)$ (see Figure 2.3 (b) and Figure 2.3 (c)) is that, the relative errors are always large for either small t or large t, while the errors in the interior part of $(0, T)$ are relatively small. The deviation, which is also visually seen in Figure 2.3 (a), in the small time region is speculated from the diffusion approximation, which can not model the finite time of the transportation. In the large time region, the excitation field is weakened by the absorption from the object and eventually the fluorescence intensity is smaller than that calculated by the DE model, ignoring the absorption μ_f from the object in the excitation. Due to this reason, when we do simulations for our inverse problem, we can ignore the inversion input data for t either large or small. This is also one reason why we always take the time points around peak time of the emission as our measurement data when we consider the numerical inversion in the Chapter 6.

Remark 2.3. *For the above implementations, the absorption of background is* $\mu_a = 0.01\ mm^{-1}$ *and the absorption of fluorescence target is* $\mu_f = 0.0017\ mm^{-1}$*. In some* *sense, it is very hard to assert* $\|\mu_f\|_{L^2(\Omega_0)} \ll \mu_a$ *quantitatively. However, from Figure 2.2 and Figure 2.3, we have the observation that the errors for excitation field and emission field by ignoring* μ_f *in (2.1.34) are indeed small, if* $\|\mu_f\|_{L^2(\Omega_0)}$ *is not large compared with* μ_a *and the size of the fluorescence target is small, which partially supports our theoretical result in Theorem 2.1, where the error* $U_e - u_e$ *by the average norm is estimated. Here we showed this error distribution with respect to time at two fixed observation points.*

2.4 Chapter Summary

We considered the DE model for identifying the absorption coefficient $\mu_f(x)$ of fluorophore from boundary measurement data. Although such an imaging model, as an approximation to RTE model due to the approximate expansions of excitation and emission together with the linearization process for imaging, has been widely applied in engineering communities, there is no rigorous mathematical analysis on the above process. Our novel contributions in this chapter are as follows.

1. We establish the error estimate rigorously for the excitation field due to ignoring $\mu_f(x)$ and the corresponding error estimate for recovering $\mu_f(x)$ from the linearized DE model;
2. We present numerical implementations to partially support our theoretical estimates, by comparing the excitation fields and emission fields on the boundary for DE model and RTE model.

Chapter 3

Parameter Identification for FDOT

For the linearized DE model obtained in Chapter 2, we consider the parameter identification problems arising from FDOT. In section 3.1, based on the analytical expressions of excitation and emission, the identifiability of the absorption coefficient of fluorophores is rigorously analyzed for absorption coefficient in special form. Also, based on the analytical expression of emission, we show its long-time asymptotic behavior in section 3.2, by which we can estimate the fluorescence lifetime. Finally, we give some conclusion and remark in section 3.3.

3.1 Identifiability of the Absorption Coefficient

We have derived the linearized inverse model in terms of $u_m(x,t;x_s)$ with known excitation field $u_e(x,t;x_s)$ generated from (2.1.43) depending on the boundary point source $\delta(x-x_s)\delta(t)$. Then a mathematically idealized version of our linear inverse problem is to recover $\tilde{\mu}_f(x)$ from specified data

$$u_m(x,t;x_s) := h(x,t;x_s), \quad (x,t) \in \partial\Omega \times (0,T), \tag{3.1.1}$$

where $u_m(x,t;x_s)$ is the solution to (2.1.44) with the source term

$$S[\tilde{\mu}_f, u_e](x,t) := \gamma\tilde{\mu}_f(x) \int_0^t \frac{e^{-(t-t')/\tau}}{\tau} u_e(x,t';x_s)\,\mathrm{d}t' \tag{3.1.2}$$

for known u_e. By Lemma 2.2, we have from (3.1.1) that

$$\int_{\Omega_0} \tilde{\mu}_f(y) \int_0^t \int_0^s \frac{e^{-(s-t')/\tau}}{\tau} K(x,y;t-s)K(y,x_s;t')\,\mathrm{d}t'\mathrm{d}s\mathrm{d}y = \frac{1}{\gamma D} h(x,t;x_s) \tag{3.1.3}$$

for $(x,t;x_s) \in \partial\Omega \times (0,T) \times \partial\Omega$.

The essence of this problem is to identify the three-dimensional absorption function $\tilde{\mu}_f(x)$ with known compact support Ω_0 from the measurement data only on the horizontal plane $x_3 = 0$. In general, it is impossible to uniquely identify $\tilde{\mu}_f(x)$ even if we put the point sources on the whole boundary $\partial\Omega$. This is because the measurements on $x_3 = 0$ are just back scattering data which reveal the horizontal information about $\tilde{\mu}_f(x)$ and are not enough to identify its distribution along vertical direction. So it is important to clarify to what extent we can get the uniqueness of this inverse problem.

Since both the source locations x_s and the observation points x are optional in boundary $\partial\Omega$, we need to consider the uniqueness of the solution $\tilde{\mu}_f(y)$ to (3.1.3) from known $h(x,t;x_s)$ for suitable boundary points $x, x_s \in \partial\Omega$. However, the equation (3.1.3) is an integral equation of the first kind with respect to $\tilde{\mu}_f(x)$ defined in $\mathbb{R}^3_+$, in general, there is no uniqueness for the solution. Moreover, the convolution structure with the function $\frac{1}{\tau}e^{-\frac{t}{\tau}}$ makes the kernel more smooth.

Thus, we consider a particular case of the model (2.1.44) for $u_m(x,t;x_s)$. Let $\widetilde{u}_m(x,t;x_s)$ denote the photon density of *zero-lifetime emission light*, i.e., the fluorescence lifetime in the source term $S[\tilde{\mu}_f,u_e](x,t)$ is $\tau=0$. For $t\in(0,T)$, integrating (3.1.2) by parts with respect to s gives

$$\begin{aligned}S[\tilde{\mu}_f,u_e](x,t;\tau) &= \frac{\gamma\tilde{\mu}_f(x)}{\tau}\int_0^t e^{-(t-s)/\tau}u_e(x,s;x_s)\,\mathrm{d}s\\ &= \gamma\tilde{\mu}_f(x)\left(u_e(x,t;x_s)-u_e(x,0;x_s)e^{-\frac{t}{\tau}}-\int_0^t\frac{\partial u_e(x,s;x_s)}{\partial s}e^{-\frac{t-s}{\tau}}\,\mathrm{d}s\right).\end{aligned}$$

Since $x_s\in\partial\Omega$,

$$u_e(x,t;x_s)\in C^\infty(\Omega\times[0,T]) \tag{3.1.4}$$

due to (2.2.4) and (2.2.8). Hence $\frac{\partial u_e(x,s;x_s)}{\partial s}$ is bounded with respect to $s\in(0,T)$. Hence there exists a constant $C>0$ such that

$$\left|\int_0^t\frac{\partial u_e(x,s;x_s)}{\partial s}e^{-\frac{t-s}{\tau}}\,\mathrm{d}s\right|\le C\int_0^t e^{-\frac{t-s}{\tau}}\,\mathrm{d}s=C\tau(1-e^{-\frac{t}{\tau}}).$$

Together with this and $\lim_{\tau\to0+}e^{-\frac{t}{\tau}}=0$ for $t>0$, we immediately have

$$\lim_{\tau\to0+}S[\tilde{\mu}_f,u_e](x,t;\tau)=\gamma\tilde{\mu}_f(x)u_e(x,t;x_s). \tag{3.1.5}$$

Thus, the photon density of zero-lifetime emission light $\widetilde{u}_m$ satisfies

$$\begin{cases}\left(\frac{1}{c}\frac{\partial}{\partial t}-D\Delta+\mu_a\right)\widetilde{u}_m=\gamma\tilde{\mu}_f(x)u_e(x,t;x_s), & (x,t)\in\Omega\times(0,T),\\ \widetilde{u}_m(x,0)=0, & x\in\Omega,\\ \nu\cdot\nabla\widetilde{u}_m+\beta\widetilde{u}_m=0, & (x,t)\in\partial\Omega\times(0,T)\end{cases} \tag{3.1.6}$$

with the analytical expression

$$\widetilde{u}_m(x,t;x_s)=\gamma D\int_0^t\int_{\Omega_0}\tilde{\mu}_f(y)K(x,y;t-s)K(y,x_s;s)\,\mathrm{d}y\mathrm{d}s,\quad (x,t)\in\overline{\Omega}\times[0,T], \tag{3.1.7}$$

which implies that the solution $u_m(x,t;x_s)$ to (2.1.44) is the convolution of zero-lifetime emission $\widetilde{u}_m(x,t;x_s)$ with the lifetime function $\frac{1}{\tau}e^{-t/\tau},\tau>0$, i.e.,

$$u_m(x,t;x_s)=\int_0^t\frac{1}{\tau}e^{-s/\tau}\,\widetilde{u}_m(x,t-s;x_s)\,\mathrm{d}s,\ \ \tau>0,\ \ (x,t)\in\overline{\Omega}\times[0,T]. \tag{3.1.8}$$

On the other hand, in the sense of $\int_0^\infty\frac{1}{\tau}e^{-\frac{t}{\tau}}\,\mathrm{d}t=1$ for any fixed small $\tau>0$ and

$$\lim_{\tau\to0+}\frac{1}{\tau}e^{-\frac{t}{\tau}}=\begin{cases}0, & t>0,\\ +\infty, & t=0,\end{cases}$$

we can consider $\frac{1}{\tau}e^{-\frac{t}{\tau}}$ for small $\tau>0$ as the approximation to $\delta(t)$ such that we have the relation

$$\lim_{\tau\to0+}u_m(x,t;x_s)=\widetilde{u}_m(x,t;x_s). \tag{3.1.9}$$

Now we are ready to consider the identifiability of our linearized inverse absorption coefficient problem for the zero-lifetime case. That is, we transform the integral equation of the first kind with respect to $\tilde{\mu}_f(x)$ given by (3.1.3) into

$$\int_{\Omega_0} \tilde{\mu}_f(y) \int_0^t K(x,y;t-s)K(y,x_s;s)\,\mathrm{d}s\mathrm{d}y = \frac{1}{\gamma D}\tilde{h}(x,t;x_s), \tag{3.1.10}$$

where $\tilde{h}(x,t;x_s)$ is the observation corresponding to the case $\tau = 0$ in (2.1.3). The following result asserts, in general, only the horizontal information of $\tilde{\mu}_f(x)$ can be determined from our linearized inversion model [65].

Theorem 3.1. *Assume that $\tilde{\mu}_f(x)$ for $x = (\tilde{x}, x_3) \in \mathbb{R}^2 \times \mathbb{R}^1_+$ has the variable separation form $\tilde{\mu}_f(x) = p(\tilde{x})q(x_3)$ with known $q(x_3)$ and the convolution kernel $\frac{1}{\tau}e^{-t/\tau}$ in (3.1.3) is replaced by the impulse function $\delta(t)$. Then $p(\tilde{x})$ can be uniquely determined from one of the following observation data:*

- *1. $\{\tilde{h}(x,t;x_s), x \in \partial\Omega, t \in (t_0 - \epsilon_0, t_0 + \epsilon_0)\}$ for one fixed point $x_s \in \partial\Omega$ and $t_0 > 0$;*
- *2. $\{\tilde{h}(x,t;x_s), x_s \in \partial\Omega, t \in (t_0 - \epsilon_0, t_0 + \epsilon_0)\}$ for one fixed point $x \in \partial\Omega$ and $t_0 > 0$,*

where $\epsilon_0 > 0$ may be arbitrarily small in each case.

Proof. By the assumptions, the equation (3.1.10) can be rewritten as

$$\int_{\mathbb{R}^2} p(\tilde{y}) \int_{\mathbb{R}+} q(y_3)\mathcal{K}(\tilde{x}, \tilde{x}_s, t, y_3)\,\mathrm{d}y_3\mathrm{d}\tilde{y} = R(\tilde{x}, t; \tilde{x}_s), \tag{3.1.11}$$

where the kernel is

$$\mathcal{K}(\tilde{x}, \tilde{x}_s, t, y_3) := e^{-c\mu_a t}\int_0^t G_2(\tilde{y} - \tilde{x}_s, s)\widetilde{K}_3(y_3; s)G_2(\tilde{x} - \tilde{y}, t-s)\widetilde{K}_3(y_3; t-s)\,\mathrm{d}s \tag{3.1.12}$$

with

$$\widetilde{K}_3(y_3; t-s) := \frac{1}{\sqrt{4\pi cD(t-s)}}K_3(y_3, 0; t-s) = \frac{1}{\sqrt{4\pi cD(t-s)}}K_3(0, y_3; t-s),$$

and

$$R(\tilde{x}, t; \tilde{x}_s) := \frac{1}{c^2\gamma D}\tilde{h}(x,t;x_s), \quad x_s = (\tilde{x}_s, 0), x = (\tilde{x}, 0). \tag{3.1.13}$$

Since $p(\tilde{x})q(x_3)$ has support Ω_0, (3.1.11) becomes

$$\int_{\mathbb{R}^2} p(\tilde{y}) \int_0^t G_2(\tilde{y} - \tilde{x}_s, s)G_2(\tilde{x} - \tilde{y}, t-s)W[q](s, t-s)\,\mathrm{d}s\mathrm{d}\tilde{y} = e^{c\mu_a t}R(\tilde{x}, t; \tilde{x}_s), \tag{3.1.14}$$

where the known function

$$W[q](s, t-s) := \int_{\mathbb{R}_+} q(y_3)\widetilde{K}_3(y_3; s)\widetilde{K}_3(y_3; t-s)\,\mathrm{d}y_3. \tag{3.1.15}$$

By operating $\frac{\partial}{\partial t} - cD\Delta_{\tilde{x}}$ to two sides of (3.1.14), we have

$$\begin{aligned} & p(\tilde{x})G_2(\tilde{x} - \tilde{x}_s, t)W[q](t, 0) + \\ & \int_{\mathbb{R}^2} p(\tilde{y}) \int_0^t G_2(\tilde{y} - \tilde{x}_s, s)G_2(\tilde{x} - \tilde{y}, t-s)\frac{\partial W[q](s, t-s)}{\partial t}\,\mathrm{d}s\mathrm{d}\tilde{y} \\ = & \left(\frac{\partial}{\partial t} - cD\,\Delta_{\tilde{x}}\right)(e^{c\mu_a t}R(\tilde{x}, t; \tilde{x}_s)), \end{aligned} \tag{3.1.16}$$

where we have used $\left(\frac{\partial}{\partial t} - cD\,\Delta_{\tilde{x}}\right) G_2(\tilde{x}-\tilde{y},t-s) = \delta(\tilde{x}-\tilde{y})\delta(t-s)$ and $G_2(\tilde{x}-\tilde{y},t-s) \equiv 0$ for $s \geq t$. On the other hand, rewriting (3.1.14) as

$$\int_{\mathbb{R}^2} p(\tilde{y}) \int_0^T G_2(\tilde{y}-\tilde{x}_s, t-s) G_2(\tilde{x}-\tilde{y}, s) W[q](t-s,s)\,\mathrm{d}s\mathrm{d}\tilde{y} = e^{c\mu_a t} R(\tilde{x}, t; \tilde{x}_s)$$

and then applying the operator $\frac{\partial}{\partial t} - cD\Delta_{\tilde{x}_s}$ to both sides, we have

$$\begin{aligned} & p(\tilde{x}_s) G_2(\tilde{x}-\tilde{x}_s, t) W[q](0,t) + \\ & \int_{\mathbb{R}^2} p(\tilde{y}) \int_0^t G_2(\tilde{y}-\tilde{x}_s, s) G_2(\tilde{x}-\tilde{y}, t-s) \frac{\partial W[q](s,t-s)}{\partial t}\,\mathrm{d}s\mathrm{d}\tilde{y} \\ = {} & \left(\frac{\partial}{\partial t} - cD\,\Delta_{\tilde{x}_s}\right)\left(e^{c\mu_a t} R(\tilde{x}_s, \tilde{x}, t)\right). \end{aligned} \tag{3.1.17}$$

Hence, for known $q(x_3)$, we get the integral equations (3.1.16) and (3.1.17) for $p(\tilde{x})$ and $p(\tilde{x}_s)$, respectively.

Now we analyze the solvability of (3.1.16) and (3.1.17), which depends on the behavior of $W[q](t,0)$ $(W[q](0,t))$. In terms of the definitions of (2.2.5), we decompose $\widetilde{K}_3(y_3;t) = 2G_1(y_3,t)\mathcal{K}_3(y_3;t)$ with

$$\begin{aligned} \mathcal{K}_3(y_3;t) : &= 1 - \beta\sqrt{4\pi cDt}\frac{e^{\beta y_3 + \beta^2 cDt + \frac{y_3^2}{4cDt}}}{2} \int_{\frac{y_3+2\beta cDt}{\sqrt{4cDt}}}^{+\infty} e^{-s^2}\,\mathrm{d}s \\ &= 1 - \beta\sqrt{\pi cDt}\, e^{\left(\frac{y_3+2\beta cDt}{\sqrt{4cDt}}\right)^2} \int_{\frac{y_3+2\beta cDt}{\sqrt{4cDt}}}^{+\infty} e^{-s^2}\,\mathrm{d}s \\ &= 1 - \beta\sqrt{\pi cDt}\, M\left(\frac{y_3+2\beta cDt}{\sqrt{4cDt}}\right), \end{aligned} \tag{3.1.18}$$

where we introduce

$$M(z) := e^{z^2}\operatorname{erfc}(z). \tag{3.1.19}$$

Based on the asymptotic expansion of the complementary error function given as

$$\sqrt{\pi} z e^{z^2} \operatorname{erfc}(z) \sim 1 + \sum_{m=1}^{\infty} (-1)^m \frac{(2m-1)!!}{(2z^2)^m}, \quad z \gg 1,$$

we have $M(z) \sim 1/(z\sqrt{\pi})$ for large z. Thus we have $0 < \mathcal{K}_3(y_3;z) < 1$ and $\mathcal{K}_3(y_3;z) \to 1$ as $z \to 0+$, which implies that $\mathcal{K}_3(y_3;\cdot)$ can be considered as a positive continuous function on $[0,+\infty)$ with $\mathcal{K}_3(y_3;0) = 1$ for any fixed $y_3 > 0$. Therefore we have

$$W[q](s,t-s) = \int_{\mathbb{R}_+} Q(y_3,t-s,s) \frac{1}{\sqrt{4\pi cD(t-s)}} \frac{1}{\sqrt{4\pi cDs}} e^{-y_3^2\left(\frac{1}{4cD(t-s)}+\frac{1}{4cDs}\right)}\,\mathrm{d}y_3$$

with a compactly supported smooth function

$$Q(\cdot,t-s,s) := 4q(\cdot)\mathcal{K}_3(\cdot;s)\mathcal{K}_3(\cdot;t-s) > 0.$$

Further by the variable transform, we have

$$W[q](s,t-s) = \frac{1}{\sqrt{4cDt}} \int_{\mathbb{R}_+} Q(2\sqrt{cD}z(s(1-s/t))^{1/2}, t-s, s) e^{-z^2}\,\mathrm{d}z,$$

which implies

$$W[q](t,0) = \frac{1}{\sqrt{4cDt}} \int_{\mathbb{R}_+} Q(2\sqrt{cD}z(s(1-s/t))^{1/2}, t-s, s)e^{-z^2}\,\mathrm{d}z\,|_{s=t} > 0. \tag{3.1.20}$$

$W[q](0,t)$ has the same expression due to $W[q](s,t-s) = W[q](t-s,s)$. Therefore, for known $q(y_3)$, the integral equations (3.1.16) and (3.1.17) are Volterra integral equations of the second kind for $p(\tilde{x})$ and $p(\tilde{x}_s)$, respectively, which are uniquely solvable.

The proof is complete. ☐

3.2 Long-time Behavior of Emission Light

The emission light u_m has information on the fluorosence target. Let us investigate the long-time behavior of u_m. We will see below that the fluorescence lifetime τ can be estimated by the long-time behavior of u_m.

For simplicity we consider a point target

$$\mu_f(x) = \delta(x - x_0), \quad x_0 := (x_1^0, x_2^0, x_3^0) \in \Omega. \tag{3.2.1}$$

That is, Ω_0 is a point x_0. According to (2.2.9), the emission light $u_m(x_d, t; x_s)$ with $x_d, x_s \in \partial\Omega$ can be calculated as

$$u_m(x_d, t; x_s) = \frac{\gamma}{16\pi^3 D^2 c} \int_0^t \frac{1}{\tau} e^{-\frac{t-s}{\tau}} e^{-c\mu_a s} \int_0^s \xi(s,s') e^{\zeta(s,s')}\,\mathrm{d}s'\mathrm{d}s. \tag{3.2.2}$$

Here we introduced

$$\begin{aligned}\xi(s,s') &= \frac{1}{[(s-s')s']^{3/2}} \\ &\times \left[1 - \beta\sqrt{\pi Dc(s-s')}M\left(\frac{x_3^0 + 2\beta Dc(s-s')}{\sqrt{4Dc(s-s')}}\right)\right] \\ &\times \left[1 - \beta\sqrt{\pi Dcs'}M\left(\frac{x_3^0 + 2\beta Dcs'}{\sqrt{4Dcs'}}\right)\right],\end{aligned} \tag{3.2.3}$$

and

$$\zeta(s,s') = -\frac{|x_d - x_0|^2}{4Dc(s-s')} - \frac{|x_s - x_0|^2}{4Dcs'}, \tag{3.2.4}$$

where $M(z)$ is defined by (3.1.19). On the other hand, we note

$$\min_{t\in(0,T)} \frac{x_3^0 + 2\beta Dct}{\sqrt{4Dct}} = \sqrt{2\beta x_3^0}. \tag{3.2.5}$$

In the sequel, let us suppose

$$x_3^0 \gg \frac{1}{2\beta}. \tag{3.2.6}$$

Then, using the method of steepest descent, we obtain

$$\begin{aligned} u_m(x_d,t;x_s) \approx{}& \frac{\gamma(x_3^0)^2}{8\pi^{5/2}D^{3/2}\sqrt{c}} \frac{(|x_s-x_0|+|x_d-x_0|)^3}{|x_s-x_0||x_d-x_0|} \\ &\times \int_0^t h_\tau(t-s)\frac{e^{-c\mu_a s}}{s^{3/2}} \exp\left(-\frac{(|x_s-x_0|+|x_d-x_0|)^2}{4Dcs}\right) \\ &\times \frac{1}{C_0x_3^0+2\beta Dc|x_s-x_0|s}\,\frac{1}{C_0x_3^0+2\beta Dc|x_d-x_0|s}\,\mathrm{d}s, \end{aligned} \tag{3.2.7}$$

where $C_0 = |x_s - x_0| + |x_d - x_0|$.

By considering large t, we assume the following relations.

$$t \gg \tau, \quad \tau \gg \frac{x_3^0}{2\beta Dc}. \tag{3.2.8}$$

Since we are interested the long-time behavior of $u_m(x_d,t;x_s)$, we take the Laplace transform for t and take only small values of the Laplace variable into account. Then for large t, we have

$$u_m(x_d,t;x_s) \propto \exp\left[-\frac{1}{\tau}\left(t-\frac{|x_s-x_0|+|x_d-x_0|}{2c\sqrt{\mu_a D}}\right)\right]. \tag{3.2.9}$$

Therefore we obtain

$$\tau = \left(-\frac{\partial}{\partial t}\ln u_m(x_d,t;x_s)\right)^{-1}. \tag{3.2.10}$$

In Chapter 6, we will develope a reconstruction algorithm using pre-determined fluorescence lifetime, which is not always known a priori. Kumar et al. pointed out that the fluorescence lifetime can be estimated from the asymptotic behavior of the temporal profile of the emission light [60,61]. Here we showed that their formula also holds true in the presence of the boundary.

3.3 Chapter Summary

We established the identifiability of the fluorophore and revealed the physical difficulty of the 3-dimensional imaging model by the back scattering diffusive system. We point that although the FDOT based on the linearized DE model was a linear inverse problem, we can only establish the identifiability of the fluorophore by its absorption coefficient $\mu_f(x) := p(\tilde{x})q(x_3)$ with $\tilde{x} \in \partial\Omega$. We verified the uniqueness of $p(\tilde{x})$, under the assumptions that the vertical information of absorption $q(x_3)$ is known, and the lifetime of the fluorophore is $\tau = 0$. However, the general practical target $\mu_f(x)$ may not have the decomposition form $p(\tilde{x})q(x_3)$ and its lifetime are generally $\tau > 0$. Also, we need to develop the efficient reconstruction algorithms for $\mu_f(x)$ in finite dimensional space, which is one of our tasks in the following chapters.

Chapter 4

FDOT Using Cuboid Approximation

In this chapter, for general target with any $\tau > 0$, we will introduce the idea of *cuboid approximation* for our FDOT based on the linearized DE model, which develops a simple imaging model for $\mu_f(x)$ in finite dimensional space. The remainder of this chapter is organized as follows. We first simplify the linearized DE model and provide a fast solver for the forward problem by assuming a cuboid in section 4.1. In section 4.2, the numerical implementations using cuboid to approximate spherical target is shown to valuate the rationality of approximating unknown target by cuboid. The simulation and property of measured data are numerically tested in section 4.3 which is useful to find a good initial guess for iteration methods. Finally the concluding remark is denoted in section 4.4.

4.1 The Idea of Cuboid Approximation

We first recall our FDOT based on the linearized DE model, which is an effective and reasonable approximation of RTE model as we analyzed in Chapter 2. Let a fluorescence target be embedded in a biological tissue occupying the half space Ω with boundary $\partial\Omega$. We assume that the reduced scattering coefficient μ_s' and the absorption coefficient μ_a are constant everywhere in the medium and in the wavelength range of the excitation and fluorescence. Let $x_s = (x_{s1}, x_{s2}, 0) \in \partial\Omega$ denote the position where the excitation photons are injected by a pencil beam of the temporal profile $r(t)(t > 0)$ and hence generating the excitation light on the boundary. Then the propagation of excitation light $u_e(x, t; x_s)$ and emission (fluorescence) light $u_m(x, t; x_s)$ in scattering–absorbing medium can be described by coupled time-domain diffusion equations as follows [51, 57]

$$\begin{cases} \left(\frac{1}{c}\frac{\partial}{\partial t} - D\Delta + \mu_a\right) u_e = 0, & (x,t) \in \Omega \times (0,T), \\ u_e(x,0) = 0, & x \in \Omega, \\ \nu \cdot \nabla u_e + \beta u_e = \delta(x - x_s) r(t), & (x,t) \in \partial\Omega \times (0,T), \end{cases} \tag{4.1.1}$$

and

$$\begin{cases} \left(\frac{1}{c}\frac{\partial}{\partial t} - D\Delta + \mu_a\right) u_m = f(x,t;\tau), & (x,t) \in \Omega \times (0,T), \\ u_m(x,0) = 0, & x \in \Omega, \\ \nu \cdot \nabla u_m + \beta u_m = 0, & (x,t) \in \partial\Omega \times (0,T), \end{cases} \tag{4.1.2}$$

where $\nu = (0, 0, -1)$ is the unit outward normal direction, c is the speed of light in the medium, and $D := \frac{1}{3\mu_s'}$, β are some positive constants defined as before. The source term f for u_m on the right-hand side of (4.1.2) contains the excitation field and is specified by

$$f(x,t;\tau) = \frac{\gamma \mu_f(x)}{\tau} \int_0^t e^{-(t-s)/\tau} u_e(x, s; x_s) \, \mathrm{d}s, \tag{4.1.3}$$

where $\tau > 0$ is the fluorescence lifetime, γ is the quantum efficiency of the fluorescence, and μ_f is the absorption coefficient of fluorophore inside the target. It should be remarked here that we have assumed that $\mu_f \ll \mu_a$.

4.1.1 Analytical solution to real experiment

In the real experiment such as our ex vivo beef experiment in Chapter 7, any device for the measurements has some delay in responding to the coming signals. Suppose an excited light is detected at $x_d := (x_{d1}, x_{d2}, 0) \in \partial\Omega$, the detected excitation light U_e^{exp} is given through a *response function* $\widetilde{R}$ as

$$U_e^{\mathrm{exp}}(x_d, t; x_s) := \int_0^t \widetilde{R}(t-s) u_e(x_d, s; x_s)\,\mathrm{d}s, \tag{4.1.4}$$

where $x_d \in \partial\Omega$ denotes the position of a detector. Similarly, the observed emission light U_m^{exp} is given as

$$U_m^{\mathrm{exp}}(x_d, t; x_s) := \int_0^t \widetilde{R}(t-s) u_m(x_d, s; x_s)\,\mathrm{d}s. \tag{4.1.5}$$

Further, the excitation laser pulse is slightly temporal broadened in the real experiment. We take these non-ideal temporal broadening effects into account with an *instrumental response function* (IRF)

$$q(t) := \int_0^t \widetilde{R}(t-s) r(s)\,\mathrm{d}s, \tag{4.1.6}$$

which is experimentally determined.

Our fluorescence diffuse optical tomography (FDOT) is to identify the distribution of $\mu_f(x)$ in Ω as well as its interface from the boundary measured data, which is a *linear inverse source problem* formulated by the forward diffusion model together with the corresponding additional information.

Then, by changing the order of integrals and the general theory of partial differential equations, we immediately have the following expression of U_m^{exp} stated as a lemma.

Lemma 4.1. *Suppose $\Omega_0 \Subset \Omega$ be the support of $\mu_f(x)$, we have*

$$U_m^{\mathrm{exp}}(x_d, t; x_s) = \int_0^t \widetilde{q}(\xi) \widetilde{u}_m(x_d, t-\xi; x_s)\,\mathrm{d}\xi, \quad x_d, x_s \in \partial\Omega,\ t \in [0, T], \tag{4.1.7}$$

where $\widetilde{q}(\xi)$ is defined by

$$\widetilde{q}(\xi) = \int_0^\xi \frac{e^{-s/\tau}}{\tau} q(\xi - s)\,\mathrm{d}s \tag{4.1.8}$$

and $\widetilde{u}_m(x_d, t; x_s), x_d, x_s \in \partial\Omega, t \in [0, T]$ given by

$$\widetilde{u}_m(x_d, t; x_s) = \gamma D \int_0^t \int_{\Omega_0} \mu_f(y) K(x_d, y; t-s) K(y, x_s; s)\,\mathrm{d}y\mathrm{d}s \tag{4.1.9}$$

is the photon density of zero-lifetime emission light satisfying initial boundary value problem (3.1.6).

Proof. By solving the initial boundary value problem (4.1.2), we have

$$\begin{aligned} u_m(x_d, t; x_s) &= \int_0^t \int_\Omega K(x_d, y; t-s) f(y, s; \tau)\,\mathrm{d}y\mathrm{d}s \\ &= \gamma \int_0^t \int_0^s \frac{e^{-(s-t')/\tau}}{\tau} \int_{\Omega_0} \mu_f(y) K(x_d, y; t-s) u_e(y, t'; x_s)\,\mathrm{d}y\mathrm{d}t'\mathrm{d}s \end{aligned}$$

with $K(x,y;t)$ is the Green function satisfying (2.2.1) and

$$u_e(y,t';x_s) = D\int_0^{t'} r(t'')K(y,x_s;t'-t'')\,\mathrm{d}t''.$$

Thus u_m is written as

$$\begin{aligned} u_m(x_d,t;x_s) = \gamma D\int_0^t\int_0^s \frac{e^{-(s-t')/\tau}}{\tau}\int_0^{t'} r(t'')\int_{\Omega_0}\mu_f(y) \\ \times K(x_d,y;t-s)K(y,x_s;t'-t'')\,\mathrm{d}y\mathrm{d}t''\mathrm{d}t'\mathrm{d}s, \end{aligned}$$

Substituting above into (4.1.5), we have

$$\begin{aligned} U_m^{\exp}(x_d,t;x_s) = \gamma D\int_0^t R(\xi)\int_0^{t-\xi}\int_0^s \frac{e^{-(s-t')/\tau}}{\tau}\int_0^{t'} r(t'')\int_{\Omega_0}\mu_f(y) \\ \times K(x_d,y;t-\xi-s)K(y,x_s;t'-t'')\,\mathrm{d}y\mathrm{d}t''\mathrm{d}t'\mathrm{d}s\mathrm{d}\xi. \end{aligned}$$

By (3.1.7) and exchanging the integrals we have

$$\begin{aligned} U_m(x_d,t;x_s) &= \gamma D\int_0^t \widetilde{q}(\xi)\int_0^{t-\xi}\int_{\Omega_0}\mu_f(y)K(x_d,y;t-\xi-s)K(y,x_s;s)\,\mathrm{d}y\mathrm{d}s\mathrm{d}\xi \\ &= \int_0^t \widetilde{q}(\xi)\widetilde{u}_m(x_d,t-\xi;x_s)\,\mathrm{d}\xi, \end{aligned}$$

where $\widetilde{q}(\xi)$ is defined by (4.1.8). This completes the proof. □

4.1.2 Fast solver by assuming cuboid

Although the fluorescence target which we try to recover may have different shapes, in this paper we focus on simultaneously recovering the position and approximate size of the fluorescence target in the tissue by assuming that it has a cuboidal shape. In other words, we assume that the support of $\mu_f(x)$ is a *cuboid*, which is parallel to horizontal plane and vertical plane. Since the absorption coefficient μ_f of the fluorophore has a nonzero value only inside the target, we have

$$\mu_f(x) = \begin{cases} P, & x\in \text{cuboid}, \\ 0, & x\notin \text{cuboid}, \end{cases} \tag{4.1.10}$$

where P is a positive constant and

$$\text{cuboid} := \{x\in\Omega;\ x_1\in(a_1,b_1),\ x_2\in(a_2,b_2),\ x_3\in(a_3,b_3)\} \tag{4.1.11}$$

with $b_3 > a_3 > 0$. Thus, to recover the distribution of $\mu_f(x)$ in Ω as well as its interface, we only need to determine seven unknowns $(a_1,b_1,a_2,b_2,a_3,b_3,P)$ in practical configurations, which becomes a *nonlinear inverse problem*. In the future work, we will consider the approximate recovery of fluorescence target using the cuboid with some rotation, which implies to identify nine unknowns including the angles of cuboid with horizontal and vertical planes. In the sequel, we use the following identification

$$\mu_f(x) \Leftrightarrow \mathbf{a} := (a_1,b_1,a_2,b_2,a_3,b_3,P)\in\mathbb{R}^4\times\mathbb{R}^3_+. \tag{4.1.12}$$

Then we can provide a *fast solver* for the forward problem by transforming $\widetilde{u}_m$ given by (4.1.9) into following easy computation scheme.

Theorem 4.1. *Suppose that the support of* $\mu_f(x)$ *is a cuboid, we have*

$$\begin{aligned}\widetilde{u}_m(x_d,t;x_s) = PC(x_{d1},x_{s1},x_{d2},x_{s2},t)&\int_0^t \frac{1}{\sqrt{s(t-s)}}\\ &\times \widetilde{u}_1(x_{d1},x_{s1},t,s;a_1,b_1)\\ &\times \widetilde{u}_2(x_{d2},x_{s2},t,s;a_2,b_2)\widetilde{u}_3(t,s;a_3,b_3)\,\mathrm{d}s,\end{aligned}\tag{4.1.13}$$

where $C(x_{d1},x_{s1},x_{d2},x_{s2},t) := \frac{\gamma}{4^3\pi^2 Dt}e^{-\frac{(x_{d1}-x_{s1})^2+(x_{d2}-x_{s2})^2}{4cDt}}e^{-c\mu_a t}$, *and*

$$\begin{aligned}\widetilde{u}_i(x_{di},x_{si},t,s;a_i,b_i) = \operatorname{erf}&\left(\sqrt{\frac{t}{4cD(t-s)s}}\left(b_i-\frac{sx_{di}+(t-s)x_{si}}{t}\right)\right)\\ &-\operatorname{erf}\left(\sqrt{\frac{t}{4cD(t-s)s}}\left(a_i-\frac{sx_{di}+(t-s)x_{si}}{t}\right)\right), \quad t>s,\end{aligned}$$

for $i=1,2$ *and*

$$\widetilde{u}_3(t,s;a_3,b_3) := \int_{a_3}^{b_3} K_3(0,y_3;t-s)K_3(y_3,0;s)\,\mathrm{d}y_3, \ \ t>s$$

with $K_3(x,y;t)$ *defined by* (2.2.5) *and error function* $\operatorname{erf}(z) := \frac{2}{\sqrt{\pi}}\int_0^z e^{-\zeta^2}\,\mathrm{d}\zeta$.

Proof. We note that

$$\begin{aligned}\int_a^b e^{-\frac{(y-\alpha)^2}{p}}e^{-\frac{(y-\beta)^2}{q}}\,\mathrm{d}y &= \sqrt{\frac{pq}{p+q}}e^{-\frac{(\alpha-\beta)^2}{p+q}}\int_{\sqrt{\frac{p+q}{pq}}\left(a-\frac{q\alpha+p\beta}{p+q}\right)}^{\sqrt{\frac{p+q}{pq}}\left(b-\frac{q\alpha+p\beta}{p+q}\right)} e^{-z^2}\,\mathrm{d}z\\ &= \frac{1}{2}\sqrt{\frac{\pi pq}{p+q}}\,e^{-\frac{(\alpha-\beta)^2}{p+q}} \times \left[\operatorname{erf}\left(\sqrt{\frac{p+q}{pq}}\left(b-\frac{q\alpha+p\beta}{p+q}\right)\right)\right.\\ &\left.-\operatorname{erf}\left(\sqrt{\frac{p+q}{pq}}\left(a-\frac{q\alpha+p\beta}{p+q}\right)\right)\right].\end{aligned}$$

Hence, by simple computation we have

$$\begin{aligned}&\int_{a_1}^{b_1}\int_{a_2}^{b_2} e^{-\frac{(x_{d1}-y_1)^2+(x_{d2}-y_2)^2}{4cD(t-s)}}e^{-\frac{(y_1-x_{s1})^2+(y_2-x_{s2})^2}{4cDs}}\,\mathrm{d}y_1\mathrm{d}y_2\\ =&\left(\int_{a_1}^{b_1} e^{-\frac{(x_{d1}-y_1)^2}{4cD(t-s)}}e^{-\frac{(y_1-x_{s1})^2}{4cDs}}\,\mathrm{d}y_1\right)\left(\int_{a_2}^{b_2} e^{-\frac{(x_{d2}-y_2)^2}{4cD(t-s)}}e^{-\frac{(y_2-x_{s2})^2}{4cDs}}\,\mathrm{d}y_2\right)\\ =&\frac{\pi cD(t-s)s}{t}e^{-\frac{(x_{d1}-x_{s1})^2+(x_{d2}-x_{s2})^2}{4cDt}}\\ &\times\left[\operatorname{erf}\left(\sqrt{\frac{t}{4cD(t-s)s}}\left(b_1-\frac{sx_{d1}+(t-s)x_{s1}}{t}\right)\right)\right.\\ &\left.-\operatorname{erf}\left(\sqrt{\frac{t}{4cD(t-s)s}}\left(a_1-\frac{sx_{d1}+(t-s)x_{s1}}{t}\right)\right)\right]\\ &\times\left[\operatorname{erf}\left(\sqrt{\frac{t}{4cD(t-s)s}}\left(b_2-\frac{sx_{d2}+(t-s)x_{s2}}{t}\right)\right)\right.\\ &\left.-\operatorname{erf}\left(\sqrt{\frac{t}{4cD(t-s)s}}\left(a_2-\frac{sx_{d2}+(t-s)x_{s2}}{t}\right)\right)\right].\end{aligned}$$

Thus we obtain

$$\begin{aligned}
&\int_{\Omega_0} K(x_d, y; t-s)K(y, x_s; s)\,\mathrm{d}y \\
={}& \frac{c^2 e^{-c\mu_a t}}{(4\pi cD)^3(t-s)^{3/2}s^{3/2}} \left(\int_{a_1}^{b_1}\int_{a_2}^{b_2} e^{-\frac{(x_{d1}-y_1)^2+(x_{d2}-y_2)^2}{4cD(t-s)}} e^{-\frac{(y_1-x_{s1})^2+(y_2-x_{s2})^2}{4cDs}}\,\mathrm{d}y_1\mathrm{d}y_2\right) \\
&\times \int_{a_3}^{b_3} K_3(0, y_3; t-s)K_3(y_3, 0; s)\,\mathrm{d}y_3 \\
={}& \frac{e^{-c\mu_a t}}{4^3\pi^2 D^2 t\sqrt{(t-s)s}} e^{-\frac{(x_{d1}-x_{s1})^2+(x_{d2}-x_{s2})^2}{4cDt}} \\
&\times \widetilde{u}_1(x_{d1}, x_{s1}, t, s; a_1, b_1)\widetilde{u}_2(x_{d2}, x_{s2}, t, s; a_2, b_2)\widetilde{u}_3(t, s; a_3, b_3),
\end{aligned}$$

where $\widetilde{u}_1(x_{d1}, x_{s1}, t, s; a_1, b_1), \widetilde{u}_2(x_{d2}, x_{s2}, t, s; a_2, b_2), \widetilde{u}_3(t, s; a_3, b_3)$ are defined as above. Then, by the expression (4.1.9) and (4.1.10) we have

$$\begin{aligned}
\widetilde{u}_m(x_d, t; x_s) ={}& \frac{\gamma P e^{-c\mu_a t}}{4^3\pi^2 Dt} e^{-\frac{(x_{d1}-x_{s1})^2+(x_{d2}-x_{s2})^2}{4cDt}} \\
&\times \int_0^t \frac{1}{\sqrt{(t-s)s}} \widetilde{u}_1(x_{d1}, x_{s1}, t, s; a_1, b_1) \\
&\times \widetilde{u}_2(x_{d2}, x_{s2}, t, s; a_2, b_2)\widetilde{u}_3(t, s; a_3, b_3)\,\mathrm{d}s.
\end{aligned}$$

By the definition of $C(x_{d1}, x_{s1}, x_{d2}, x_{s2}, t)$, we end the proof. ☐

Remark 4.1. *Although the form of* (4.1.13) *looks not of convolution type, it is actually the same as* (4.1.9) *which is of convolution type.*

Suppose that the support of $\mu_f(x)$ is a cuboid, we can analyze the singularity of zero-lifetime emission (4.1.13) when $s \to 0_+$ and $s \to t_-$ for any fixed $t > 0$. Noticing the error function erf is odd function and $\mathrm{erf}(+\infty) = 1$, we have the following results.

Theorem 4.2. *(1) For every fixed $t > 0$, $a_i, b_i \in \mathbb{R}$ and $a_i < b_i$ $(i = 1, 2)$, we have*

$$\lim_{s\to 0_+} \widetilde{u}_i(x_{di}, x_{si}, t, s; a_i, b_i) = \begin{cases} 2, & for\ x_{si} \in (a_i, b_i), x_{di} \in \mathbb{R}, \\ 1, & for\ x_{si} = a_i, x_{di} \in \mathbb{R}\ \ or\ \ x_{si} = b_i, x_i \in \mathbb{R}, \\ 0, & else; \end{cases} \tag{4.1.14}$$

$$\lim_{s\to t_-} \widetilde{u}_i(x_{di}, x_{si}, t, s; a_i, b_i) = \begin{cases} 2, & for\ x_{di} \in (a_i, b_i), x_{si} \in \mathbb{R}, \\ 1, & for\ x_{di} = a_i, x_{si} \in \mathbb{R}\ or\ x_{di} = b_i, x_{si} \in \mathbb{R}, \\ 0, & else. \end{cases} \tag{4.1.15}$$

(2) For every fixed $t > 0$ and $0 < a_3 < b_3$, we have

$$\lim_{s\to 0_+} \frac{1}{\sqrt{s(t-s)}} \widetilde{u}_3(t, s; a_3, b_3) = \lim_{s\to t_-} \frac{1}{\sqrt{s(t-s)}} \widetilde{u}_3(t, s; a_3, b_3) = 0, \tag{4.1.16}$$

which is not dependent on the positions of x_d and x_s.

Proof. Based on the property of error function, it is easy to prove (4.1.14) and (4.1.15). Now we prove (4.1.16).

By the expression of $K_3(x,y;t)$ we have

$$\begin{aligned}\frac{1}{\sqrt{s(t-s)}}\widetilde{u}_3(t,s;a_3,b_3) &= \frac{1}{\sqrt{s(t-s)}}\int_{a_3}^{b_3} K_3(0,y_3;t-s)K_3(y_3,0;s)\,\mathrm{d}y_3\\ &= \frac{4}{\sqrt{s(t-s)}}\int_{a_3}^{b_3} e^{-\frac{y_3^2}{4Dc(t-s)}-\frac{y_3^2}{4Dcs}}\\ &\times\left[1-\beta\sqrt{\pi Dc(t-s)}M\left(\frac{y_3+2\beta Dc(t-s)}{\sqrt{4Dc(t-s)}}\right)\right]\\ &\times\left[1-\beta\sqrt{\pi Dcs}M\left(\frac{y_3+2\beta Dcs}{\sqrt{4Dcs}}\right)\right]\,\mathrm{d}y_3,\end{aligned}$$

where the function $M(z)$ is defined by (3.1.19). By $M(z)\sim 1/(z\sqrt{\pi})$ for $z\gg 1$, we obtain the estimate for $t>0$ that

$$\begin{aligned}\frac{1}{\sqrt{s(t-s)}}\widetilde{u}_3(t,s;a_3,b_3) &\leq \frac{4}{\sqrt{s(t-s)}}\int_{a_3}^{b_3} e^{-\left(\frac{y_3^2}{4Dc(t-s)}+\frac{y_3^2}{4Dcs}\right)}\,\mathrm{d}y_3\\ &= 8\sqrt{\frac{Dc}{t}}\int_{\sqrt{\frac{t}{t-s}}\frac{a_3}{\sqrt{4Dcs}}}^{\sqrt{\frac{t}{t-s}}\frac{b_3}{\sqrt{4Dcs}}} e^{-z^2}\,\mathrm{d}z =: \mathcal{U}_3(t,s;a_3,b_3),\end{aligned} \tag{4.1.17}$$

where we substitute $z=\sqrt{\frac{t}{t-s}}\frac{y_3}{\sqrt{4Dcs}}$ satisfying

$$\frac{{y_3}^2}{4Dc(t-s)}+\frac{{y_3}^2}{4Dcs}=z^2. \tag{4.1.18}$$

Apparently, $\lim_{s\to 0_+}\mathcal{U}_3(t,s;a_3,b_3)=\lim_{s\to t_-}\mathcal{U}_3(t,s;a_3,b_3)=0$, which implies (4.1.16). ☐

Theorem 4.2 ensures the effectiveness of solving (4.1.13) by numerical methods such as trapezoidal formula and compound trapezoidal formula. Now we give one numerical example to verify the results in Theorem 4.2. Without loss of generality, we fix time $t=100$ ps, $a_1=3$ mm, $b_1=6$ mm and take physical parameters as (2.3.3) to numerically check the behavior of $\widetilde{u}_1$ when $s\to 0_+$ and $s\to t_-$. The values of $\lim_{s\to 0_+}\widetilde{u}_1(x_{d1},x_{s1},t,s;a_1,b_1)$ with fixed $x_{d1}=1$ and $x_{s1}\in[0,10]$ is plotted in Figure 4.1 (a), and the values of $\lim_{s\to t_-}\widetilde{u}_1(x_{d1},x_{s1},t,s;a_1,b_1)$ with fixed $x_{s1}=1$ and $x_{d1}\in[0,10]$ is plotted in Figure 4.1 (b), respectively. The numerical results are consistent to Theorem 4.2.

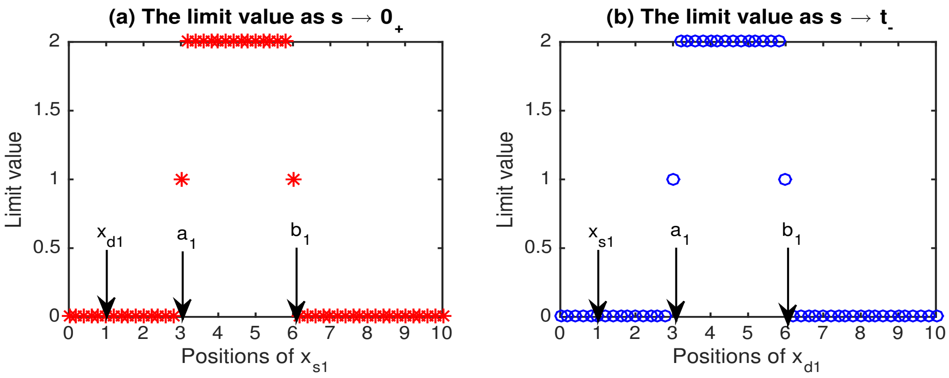

FIGURE 4.1: (a) The values of $\lim_{s\to 0_+}\widetilde{u}_1(x_{d1},x_{s1},t,s;a_1,b_1)$ with fixed $x_{d1}=1$ and $x_{s1}\in[0,10]$. (b) The values of $\lim_{s\to t_-}\widetilde{u}_1(x_{d1},x_{s1},t,s;a_1,b_1)$ with fixed $x_{s1}=1$ and $x_{d1}\in[0,10]$.

4.2 Testing the Rationality of Cuboid Approximation

How to save time of computation is very important for solving inverse problems in practice. To fulfill this request, on one hand, a fast solver for the forward problem is highly desirable for inversion schemes using iterative methods such as the least square method, Levenberg-Marquadt method and trust region method. On the other hand, the interpretation of the measured data by small number of effective parameters could be useful. Hence we aim to describe the unknown target by finite parameters such that a small number of sources and detectors are enough to have a good performance in our inversion scheme based on Levenberg-Marquadt method.

Next we will show numerically that the modeling of the target by cuboid is a reasonable approximation. In another word, we will show that the measured emission light due to the existence of an unknown target can be approximated well by assuming it as a cuboid. To do that, we will compare the *temporal point spread functions* (TPSFs) associated with different shape of targets by that associated with cuboidal target.

To be precise we will give one example. For that, if not specified, we always take the physical parameters as (2.3.3). Hereafter the unit of length is mm, and we will set $\gamma = 1$. The quantum efficiency γ of the real fluorophore molecule is usually less than 1. However, this factor only affects the scaling of the absorption coefficient μ_f and thus this factor is only needed to calculate the absolute value of μ_f as a proportional constant. The discussion of the recovery will not change even if assuming $\gamma = 1$ except requirement of the absolute value of μ_f.

Example 4.1. (spherical target) *Suppose a spherical target with 6 mm in diameter shown in Figure 4.2 is located at* $(0, 0, 11)$. *We assume the absorption coefficient of the target by fluorophore is* $\mu_f = P = 0.0017\ \mathrm{mm}^{-1}$ *inside the sphere.*

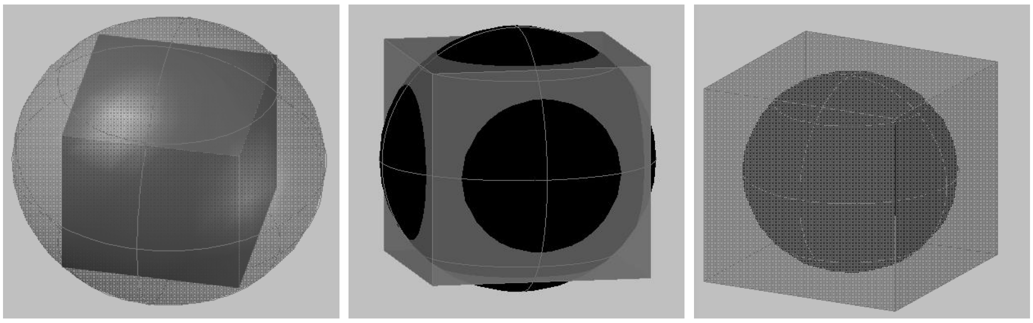
(a) Cube1 (b) Cube2 (c) Cube3

FIGURE 4.2: The spherical target and three cubic targets approximated to the spherical target; Cube1 is the inscribed cubic target, Cube2 is the cubic target which has same volume and Cube3 is the circumscribed cubic target.

In this example we compare the zero-lifetime emission light between spherical target and three different cubic targets shown in Figure 4.2, (a), (b), (c) respectively, all of which have the same absorption P. In particular, Cube2 denoted by

$$\mathrm{Cube2} := \{x \in \Omega;\ x_1 \in (-2.42, 2.42),\ x_2 \in (-2.42, 2.42),\ x_3 \in (8.58, 13.42)\} \qquad (4.2.1)$$

has the same center and volume as that of the spherical target. For the cubic targets, the photon density of emission light $\widetilde{u}_m^{\mathrm{cube}}(x_d, t; x_s)$ is computed by (4.1.13). For spherical fluorophore target, its photon density of emission light is calculated by

$$\begin{aligned}\widetilde{u}_m^{\text{sphere}}(x_d, t; x_s) = \gamma DP \int_0^t \mathrm{d}s \int_0^R r^2\,\mathrm{d}r \int_0^\pi \sin\varphi\,\mathrm{d}\varphi \\ \times \int_0^{2\pi} K(x_d, y; t-s) K(y, x_s; s)\,\mathrm{d}\theta,\end{aligned} \tag{4.2.2}$$

where $y = x^* + r(\sin\varphi\cos\theta, \sin\varphi\sin\theta, \cos\varphi)$, $x^* = (x_1^*, x_2^*, x_3^*) = (0, 0, 11)$ is the center of sphere and $r = 6$ mm is its diameter.

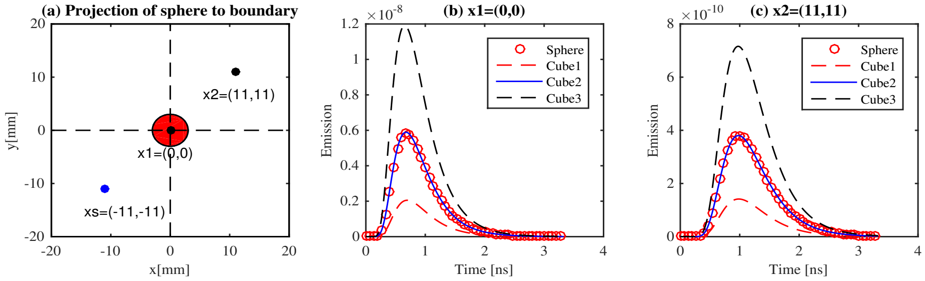

FIGURE 4.3: TPSFs (i.e. temporal profile of the emission) corresponding to the spherical target indicated by circles and three approximate cube targets indicated by lines. Two figures are corresponding to the different detection points at (0,0,0) and (19,-11, 0).

As shown in Figure 4.3 (a), we fix the point source $x_s = (-11, -11) \in \partial\Omega$ and consider two detectors located at $x_1 = (0, 0), x_2 = (11, 11) \in \partial\Omega$ for $t \in (0, T)$ with $T = 3.3$ ns. TPSFs corresponding to the emission light $\widetilde{u}_m^{\text{sphere}}(x_d, t; x_s)$ and $\widetilde{u}_m^{\text{cube}}(x_d, t; x_s)$ at two detectors are shown in Figure 4.3 (b), (c), respectively. It can be observed that the curves depend on the volumes of targets, and a good agreement indicates that the spherical target can be approximated well by the cubic target having the same center and volume as that of spherical target (Cube2). On the other hand, by applying the typical function (named integral3) implemented on Matlab to compute (4.2.2) could take several hours of computation. However, we could easily compute (4.1.13), for which less than one minute of computation was enough.

We further check the cuboid approximation from the view of inverse problem. We place four sources $S_i, i = 1, \cdots, 4$ and twelve detectors $D_j, j = 1, \cdots, 12$ as follows on the boundary (see Figure 4.4 (a)) to obtain the measurements

$$S_3 = (-11, 11), \quad S_4 = (11, 11),$$

$$S_1 = (-11, -11), \quad S_2 = (11, -11),$$

and

$$D_7 = (-19, 18), \quad D_9 = (-3, 18), \quad D_{10} = (6, 18), \quad D_{12} = (16, 18),$$

$$D_8 = (-11, 4), \quad D_{11} = (11, 4),$$

$$D_2 = (-11, -4), \quad D_5 = (11, -4),$$

$$D_1 = (-19, -18), \quad D_3 = (-3, -18), \quad D_4 = (6, -18), \quad D_6 = (16, -18).$$

Here we obtained the measured data with respect to a spherical target by the Monte Carlo simulation as we described in section 2.3. The emission at each detector corresponding to excitation S_1 are shown in Figure 4.4 (b), (c) respectively.

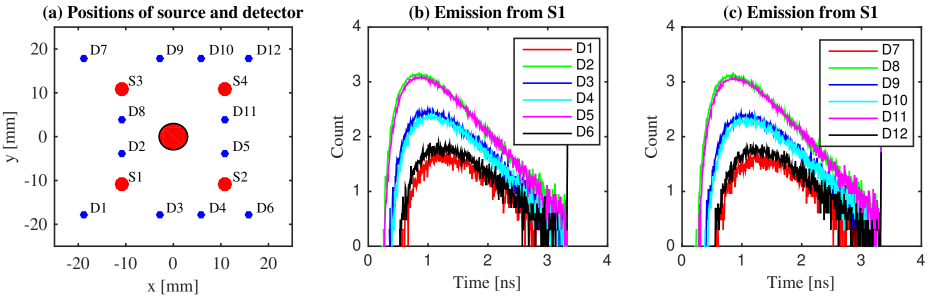

FIGURE 4.4: (a) The positions of four sources (small red circles) and twelve detectors (small blue points). The big red circle is the projection of spherical target to the boundary. (b), (c) are the TPSFs (the logarithm value) to different detectors corresponding to source S_1.

Let (X_1, X_2, X_3) denote the center of cube and L denote its side length. Denote by Q the absorption coefficient of recovered cube. We want to find an approximate cube

$$\mathbf{a}^{\text{cube}} := (X_1, X_2, X_3, L, Q) \tag{4.2.3}$$

of the spherical target by fitting the measured data. To identify unknowns $\mathbf{a}^{\text{cube}}$, we will use time-resolved measurements in time domain $[0, T]$ with $T = 3.3$ ns. For each source detector pair, we denote t_{peak} as the peak time at which the photon density of emission light is biggest. Then, for each source-detector pair we select the peak time and choose 10 time points $[t_{\text{peak}} - 5\Delta t, t_{\text{peak}} + 4\Delta t]$ with time step $\Delta t = 6.67$ ps. Setting the initial guess $\mathbf{a}_0 = (2, 2, 4, 2, 0.1)$, the recovered cube by Levenberg-Marquadt method is

$$\mathbf{a}^{\text{cube}}_{\text{rec}} = (-0.0003, -0.0047, 11.0418, 4.6759, 0.0020), \tag{4.2.4}$$

which is almost same as Cube2 given by (4.2.1).

Summarizing the results obtained in the above example, we have observed that TPSF for unknown target with spherical shape can be approximated well by corresponding one for cuboidal target having the same center and volume as that of the unknown target. The recovered cube (4.2.4) further confirms this argument. In other words, the interpretation of measured data using cuboidal target was reasonable and made the computation very fast.

4.3 Simulation and Property of Measured Data

Generally speaking, the measured data itself contain the information of the unknown target. How to analyze the relations between the measurement and unknown target is important to obtain some prior information of the target, which is very useful in establishing our inversion strategy. To do this, we study the property of measured data to obtain the prior estimation of unknown target. Let $\mathbf{a} = (a_1, b_1, a_2, b_2, a_3, b_3, P) = (-1, 1, -3, 3, 10, 12, 0.01)$ be a cuboidal target, and let the other physical parameters be the same as (2.3.3). That is

$$\mu_f(x) = \begin{cases} 0.01, & x \in \text{cuboid} := \{x \in \Omega;\ x_1 \in (-1,1),\ x_2 \in (-3,3),\ x_3 \in (10,12)\}, \\ 0, & x \notin \text{cuboid}. \end{cases}$$

We define the intensity of emission light corresponding to source-detector (S-D) pair as

$$\mathbf{I} := \int_0^T \widetilde{u}_m(\mathbf{a})(x_d, t; x_s)\, \mathrm{d}t. \tag{4.3.1}$$

Let (x_1, x_2) be the the middle position of a S-D pair. As shown in Figure 4.5, (a), we scan the S-D pair on $\partial\Omega$ along the direction $x_2 = 0$ without any rotation. Then the emission intensities with $T = 3.3$ ns and different positions of S-D pair are plotted in Figure 4.5, (b).

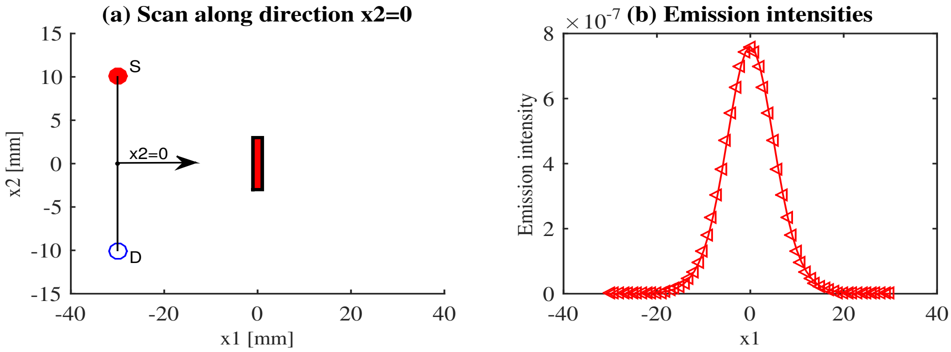

FIGURE 4.5: (a) Scan the S-D pair on the boundary $\partial\Omega$; The red rectangular shape shows the fluorescence target. (b) The emission intensities given by (4.3.1) with different position $x1$.

We keep the same size of cuboidal target as above and denote its center by $(0, 0, h)$. The TPSFs (the logarithm value) at $x_1 = x_2 = 0$ with respect to different h are plotted in Figure 4.6, (a). For fixed scan direction $x_2 = 0$, three indexes such as peak time, peak intensity and intensity of emission light with different S-D pairs and target center h are plotted in Figure 4.6, (b), (c), (d), respectively.

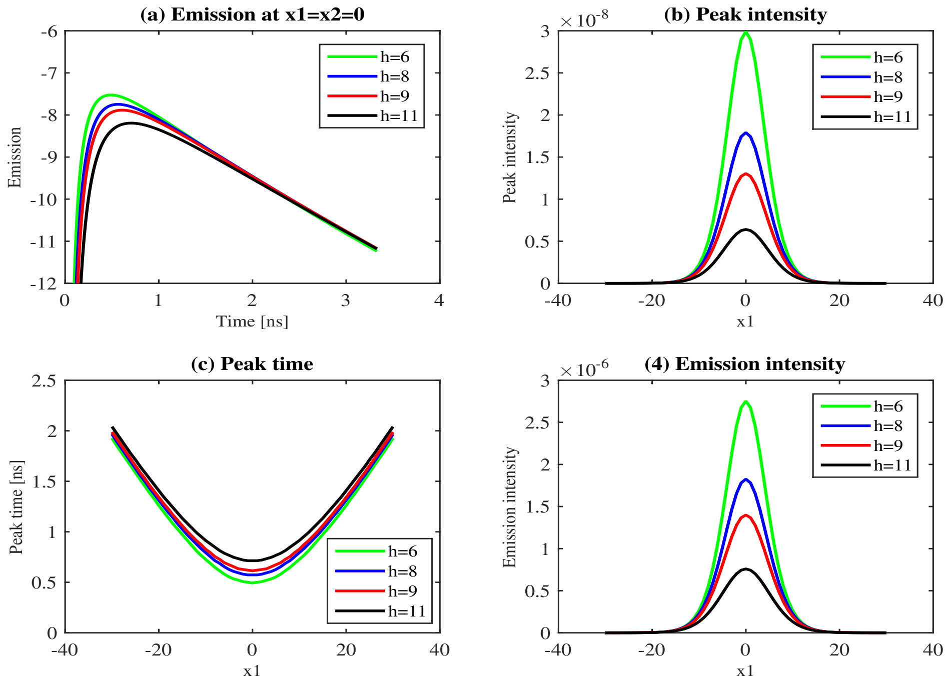

FIGURE 4.6: TPSFs and three indexes of emission light with different S-D pairs.

In both Figure 4.5 and Figure 4.6, the middle positions of the source and the detector with respect to different S-D pairs are $(x_1, 0)$ due to the fixed scan direction $x_2 = 0$.

Now we change the scan direction and scan the S-D pair on the boundary without any rotation. We plot the emission intensities given by different positions of the S-D pair for the target with $h = 11$ in Figure 4.7.

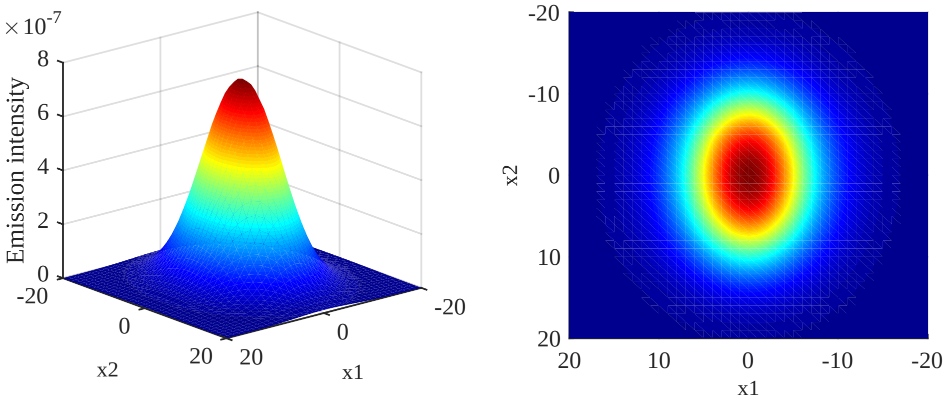

FIGURE 4.7: The distribution of emission intensity with different S-D pairs.

From Figure 4.5 and Figure 4.7, it can be seen that the intensities of emission light with S-D pairs near by the target are stronger than the others. We can see the same phenomenon for other indexes of emission light such as the peak time and the peak intensity from Figure 4.6. Therefore, by comparing for example the emission intensities I with different S-D pairs, we can obtain prior information of the projection of target to $\partial\Omega$, which is useful to choose a good initial guess for iteration methods.

4.4 Chapter Summary

We considered the cuboid approximation for our FDOT based on the linearized DE model. By solving the initial boundary value problem, the explicit analytical expression is possible for real experimental case, which is further transformed into an easy computation scheme having an integral form. We further analyzed the weak singularity of the integrand function with a numerical test, revealing that our proposed easy computation scheme is reliable to apply numerical integration for example trapezoidal formula. By comparing the temporal point spread functions (TPSFs) associated with spherical shape of target by that associated with cuboidal target, we showed numerically that the modeling of the target by cuboid is a reasonable approximation. The measured emission light due to the existence of an unknown target could be approximated well by assuming it as cuboid. Nevertheless, we point that it is hard to compute the TPSFs with irregular shape of target. Therefore, the remained problem is to verify the effectiveness of approximating the target with irregular shape by some associated cuboid. We also tested the properties of measured data, which gives us some ideas to choose a good initial guess in our inversion iteration method. Summarizing the results in this chapter, we observed that our cuboid approximation was reasonable and made the computation very fast. This provides a preliminary basis for our further research on FDOT using cuboid approximation in the following chapters.

Chapter 5

Local Analysis for FDOT Using Cuboid Approximation

In this chapter, we consider the local analysis for our FDOT inverse problem using cuboid approximation. For giving some mathematical analysis and discussion on our FDOT measurement and inversion, we need to describe the measurement using some mathematical notations. Since the detected experimental emission light U_m with any fixed $\tau > 0$ is the convolution of function $\widetilde{q}$ defined by (4.1.8) with the zero-lifetime emission light $\widetilde{u}_m$, it is enough to do that for $\widetilde{u}_m$ for simplicity. We start that by introducing the following convention.

Let $\{\omega_i := (x_s^i, x_d^i) \in \partial\Omega \times \partial\Omega, i = 1, 2, \cdots, N\}$ be the finite set of source-detector (S-D) pairs and let $\mathcal{T} \subset (0, \infty)$ be a time interval in which we have measurement times. Then, representing μ_f by vector $\mathbf{a}$ as in (4.1.10), (4.1.12), we can denote by $\widetilde{u}_m(\mathbf{a})(t_*, \omega_i)$ the unique solution of the forward diffusion problem corresponding to any given input $\mathbf{a}$ in a vector subspace $\mathcal{A} \subset \mathbb{R}^d$ with $\omega_i \in \partial\Omega \times \partial\Omega$ and $t_* \in \mathcal{T}$. Unless otherwise specified, we will always take $d = 7$ which is equal to the number of component of $\mathbf{a}$ of (4.1.12). Here d is different from the d for x_d^i and note that we have assumed $\mathcal{A}$ where the unknown $\mathbf{a}$ belongs does not change even when S-D pairs and measurement times change. Taking the measured data at K different times $\{t_1, \cdots, t_K\}$ denoted by $\hat{t} \in \mathcal{T}^K$, the inverse problem which we considered consists of determining an unknown vector $\mathbf{a}$ from a time-resolved data with N S-D pairs given as the following set of measurement data

$$H := (\vec{h}_1, \cdots, \vec{h}_N) = (\widetilde{u}_m(\mathbf{a})(\hat{t}, \omega_1), \cdots, \widetilde{u}_m(\mathbf{a})(\hat{t}, \omega_N)) \tag{5.0.1}$$

in an $N \times K$ dimensional real vector space $\mathcal{H}^{NK}$. The process of obtaining the finite set of measurement data (5.0.1) can be described as

$$\mathcal{F}_i := F(\hat{t}, \omega_i) : \mathcal{A} \to \mathcal{H}^K, \quad F(\hat{t}, \omega_i)(\mathbf{a}) := \widetilde{u}_m(\mathbf{a})(\hat{t}, \omega_i) = \vec{h}_i, \ i = 1, \cdots, N \tag{5.0.2}$$

with $\hat{t} \in \mathcal{T}^K$. For convenience, we rewrite (5.0.2) as a single equation

$$\mathcal{F} := F(\hat{t}, \hat{\omega}) : \mathcal{A} \to \mathcal{H}^{NK}, \quad F(\hat{t}, \hat{\omega})(\mathbf{a}) = H \text{ with } \hat{\omega} := (\omega_1, \cdots, \omega_N), \tag{5.0.3}$$

which is a nonlinear mapping. Further by Lemma 4.1, it is easy to see that $\mathcal{F}(\mathbf{a}) = F(\hat{t}, \hat{\omega})(\mathbf{a})$ is analytic with respect to $\hat{t}$, $\hat{\omega}$, $\mathbf{a}$.

In the forthcoming arguments, unless otherwise stated, $B_r(\mathbf{a}_0)$ stands for an open ball centered at $\mathbf{a}_0$ with radius $r > 0$ such that $\mathcal{B} := B_r(\mathbf{a}_0) \subset \mathcal{A}$, where $\mathbf{a}_0$ will be used as an initial guess of the iteration method.

5.1 The Determinant Condition

We first give the *determinant condition*. For given one time point $t_* \in \mathcal{T}$ and d S-D pairs $\hat{\omega}_* := (\omega_1, \cdots, \omega_d)$, let

$$\widetilde{F}(t_*, \hat{\omega}_*)(\mathbf{a}) := \det\left(\nabla M(t_*, \hat{\omega}_*)(\mathbf{a})\right) \tag{5.1.1}$$

with the column vector

$$M(t_*, \hat{\omega}_*)(\mathbf{a}) := (\widetilde{u}_m(\mathbf{a})(t_*, \omega_1), \cdots, \widetilde{u}_m(\mathbf{a})(t_*, \omega_d)) =: H^*, \tag{5.1.2}$$

where ∇ is the gradient with respect to $\mathbf{a}$. Then the determinant condition is given as

$$\widetilde{F}(t_*, \hat{\omega}_*)(\mathbf{a}) \neq 0 \quad \text{in } \mathcal{A}', \tag{5.1.3}$$

where $\mathcal{A}'$ is a subdomain of $\mathcal{A}$. We will see later in subsection 5.2 that we can recover $\mathbf{a}$ by knowing H^* if the determinant condition is satisfied. Hence it is very important to assure that the determinant condition can be satisfied for some time points and S-D pairs.

We further consider multiple time points for S-D pairs defined as follows.

Definition 5.1. *Given a finite set of time points* $\{t_1, t_2, \cdots, t_K\} \in \mathcal{T}^K$, *we say that* $\{t_1, \cdots, t_K\} \times \{\omega_1, \cdots, \omega_d\}$ *is a set of parameters giving the measurements.*

We would like to have a set of parameters giving the measurements and a finite open covering of $\mathcal{A}'$ such that the determinant condition (5.1.3) is satisfied in each open set of this covering by taking some time point. The precise meaning of this statement is given by the following definition.

Definition 5.2. *Let* $\mathcal{A}' \subset \mathcal{A}$. *A set of parameters giving the measurements* $\{t_1, \cdots, t_K\} \times \{\omega_1, \cdots, \omega_d\}$ *is said* $F-$*complete in* $\mathcal{A}'$ *if there exists an open cover of* $\mathcal{A}'$

$$\mathcal{A}' = \bigcup_{p=1}^{P} \mathcal{A}'_p,$$

such that for each p *there exist* $k \in \{1, 2, \cdots, K\}$ *and* $\hat{\omega}_*$ *both depending on* p *such that*

$$|\widetilde{F}(t_k, \hat{\omega}_*)(\mathbf{a})| > 0, \ \mathbf{a} \in \mathcal{A}'_p. \tag{5.1.4}$$

A F-complete set of parameters giving the measurements provides a cover of $\mathcal{A}'$ by its finite subdomains, such that the determinant condition (5.1.3) is satisfied in each subdomain with different time point and S-D pairs. The following theorem gives a condition when we can have a F-complete set of parameters giving the measurements.

Theorem 5.1. *Suppose the determinant condition* (5.1.3) *holds in* $\mathcal{B}$ *at a time point* t_* *and for the source-detector pairs* $\omega_1, \cdots, \omega_d$. *Then for any* $\mathcal{B}' := B_{r'}(\mathbf{a}_0)$ *with* $0 < r' < r$,

$$\left\{(t_1, t_2, \cdots, t_d) \in \mathcal{T}^d : \{t_1, \cdots, t_d\} \times \{\omega_1, \cdots, \omega_d\} \textit{ is } F-\textit{complete in } \mathcal{B}'\right\}$$

is open and dense in $\mathcal{T}^d$.

The proof of this theorem can be given in the same way as that of Theorem 3.50 in [5] which basically uses the Whitney stratification for analytic sets. We will see in subsection 5.4, (1) that the determinant condition holds numerically for the S-D pairs chosen near but not distributed symmetrically around the target. However, it is not easy to prove this theoretically. Since there is a very strong smoothing effect of diffusion for u_m after $t = 0$, it is very natural to analyze the determinant condition for $0 < t \ll 1$. Hence we will derive the asymptotic expansions as $t \to +0$ for the derivatives of u_m given in Appendix. Based on this we can have the asymptotic expansion of $\mathcal{F}'(\mathbf{a})$ as $t \to +0$ by choosing 7 different S-D pairs. Our speculation was that the dominant part of this asymptotic expansion will satisfy the determinant condition. Unfortunately it was not the case. In fact we will see that the three column vectors of the dominant part coming from the derivatives with respect to a_3, b_3, P are mutually parallel to each other for any choice of 7 different S-D pairs. This could be related to the bad sensitivity of $\mathcal{F}(\mathbf{a})$ with respect to a_3, b_3 which we will see in subsection 5.4, (2). Hence we will only prove theoretically the following reduced determinant condition. That is under the assumption that we do know a_3, b_3, we show that the determinant condition holds for the Fréchet derivative of $\mathcal{F}(a)$ with respect to (a_1, b_1, a_2, b_2, P) for some particular choice of 5 S-D pairs for any $0 < t_* \ll 1$.

As a major tool for our next argument, we give the asymptotic expansion of following integral of the form

$$I(t) = \int_0^t (s(t-s))^{-\alpha} e^{-\frac{kt}{s(t-s)}} f(t,s)\, \mathrm{d}s \text{ as } t \to +0, \tag{5.1.5}$$

where $k > 0$, $\alpha < 1$ are constants and $f(t,s)$ is a smoothly extendable function in s, t with $0 \le t \le T$ which is not symmetric with respect to point $s = t/2$ of $(0,t)$ for a $t \in (0,T)$.

Lemma 5.1. *For $0 < t \ll 1$, (5.1.5) admits the following asymptotic expansion*

$$\begin{aligned} I(t) \sim \sum_{j=0}^{\infty} \frac{2^{-2j+1}}{(2j)!} t^{2(j-\alpha)+1} f^{(2j)}(t, t/2) e^{-4kt^{-1}} \times \Big[4^{\alpha-j-\frac{3}{2}} \Gamma\big(j+\frac{1}{2}\big)(kt^{-1})^{-(j+\frac{1}{2})} \\ + 4^{\alpha-j-\frac{5}{2}}(\alpha - j - 3/2)\Gamma\big(j+\frac{3}{2}\big)(kt^{-1})^{-(j+\frac{3}{2})} + \cdots \Big]. \end{aligned} \tag{5.1.6}$$

Proof. By expanding $f(t,s)$ into finite terms Taylor series around $s = t/2$ with respect to s, $f(t,s)$ admits the following asymptotic expansion

$$f(t,s) = f_0(t) + \frac{f'(t,\frac{t}{2})}{1!}\big(s - \frac{t}{2}\big) + \frac{f''(t,\frac{t}{2})}{2!}\big(s-\frac{t}{2}\big)^2 + \cdots$$

for $|s - t/2| \ll 1$, where $'$ denotes the derivative with respect to s. Since the function $s(t-s)$ in $(0,t)$ is symmetric at $s = t/2$ and an even function with respect to this point, we have

$$\begin{aligned} I(t) &\sim 2\int_0^{t/2} (s(t-s))^{-\alpha} e^{-\frac{kt}{s(t-s)}} \Big[f_0(t) + \frac{f''(t,\frac{t}{2})}{2!}\big(s-\frac{t}{2}\big)^2 + \frac{f^{(4)}(t,\frac{t}{2})}{4!}\big(s-\frac{t}{2}\big)^4 + \cdots \Big] \mathrm{d}s \\ &\sim \sum_{j=0}^{\infty} \frac{2}{(2j)!} \int_0^{t/2} (s(t-s))^{-\alpha} \big(s - \frac{t}{2}\big)^{2j} e^{-\frac{kt}{s(t-s)}} f^{(2j)}(t, t/2)\, \mathrm{d}s, \end{aligned}$$

where $f^{(2j)}$ denotes the derivative of f with respect to s of order $2j$. By introducing the new integration variable σ given by $\sigma = s/t$, this expansion becomes

$$\begin{aligned} I(t) &\sim \sum_{j=0}^{\infty} \frac{2}{(2j)!} t^{2(j-\alpha)+1} f^{(2j)}(t, t/2) \int_0^{1/2} (\sigma(1-\sigma))^{-\alpha} \big(\sigma - \frac{1}{2}\big)^{2j} e^{-\frac{kt^{-1}}{\sigma(1-\sigma)}} \, \mathrm{d}\sigma \\ &\sim \sum_{j=0}^{\infty} \frac{2}{(2j)!} t^{2(j-\alpha)+1} f^{(2j)}(t, t/2) H_{2j}(t) \end{aligned} \tag{5.1.7}$$

with

$$H_{2j}(t) := \int_0^{1/2} (\sigma(1-\sigma))^{-\alpha} \big(\sigma - \frac{1}{2}\big)^{2j} e^{-\frac{kt^{-1}}{\sigma(1-\sigma)}} \, \mathrm{d}\sigma.$$

Here we first transform the integration variable σ to $z = (\sigma(1-\sigma))^{-1}$ which transform $0 \le \sigma \le 1/2$ to $4 \le z < \infty$, and σ is given as $\sigma = \big(1 - \sqrt{1 - 4z^{-1}}\big)/2$. Then, we further transform z to $\zeta = z - 4$, which yields the following Laplace transform

$$H_{2j}(t) := 2^{-2j} e^{-4kt^{-1}} \int_0^{\infty} (\zeta + 4)^{\alpha - 2} (1 - 4(\zeta + 4)^{-1})^{j - 1/2} e^{-kt^{-1}\zeta} \, \mathrm{d}\zeta$$

with Laplace variable kt^{-1}.

Now recall Watson's lemma at the infinity which says that if $g \in C^{\infty}((0, \infty))$ is bounded on $[1, \infty)$ and satisfies

$$g(\zeta) \sim \zeta^{\mu} \sum_{n=0}^{\infty} g_n \zeta^{-n}, \quad 0 < \zeta \ll 1 \text{ with } \mu > -1,$$

then

$$\int_0^{\infty} e^{-\eta\zeta} g(\zeta) \, \mathrm{d}\zeta \sim \sum_{n=0}^{\infty} g_n \Gamma(\mu + n + 1) \eta^{-(\mu + n + 1)}, \quad \eta \gg 1.$$

By applying this lemma to $H_{2j}(t)$, we have for $0 < t \ll 1$ that

$$\begin{aligned} H_{2j}(t) \sim 2^{-2j} e^{-4kt^{-1}} \Bigg[& 4^{\alpha - j - \frac{3}{2}} \Gamma\left(j + \frac{1}{2}\right) (kt^{-1})^{-(j + \frac{1}{2})} \\ & + 4^{\alpha - j - \frac{5}{2}} (\alpha - j - 3/2) \Gamma\left(j + \frac{3}{2}\right) (kt^{-1})^{-(j + \frac{3}{2})} + \cdots \Bigg]. \end{aligned}$$

Then substituting this into (5.1.7), we obtain (5.1.6). The proof is complete. □

Based on the asymptotic expansion of the complementary error function given as

$$\sqrt{\pi} z e^{z^2} \operatorname{erfc}(z) \sim 1 + \sum_{m=1}^{\infty} (-1)^m \frac{(2m-1)!!}{(2z^2)^m}, \quad z \gg 1, \tag{5.1.8}$$

we first prepare the asymptotic expansions of the factors of $\widetilde{u}_m$ such as $K_3(0, y_3; t - s) K_3(y_3, 0; s)$ and $\widetilde{u}_i$, $i = 1, 2, 3$ in order to derive the asymptotic expansion of the derivatives of $\widetilde{u}_m$. They are given as follows.

Lemma 5.2. *For $y_3 > 0$, $t > s$ and given D, β, we have*

$$K_3(0, y_3; t - s) K_3(y_3, 0; s) \sim 4 e^{-\frac{{y_3}^2 t}{4cDs(t-s)}}, \quad t \to 0, \tag{5.1.9}$$

and

$$\begin{aligned}\widetilde{u}_3 &:= \int_0^t K_3(0, y_3; t-s) K_3(y_3, 0; s)\,\mathrm{d}s \\ &\sim \frac{1}{\sqrt{\pi}} \frac{16cDs(t-s)}{t} \left[{a_3}^{-1} e^{-\frac{{a_3}^2 t}{4cDs(t-s)}} - {b_3}^{-1} e^{-\frac{{b_3}^2 t}{4cDs(t-s)}} \right], \quad t \to 0.\end{aligned} \tag{5.1.10}$$

Moreover, if the geometrical parameters $\{a_i, b_i, i = 1, 2\}$ *of the cuboidal target and the positions of source* $(x_{s1}, x_{s2}, 0) \in \partial\Omega$ *and detector* $(x_{d1}, x_{d2}, 0) \in \partial\Omega$ *satisfy*

$$\left| a_i - \frac{s x_{di} + (t-s) x_{si}}{t} \right|, \quad \left| b_i - \frac{s x_{di} + (t-s) x_{si}}{t} \right| > \varepsilon \tag{5.1.11}$$

with some $0 < \varepsilon \ll 1$ *and for any* $0 \le s < t \le T$*, then we have*

$$\begin{aligned}\widetilde{u}_i \sim \frac{1}{\sqrt{\pi}} \sqrt{\frac{4cD(t-s)s}{t}} &\left\{ \left(a_i - \frac{s x_{di} + (t-s) x_{si}}{t} \right)^{-1} e^{-\frac{t\left(a_i - \frac{s x_{di} + (t-s) x_{si}}{t}\right)^2}{4cD(t-s)s}} \right. \\ &\left. - \left(b_i - \frac{s x_{di} + (t-s) x_{si}}{t} \right)^{-1} e^{-\frac{t\left(b_i - \frac{s x_{di} + (t-s) x_{si}}{t}\right)^2}{4cD(t-s)s}} \right\}, \quad i = 1, 2.\end{aligned} \tag{5.1.12}$$

Proof. For $y_3 > 0$ and given positive constants β and D, we know

$$\frac{y_3 + 2\beta cDs}{\sqrt{4cDs}} \to \infty, \quad s \to 0. \tag{5.1.13}$$

By the expression

$$K_3(y_3, 0; s) = 2e^{-\frac{{y_3}^2}{4cDs}} - 2\beta\sqrt{\pi cDs}\, e^{\beta y_3 + \beta^2 cDs} \operatorname{erfc}\left(\frac{y_3 + 2\beta cDs}{\sqrt{4cDs}} \right),$$

and the asymptotic expansion (5.1.8) of the complementary error function, we have

$$K_3(y_3, 0; s) \sim 2\left(1 - \frac{2\beta cDs}{y_3 + 2\beta cDs} \right) e^{-\frac{{y_3}^2}{4cDs}}, \quad s \to 0.$$

Similarly we have

$$K_3(0, y_3; t-s) \sim 2\left(1 - \frac{2\beta cD(t-s)}{y_3 + 2\beta cD(t-s)} \right) e^{-\frac{{y_3}^2}{4cD(t-s)}}, \quad 0 < t-s \to 0.$$

Hence from these two asymptotic expansions, we immediately have (5.1.9).

By (5.1.9) and the transformation of integration variable $y_3 = \sqrt{\frac{4cDs(t-s)}{t}}\, z$, we have for $t > s$

$$\begin{aligned}\widetilde{u}_3 &\sim 4\int_{a_3}^{b_3} e^{-\frac{t{y_3}^2}{4cDs(t-s)}}\,\mathrm{d}y_3 = 4\sqrt{\frac{4cDs(t-s)}{t}} \int_{\left(\frac{4cDs(t-s)}{t}\right)^{-\frac{1}{2}} a_3}^{\left(\frac{4cDs(t-s)}{t}\right)^{-\frac{1}{2}} b_3} e^{-z^2}\,\mathrm{d}z \\ &= 4\sqrt{\frac{4cDs(t-s)}{t}} \left\{ \operatorname{erfc}\left(\left(\frac{4cDs(t-s)}{t} \right)^{-\frac{1}{2}} a_3 \right) - \operatorname{erfc}\left(\left(\frac{4cDs(t-s)}{t} \right)^{-\frac{1}{2}} b_3 \right) \right\} \\ &\sim \frac{1}{\sqrt{\pi}} \frac{16cDs(t-s)}{t} \left[{a_3}^{-1} e^{-\frac{t{a_3}^2}{4cDs(t-s)}} - {b_3}^{-1} e^{-\frac{t{b_3}^2}{4cDs(t-s)}} \right], \quad t \to 0,\end{aligned}$$

which gives (5.1.10). Now by the expression of $\widetilde{u}_i$ $(i=1,2)$, we have

$$\begin{aligned}\widetilde{u}_i = &\operatorname{erfc}\left(\sqrt{\frac{t}{4cD(t-s)s}}\left(a_i - \frac{sx_{di}+(t-s)x_{si}}{t}\right)\right)\\ &-\operatorname{erfc}\left(\sqrt{\frac{t}{4cD(t-s)s}}\left(b_i - \frac{sx_{di}+(t-s)x_{si}}{t}\right)\right).\end{aligned}$$

Then under the condition (5.1.11), we can also prove (5.1.12) by using the asymptotic expansion of the complementary error function. This completes the proof. □

Based on Lemma 5.1 and Lemma 5.2, we can give the asymptotic expansions of the derivatives of $\widetilde{u}_m$ as follows.

Theorem 5.2. *Let the parameters of unknown cuboidal target* $\{a_i, b_i, i=1,2\}$ *and the positions of source* $x_s=(x_{s1},x_{s2},0)\in\partial\Omega$ *and detector* $x_d=(x_{d1},x_{d2},0)\in\partial\Omega$ *satisfy*

$$\left|a_i - \frac{sx_{di}+(t-s)x_{si}}{t}\right|,\ \left|b_i - \frac{sx_{di}+(t-s)x_{si}}{t}\right| > \varepsilon,\quad i=1,2 \tag{5.1.14}$$

with some $0<\varepsilon\ll 1$ *and for any* $0\le s<t\le T$, *and*

$$|b_1 - \frac{x_{d1}+x_{s1}}{2}| > |a_1 - \frac{x_{d1}+x_{s1}}{2}|,\ |b_2 - \frac{x_{d2}+x_{s2}}{2}| > |a_2 - \frac{x_{d2}+x_{s2}}{2}|. \tag{5.1.15}$$

Then we have the following asymptotic expansions of seven derivatives of $\widetilde{u}_m$ *as* $t\to +0$.

$$\begin{aligned}
\frac{\partial \widetilde{u}_m}{\partial a_1} \sim\ & -\frac{PC_1}{a_3}\left(a_2 - \frac{x_{d2}+x_{s2}}{2}\right)^{-1}\\
\times\ & \left(\frac{(a_1-x_{s1})^2+{a_3}^2}{4cDt}\right)^{-\frac{1}{2}} e^{-\left(\frac{\|x_d-x_s\|^2}{4cDt}+c\mu_a t\right)} e^{-\frac{\left\|(a_1,a_2,a_3)-\frac{x_d+x_s}{2}\right\|^2}{cDt}}, && (5.1.16)\\
\frac{\partial \widetilde{u}_m}{\partial b_1} \sim\ & \frac{PC_1}{a_3}\left(a_2 - \frac{x_{d2}+x_{s2}}{2}\right)^{-1}\\
\times\ & \left(\frac{(b_1-x_{s1})^2+{a_3}^2}{4cDt}\right)^{-\frac{1}{2}} e^{-\left(\frac{\|x_d-x_s\|^2}{4cDt}+c\mu_a t\right)} e^{-\frac{\left\|(b_1,a_2,a_3)-\frac{x_d+x_s}{2}\right\|^2}{cDt}}, && (5.1.17)\\
\frac{\partial \widetilde{u}_m}{\partial a_2} \sim\ & -\frac{PC_1}{a_3}\left(a_1 - \frac{x_{d1}+x_{s1}}{2}\right)^{-1}\\
\times\ & \left(\frac{(a_2-x_{s2})^2+{a_3}^2}{4cDt}\right)^{-\frac{1}{2}} e^{-\left(\frac{\|x_d-x_s\|^2}{4Dt}+c\mu_a t\right)} e^{-\frac{\left\|(a_1,a_2,a_3)-\frac{x_d+x_s}{2}\right\|^2}{cDt}}, && (5.1.18)\\
\frac{\partial \widetilde{u}_m}{\partial b_2} \sim\ & \frac{PC_1}{a_3}\left(a_1 - \frac{x_{d1}+x_{s1}}{2}\right)^{-1}\\
\times\ & \left(\frac{(b_2-x_{s2})^2+{a_3}^2}{4cDt}\right)^{-\frac{1}{2}} e^{-\left(\frac{\|x_d-x_s\|^2}{4cDt}+c\mu_a t\right)} e^{-\frac{\left\|(a_1,b_2,a_3)-\frac{x_d+x_s}{2}\right\|^2}{cDt}}, && (5.1.19)
\end{aligned}$$

$$\begin{aligned}
\frac{\partial \widetilde{u}_m}{\partial a_3} &\sim -PC_2\left(a_1-\frac{x_{d1}+x_{s1}}{2}\right)^{-1}\left(a_2-\frac{x_{d2}+x_{s2}}{2}\right)^{-1}\\
&\quad\times \left(\frac{{a_3}^2}{4cDt}\right)^{-\frac{1}{2}} e^{-\left(\frac{\|x_d-x_s\|^2}{4cDt}+c\mu_a t\right)} e^{-\frac{\left\|(a_1,a_2,a_3)-\frac{x_d+x_s}{2}\right\|^2}{cDt}}, && (5.1.20)\\
\frac{\partial \widetilde{u}_m}{\partial b_3} &\sim PC_2\left(a_1-\frac{x_{d1}+x_{s1}}{2}\right)^{-1}\left(a_2-\frac{x_{d2}+x_{s2}}{2}\right)^{-1}\\
&\quad\times \left(\frac{{b_3}^2}{4cDt}\right)^{-\frac{1}{2}} e^{-\left(\frac{\|x_d-x_s\|^2}{4cDt}+c\mu_a t\right)} e^{-\frac{\left\|(a_1,a_2,a_3)-\frac{x_d+x_s}{2}\right\|^2}{cDt}}, && (5.1.21)\\
\frac{\partial \widetilde{u}_m}{\partial P} &\sim C_3\left(a_1-\frac{x_{d1}+x_{s1}}{2}\right)^{-1}\left(a_2-\frac{x_{d2}+x_{s2}}{2}\right)^{-1}\\
&\quad\times \frac{t}{a_3}\left(\frac{{a_3}^2}{4cDt}\right)^{-\frac{1}{2}} e^{-\left(\frac{\|x_d-x_s\|^2}{4cDt}+c\mu_a t\right)} e^{-\frac{\left\|(a_1,a_2,a_3)-\frac{x_d+x_s}{2}\right\|^2}{cDt}}, && (5.1.22)
\end{aligned}$$

where $\|\xi\|$ *is the Euclidean distance of any three dimensional vector* ξ*, and* $C_1 := \frac{c\gamma}{16\pi^{7/2}}\Gamma\left(\frac{1}{2}\right)$*,* $C_2 := \frac{c\gamma}{32\pi^3}\Gamma\left(\frac{1}{2}\right)$*,* $C_3 := \frac{\gamma c^2 D}{32\pi^{7/2}}\Gamma\left(\frac{1}{2}\right)$ *are constants which are independent of time* t*, cuboidal target and S-D pair.*

Proof. We will only show how to derive the asymptotic expansion for $\frac{\partial \widetilde{u}_m}{\partial a_1}$. First note that we can easily see $\frac{\partial \widetilde{u}_m}{\partial a_1}$ in the form

$$\frac{\partial \widetilde{u}_m}{\partial a_1} = PC\int_0^t \frac{-\sqrt{t}}{s(t-s)\sqrt{\pi c D}} e^{-\frac{\left(t(a_1-x_{s1})-s(x_{d1}-x_{s1})\right)^2}{4cDts(t-s)}} u_2 u_3 \,\mathrm{d}s \qquad (5.1.23)$$

as in Appendix with $C := C(x_{d1}, x_{s1}, x_{d2}, x_{s2}, t)$ given in Theorem 4.1. Then taking account of the condition (5.1.14) and using Lemma 5.2, we have

$$\frac{\partial \widetilde{u}_m}{\partial a_1} \sim -\frac{32PcDC}{\pi^{\frac{3}{2}} t}\int_0^t \sqrt{s(t-s)}\left(\frac{1}{a_3} e^{-\frac{\left((a_1-x_{s1})^2+{a_3}^2\right)t}{4cDs(t-s)}} - \frac{1}{b_3} e^{-\frac{\left((a_1-x_{s1})^2+{b_3}^2\right)t}{4cDs(t-s)}}\right) f(t,s)\,\mathrm{d}s$$

with

$$\begin{aligned}
f(t,s) &:= e^{-\frac{-2ts(a_1-x_{s1})(x_{d1}-x_{s1})+s^2(x_{d1}-x_{s1})^2}{4cDts(t-s)}}\\
&\quad\times\left\{\left(a_2-\frac{sx_{d2}+(t-s)x_{s2}}{t}\right)^{-1} e^{-\frac{\left(a_2-\frac{sx_{d2}+(t-s)x_{s2}}{t}\right)^2 t}{4cD(t-s)s}}\right.\\
&\quad\left.-\left(b_2-\frac{sx_{d2}+(t-s)x_{s2}}{t}\right)^{-1} e^{-\frac{\left(b_2-\frac{sx_{d2}+(t-s)x_{s2}}{t}\right)^2 t}{4cD(t-s)s}}\right\},
\end{aligned}$$

which is not symmetric in $(0, t)$ with respect to the point $s = t/2$. Hence to exclude the integral in the above asymptotic expansion, we need to use Lemma 5.1.

To be precise let

$$k_1 := \frac{(a_1-x_{s1})^2+{a_3}^2}{4cD},\quad k_2 := \frac{(a_1-x_{s1})^2+{b_3}^2}{4cD}, \qquad (5.1.24)$$

and apply Lemma 5.1 with $\alpha = -\frac{1}{2}$. Then we have

$$\begin{aligned}
\frac{\partial \widetilde{u}_m}{\partial a_1} &\sim \frac{-Pc\gamma}{2\pi^{7/2}} e^{-\left(\frac{(x_{d1}-x_{s1})^2+(x_{d2}-x_{s2})^2}{4cDt}+c\mu_a t\right)} \sum_{j=0}^{\infty} \frac{2^{-2j+1}}{(2j)!} t^{2j} f^{(2j)}(t, t/2) \\
&\times \left\{ \frac{1}{a_3} e^{-4k_1 t^{-1}} \times [4^{-2-j}\Gamma(j+1/2)\left(k_1 t^{-1}\right)^{-(j+\frac{1}{2})} \right. \\
&-4^{-3-j}\,(j+2)\,\Gamma\big(j+3/2\big)\big(k_1 t^{-1}\big)^{-(j+3/2)} + \cdots] \\
&-\frac{1}{b_3} e^{-4k_2 t^{-1}} \times [4^{-2-j}\Gamma(j+1/2)\left(k_2 t^{-1}\right)^{-(j+1/2)} \\
&\left. -4^{-3-j}(j+2)\Gamma(j+3/2)(k_2 t^{-1})^{-(j+3/2)} + \cdots] \right\} \\
&\sim -\frac{Pc\gamma}{16\pi^{7/2}} e^{-\left(\frac{(x_{d1}-x_{s1})^2+(x_{d2}-x_{s2})^2}{4cDt}+c\mu_a t\right)} f^{(0)}\big(t, \frac{t}{2}\big) \\
&\times \left\{ \frac{1}{a_3} e^{-4k_1 t^{-1}} \Gamma\big(1/2\big)\big(k_1 t^{-1}\big)^{-\frac{1}{2}} - \frac{1}{b_3} e^{-4k_2 t^{-1}} \Gamma\big(1/2\big)\big(k_2 t^{-1}\big)^{-\frac{1}{2}} \right\}, \quad t \to 0,
\end{aligned}$$

where

$$\begin{aligned}
f^{(0)}\big(t, \frac{t}{2}\big) = e^{-\frac{-4(a_1-x_{s1})(x_{d1}-x_{s1})+(x_{d1}-x_{s1})^2}{4cDt}} &\left\{ \left(a_2 - \frac{x_{d2}+x_{s2}}{2}\right)^{-1} e^{-\frac{\left(a_2-\frac{x_{d2}+x_{s2}}{2}\right)^2}{cDt}} \right. \\
&\left. - \left(b_2 - \frac{x_{d2}+x_{s2}}{2}\right)^{-1} e^{-\frac{\left(b_2-\frac{x_{d2}+x_{s2}}{2}\right)^2}{cDt}} \right\}.
\end{aligned} \tag{5.1.25}$$

To finish the proof recall the condition (5.1.15) and note that $k_2 > k_1$ due to $b_3 > a_3$. Then just extract the dominant part to have

$$\begin{aligned}
\frac{\partial \widetilde{u}_m}{\partial a_1} \sim -\frac{Pc\gamma}{16\pi^{7/2} a_3} \Gamma\big(\frac{1}{2}\big) \left(a_2 - \frac{x_{d2}+x_{s2}}{2}\right)^{-1} \left(\frac{(a_1-x_{s1})^2 + {a_3}^2}{4cDt}\right)^{-1/2} \\
\times\, e^{-\left(\frac{(x_{d1}-x_{s1})^2+(x_{d2}-x_{s2})^2}{4cDt}+c\mu_a t\right)} e^{-\frac{\left(a_1-\frac{x_{d1}+x_{s1}}{2}\right)^2}{cDt}} e^{-\frac{\left(a_2-\frac{x_{d2}+x_{s2}}{2}\right)^2}{cDt}} e^{-\frac{{a_3}^2}{cDt}},\ t \to 0.
\end{aligned}$$

Thus we have proved (5.1.16). ☐

Now we are ready to give the validity of the reduced determinant condition. Let's begin by giving the difference of the reduced determinant condition to the determinant condition. That is in the definition (5.1.1) of $\widetilde{F}(t_*, \hat{\omega}_*)$, take $d = 5$ and assume that a_3, b_3 are known so that we can fix them. Consequently we interpret that ∇ in the definition (5.1.1) of $\widetilde{F}(t_*, \hat{\omega}_*)$ is with respect to (a_1, b_1, a_2, b_2, P). Next we give some theoretical result on the validity of the reduced determinant condition.

Theorem 5.3. *Let* $\mathbf{a}^\dagger = (a_1, b_1, a_2, b_2, a_3, b_3, P) \in \mathcal{A}$ *be the cuboidal target and* $\hat{\omega}_* = \{\omega_k := \left(x_s^k, x_d^k\right) \in \partial\Omega \times \partial\Omega,\ k = 1, 2, \cdots, 5\}$ *be the set of source-detector pairs satisfying the conditions in Theorem 5.2. Assume that* a_3 *is very small. Further we will choose* $\hat{\omega}_*$ *in a way described in the proof of this theorem. Then there exists* $r > 0$ *such that*

$$\widetilde{F}(t_*, \hat{\omega}_*)(\mathbf{a}) \neq 0,\ \mathbf{a} \in \mathcal{B} := B_r(\mathbf{a}^\dagger) \text{ for any fixed } 0 < t_* \ll 1, \tag{5.1.26}$$

where $\widetilde{F}(t_*, \hat{\omega}_*)$ *is defined by (5.1.1).*

Proof. We firstly recall that the S-D pair is denoted by $\omega = (x_s, x_d)$ with $x_s = (x_{s1}, x_{s2})$ and $x_d = (x_{d1}, x_{d2})$. For simplicity, we further denote

$$\xi_1 := x_{s1}, \quad \eta_1 := \frac{x_{d1} + x_{s1}}{2}, \quad \xi_2 := x_{s2}, \quad \eta_2 := \frac{x_{d2} + x_{s2}}{2}.$$

We assume $X := (\xi_1, \eta_1, \xi_2, \eta_2)$ satisfying (5.1.14) and (5.1.15). Take 5 of such X denoted by $X_k := (\xi_1^k, \eta_1^k, \xi_2^k, \eta_2^k)$ for $k = 1, 2, \cdots, 5$.

By factoring out some common constants and

$$\sqrt{4cDt},\ e^{-\left(\frac{\left\|x_d^k - x_s^k\right\|^2}{4cDt} + c\mu_a t\right)},\ e^{-\frac{\left\|(a_1,a_2,a_3) - \frac{x_d^k + x_s^k}{2}\right\|^2}{cDt}},\ k = 1, \cdots 5$$

and ignoring very small a_3^2 in the dominant part of the asymptotic exapansion of $\widetilde{F}(t_*, \hat{\omega}_*)(\mathbf{a})$, then the dominant part becomes

$$A := \begin{bmatrix} \vec{A_1}' \\ \vec{A_2}' \\ \vec{A_3}' \\ \vec{A_4}' \\ \vec{A_5}' \end{bmatrix}, \tag{5.1.27}$$

where the row vectors $\vec{A_k}'$ $(k = 1, 2, \cdots, 5)$ are defined by

$$\begin{aligned} \vec{A_k}' := \Big(&(a_2 - \eta_2^k)^{-1}(a_1 - \xi_1^k)^{-1},\ (a_2 - \eta_2^k)^{-1}(b_1 - \xi_1^k)^{-1}, \\ &(a_1 - \eta_1^k)^{-1}(a_2 - \xi_2^k)^{-1},\ (a_1 - \eta_1^k)^{-1}(b_2 - \xi_2^k)^{-1},\ (a_1 - \eta_1^k)^{-1}(a_2 - \eta_2^k)^{-1} \Big), \end{aligned}$$

respectively. Here for simplicity, we have mod out what we have factored out.

To have the determinant conditions, we need to show that it is possible to choose $X_k (k = 1, 2, \cdots, 5)$ in some general way satisfying $\det(A) \neq 0$. This should be possible because 20 free parameters in $X_k (k = 1, 2, \cdots, 5)$. For instance, we can take $X_k := (\xi_1^k, \xi_2^k, \eta_1^k, \eta_2^k)$ for $k = 1, 2, 3$ such that the row vectors

$$\vec{B_k}' = \Big((a_2 - \eta_2^k)^{-1}(a_1 - \xi_1^k)^{-1},\ (a_1 - \eta_1^k)^{-1}(a_2 - \xi_2^k)^{-1},\ (a_1 - \eta_1^k)^{-1}(a_2 - \eta_2^k)^{-1} \Big)$$

for $k = 1, 2, 3$ are linearly independent. Then, appropriately take X_4, X_5 to make the condition $\det(A)$ is satisfied, where A is defined by (5.1.27) with respect to the selected 5 S-D pairs in above way. The proof is complete. □

We note that we have given in Theorem 5.3 the verification of the reduced determinant condition only for some extreme choice of S-D pairs.

5.2 Local Solvability and Its Lipschitz Stability

We simply denote $M(t_*, \hat{\omega}_*)(\mathbf{a})$ by $M(\mathbf{a})$ for fixed $t_* \in \mathcal{T}$, $\hat{\omega}_* = (\omega_1, \cdots, \omega_d)$ and consider the associated operator $M : \mathcal{B} \ni \mathbf{a} \mapsto M(\mathbf{a}) \in \mathbb{R}^d$. It is clear by the expression (4.1.13) that M is continuous in $\mathcal{B}$ and its Fréchet derivative M' is locally Lipschitz continuous in $\mathcal{B}$ in terms of the expressions of $\nabla \widetilde{u}_m$ shown in Appendix. Suppose the determinant condition (5.1.3) holds in $\mathcal{B}$ at a time point t_* and for the source-detector pairs $\omega_1, \cdots, \omega_d$. Then M' is invertible and its inverse $(M')^{-1}$ is locally continuous in $\mathcal{B}$.

Moreover, there exists a constant $\tilde{C} > 0$ such that

$$\|\mathcal{G}(\mathbf{a}_2, \mathbf{a}_0) - \mathcal{G}(\mathbf{a}_1, \mathbf{a}_0)\| \leq \tilde{C}\, \|\mathbf{a}_2 - \mathbf{a}_1\|\,, \ \mathbf{a}_1, \mathbf{a}_2 \in \mathcal{B}, \tag{5.2.1}$$

where

$$\mathcal{G}(\mathbf{a}, \mathbf{a}_0) := \left(\int_0^1 M'(\mathbf{a}_0 + \theta(\mathbf{a} - \mathbf{a}_0))\ \mathrm{d}\theta \right)^{-1}, \quad \mathbf{a} \in \mathcal{B}. \tag{5.2.2}$$

Now let $\mathbf{a}^\dagger$ satisfy

$$M(\mathbf{a}^\dagger) = H^*, \quad \mathbf{a}^\dagger \in \mathcal{B}, \tag{5.2.3}$$

where H^* is defined by (5.1.2). Then we can prove the local solvability and local Lipschitz stability of the inverse problem. More precisely we first have from the inverse mapping theorem the following local solvability (see Theorem 9.23 in [9]).

Theorem 5.4. *Under the same condition in Theorem 5.1, there exist $\rho > 0$, $\tilde{r} > 0$ such that $M(\tilde{\mathbf{a}}) = \tilde{H}^*$ is uniquely solvable in $\tilde{\mathbf{a}} \in B_{\tilde{r}}(\mathbf{a}^\dagger) \subset \mathcal{B}$ for any $\tilde{H}^* \in B_\rho(H^*)$.*

Theorem 5.4 means that if the given measurement data are near by exact measurement data there exists unique solution which is also close to the exact solution.

By (5.2.1)-(5.2.2) we can immediately have

Theorem 5.5. *Under the same condition in Theorem 5.1, for any $\mathbf{a}_1, \mathbf{a}_2 \in \mathcal{B}$, $H_1^*, H_2^* \in B_\rho(H^*)$, if $M(\mathbf{a}_1) = H_1^*$, $M(\mathbf{a}_2) = H_2^*$ are satisfied, there exists a constant $C_F > 0$ such that*

$$\|\mathbf{a}_1 - \mathbf{a}_2\| \leq C_F\, \|H_1^* - H_2^*\|\,. \tag{5.2.4}$$

5.3 Convergence of Levenberg-Marquardt method

In practice, we do not know the data exactly. Instead, we only have an approximate measured data $H^\delta \in \mathcal{H}^{NK}$ satisfying

$$\left\| H^\delta - H \right\| \leq \delta \tag{5.3.1}$$

with $\delta > 0$. For inversion, we apply Levenberg-Marquardt (LM) method to solve (5.0.3) iteratively by the following procedure

$$\mathbf{a}_{k+1}^\delta = \mathbf{a}_k^\delta + \left(\mathcal{F}'(\mathbf{a}_k^\delta)^* \mathcal{F}'(\mathbf{a}_k^\delta) + \alpha_k I \right)^{-1} \mathcal{F}'(\mathbf{a}_k^\delta)^* (H^\delta - \mathcal{F}(\mathbf{a}_k^\delta)), \tag{5.3.2}$$

where $\mathcal{F}'(z)$ is the Fréchet derivative of $\mathcal{F}(z)$ defined by (5.0.3) and $\mathcal{F}'(z)^*$ is its adjoint. LM iteration scheme has a regularization parameter α_k at each $k+1$ step. This is chosen in such a way that $\mathbf{a}_{k+1}^\delta - \mathbf{a}_k^\delta$ is the minimum norm solution of

$$\left\| H^\delta - \mathcal{F}(\mathbf{a}_k^\delta) - \mathcal{F}'(\mathbf{a}_k^\delta)(\mathbf{a}_{k+1}^\delta - \mathbf{a}_k^\delta) \right\| = c_1 \left\| H^\delta - \mathcal{F}(\mathbf{a}_k^\delta) \right\| \tag{5.3.3}$$

with any fixed $0 < c_1 < 1$ (see [13]). Concerning the convergence of LM iteration scheme, it is well-known that $\mathbf{a}_k$ converges to a solution $\mathbf{a}$ of $\mathcal{F}(\mathbf{a}) = H$ $(\delta = 0)$ as $k \to \infty$ if we have the so called tangential cone condition

$$\left\| \mathcal{F}(\mathbf{a}) - \mathcal{F}(\tilde{\mathbf{a}}) - \mathcal{F}'(\mathbf{a})(\mathbf{a} - \tilde{\mathbf{a}}) \right\| \leq c_2\, \|\mathbf{a} - \tilde{\mathbf{a}}\|\, \|\mathcal{F}(\mathbf{a}) - \mathcal{F}(\tilde{\mathbf{a}})\|\,, \ \mathbf{a},\, \tilde{\mathbf{a}} \in \mathcal{B}, \tag{5.3.4}$$

where $\mathcal{F}(\mathbf{a}^\dagger) = H$.

Remark 5.1. *The tangential cone condition follows from the Hölder type stability estimate with Hölder exponent larger than* $1/2$ *(see [10]). In particular, for the case* $\mathcal{F} = M$*, the tangential cone condition follows from the local Lipshitz stability estimate* (5.2.4). *More precisely we have the following theorem.*

Theorem 5.6. *Suppose* $\mathcal{F} = M$ *with some fixed* $t_* \in \mathcal{T}$ *and* $\hat{\omega}_*$ *such that the determinant condition holds. Then the tangential cone condition (5.3.4) holds.*

Proof. For any $\mathbf{a}, \tilde{\mathbf{a}} \in \mathcal{B}$, observe that

$$\begin{aligned}
& \left\|\mathcal{F}(\mathbf{a}) - \mathcal{F}(\tilde{\mathbf{a}}) - \mathcal{F}'(\mathbf{a})(\mathbf{a}-\tilde{\mathbf{a}})\right\| \\
= & \left\|\left(\int_0^1 \mathcal{F}'(\tilde{\mathbf{a}} + \theta(\mathbf{a}-\tilde{\mathbf{a}}))\,\mathrm{d}\theta\right)(\mathbf{a}-\tilde{\mathbf{a}}) - \mathcal{F}'(\mathbf{a})(\mathbf{a}-\tilde{\mathbf{a}})\right\| \\
= & \left\|\left(\int_0^1 (\mathcal{F}'(\tilde{\mathbf{a}} + \theta(\mathbf{a}-\tilde{\mathbf{a}})) - \mathcal{F}'(\mathbf{a}))\,\mathrm{d}\theta\right)(\mathbf{a}-\tilde{\mathbf{a}})\right\| \\
\le & \left\|\int_0^1 (\mathcal{F}'(\tilde{\mathbf{a}} + \theta(\mathbf{a}-\tilde{\mathbf{a}})) - \mathcal{F}'(\mathbf{a}))\,\mathrm{d}\theta\right\| \|\mathbf{a}-\tilde{\mathbf{a}}\|.
\end{aligned}$$

By the Lipschitz continuity of $\mathcal{F}'$ we have

$$\begin{aligned}
\left\|\int_0^1 (\mathcal{F}'(\tilde{\mathbf{a}} + \theta(\mathbf{a}-\tilde{\mathbf{a}})) - \mathcal{F}'(\mathbf{a}))\,\mathrm{d}\theta\right\| & \le \int_0^1 \left\|\mathcal{F}'(\tilde{\mathbf{a}} + \theta(\mathbf{a}-\tilde{\mathbf{a}})) - \mathcal{F}'(\mathbf{a})\right\| \mathrm{d}\theta \, \|\mathbf{a}-\tilde{\mathbf{a}}\| \\
& \le C_L \int_0^1 (1-\theta)\,\mathrm{d}\theta \, \|\mathbf{a}-\tilde{\mathbf{a}}\| \le C_L \|\mathbf{a}-\tilde{\mathbf{a}}\|
\end{aligned}$$

due to $(\tilde{\mathbf{a}} + \theta(\mathbf{a}-\tilde{\mathbf{a}})) - \mathbf{a} = (1-\theta)(\tilde{\mathbf{a}} - \mathbf{a})$ and $\int_0^1 (1-\theta)\,\mathrm{d}\theta \le 1$, where C_L is a positive constant. By (5.2.4), there exists a constant C_F such that $\|\mathbf{a}-\tilde{\mathbf{a}}\| \le C_F \|\mathcal{F}(\mathbf{a}) - \mathcal{F}(\tilde{\mathbf{a}})\|$. Hence we complete the proof by setting $c_2 := C_L C_F$. ☐

In terms of the expressions of $\nabla \widetilde{u}_m$ given in Appendix, $\mathcal{F}'(\mathbf{a})$ is uniformly bounded in $\mathcal{B}$. Then, by the tangential cone condition, we have the convergence of LM iteration scheme.

Theorem 5.7. *Assume the tangential cone condition is satisfied. For exact data* H*, if the initial guess* $\mathbf{a}_0$ *satisfies*

$$\left\|\mathbf{a}_0 - \mathbf{a}^\dagger\right\| < \frac{c_1}{c_2}, \tag{5.3.5}$$

then the sequence $\mathbf{a}_k$, $k = 0, 1, \cdots$ *defined by* (5.3.2) *converges to a solution* $\mathbf{a}$ *of* $\mathcal{F}(\mathbf{a}) = H$ *as* $k \to \infty$*. Moreover, if the kernel condition*

$$\mathcal{N}(\mathcal{F}'(\mathbf{a}^\dagger)) \subset \mathcal{N}(\mathcal{F}'(\mathbf{a})) \quad \textit{for all } \mathbf{a} \in \mathcal{B} \tag{5.3.6}$$

holds, then $\mathbf{a}_k \to \mathbf{a}^\dagger$ *as* $k \to \infty$*. Here for instance* $\mathcal{N}(\mathcal{F}'(\mathbf{a}))$ *denotes the kernel of* $\mathcal{F}'(\mathbf{a})$*. (See, e.g. [11] and the references therein.)*

This theorem means that the exact solution $\mathbf{a}^\dagger \in \mathcal{B}$ of equation (5.0.3) with exact data H can be recovered by LM iteration scheme.

For the noisy data H^δ, we have to set up some stopping rule to terminate the iteration appropriately. The most commonly used stopping rule is the discrepancy principle which requires to stop the iteration at the first iteration index $k_* := k_*(\delta, H^\delta)$ for which

$$\left\|H^\delta - \mathcal{F}(\mathbf{a}^\delta_{k_*})\right\| \le \lambda\delta \tag{5.3.7}$$

with some fixed constant $\lambda > 1/c_1$.

Theorem 5.8. *Suppose the tangential cone condition for* $\mathcal{F}'(\mathbf{a})$ *is satisfied in* $\mathcal{B}$*. Let* k_* *be chosen according to the stopping rule (5.3.7) with* $\lambda > 1/c_1$*. Then starting from the initial guess* $\mathbf{a}_0$ *which satisfies*

$$\left\|\mathbf{a}_0 - \mathbf{a}^\dagger\right\| \le \frac{c_1\lambda - 1}{c_2(1+\lambda)}, \tag{5.3.8}$$

the discrepancy principle (5.3.7) terminates LM iteration scheme with α_k *determined from (5.3.3) after finitely many iterations* k_* *and we have*

$$k_*(\delta, H^\delta) = O(1 + |\ln\delta|).$$

Further the sequence $\mathbf{a}_k^\delta$*,* $k = 0, 1, \cdots$ *converges to a solution* $\mathbf{a}$ *of the equation* $\mathcal{F}(\mathbf{a}) = H$ *as* $\delta \to 0$ *(see [16]). Moreover, if the kernel condition*

$$\mathcal{N}(\mathcal{F}'(\mathbf{a}^\dagger)) \subset \mathcal{N}(\mathcal{F}'(\mathbf{a})) \quad \textit{for all } \mathbf{a} \in \mathcal{B} \tag{5.3.9}$$

holds, then $\mathbf{a}_k^\delta \to \mathbf{a}^\dagger$ *as* $\delta \to 0,\ k \to \infty$ *(see [11]).*

From Theorem 5.8, under some restrictions, the sequence $\mathbf{a}_k^\delta$ for $\delta \ge 0$ can converge to a solution $\mathbf{a}$ of $\mathcal{F}(\mathbf{a}) = H^\delta$. However, it can be observed also that the convergence heavily depends on the initial guess $\mathbf{a}_0$, i.e., a good initial guess is essential to ensure the convergence to expected solution in LM iteration scheme. In addition, the convergence speed depends also on the initial guess, i.e., a good initial guess is also important to save the number of iteration, see, e.g. [10].

Thus, based on above discussions, we summarize our main task to be answered are the following two questions.

- 1. How to select a good set of parameters giving the measurements such that the determinant condition (5.1.3) is valid.
- 2. How to obtain a stable inversion and accelerate the convergence speed (select a good initial guess).

5.4 Numerical implementations

In this section, we verify the results in section 5.2 numerically. Let

$$\mathbf{a} = (a_1, b_1, a_2, b_2, a_3, b_3, P) = (-1, 1, -3, 3, 10, 12, 0.01) \tag{5.4.1}$$

be a cuboidal target, and let the other physical parameters are the same as (2.3.3).

Numerically testing the determinant condition

For simplicity, we consider a set of source-detector (S-D) pairs $\{\omega_i = (S_i, D_i) \in \partial\Omega \times \partial\Omega,\ i = 1, \cdots, 10\}$ as shown in Figure 5.1, (a), where the corresponding sources and detectors are $S_i := (x_{s1}^i, 12, 0)$ and $D_i := (x_{d1}^i, -8, 0)$ with $\{x_{s1}^i\}_{i=1:10} = \{x_{d1}^i\}_{i=1:10} =: \{x_1^i\}_{i=1:10} = \{-28, -24, -20, -16, -12, -8, -4, 5, 10, 15\}$. We note here they are not symmetrical about the cuboidarl target. Let t_{peak}^i be the peak time corresponding to i-th S-D pair ω_i, where we expect the intensity of emission light on time t_{peak}^i is strongest in the time interval $(0, T)$. By arbitrarily choosing 7 S-D pairs from these 10 S-D pairs, there are 120 choices. Let $\{\omega_{k_1}, \omega_{k_2}, \cdots, \omega_{k_7}\}$ be the k-th chosen S-D pairs, and we compute each corresponding rank of sensitivity matrix and plot its value to have Figure 5.1, (b).

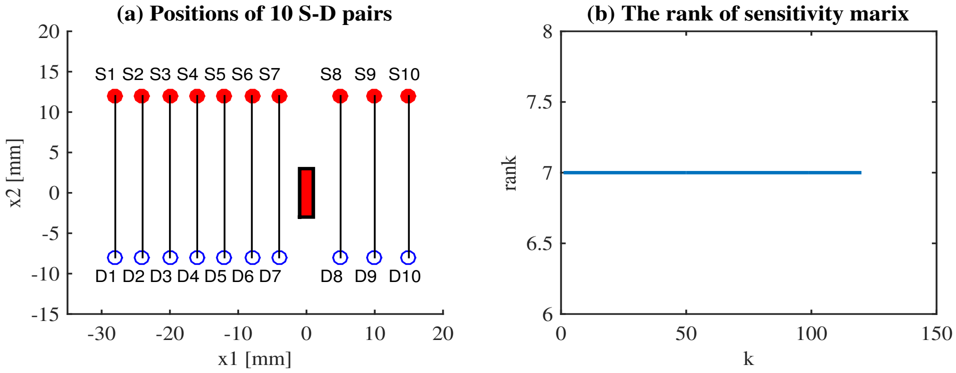

FIGURE 5.1: (a) A set of S-D pairs and the projection of cuboidal target to $\partial\Omega$; (b) The rank of sensitivity matrix with different selected 7 S-D pairs.

From Figure 5.1, it can be observed that the determinant condition is valid for the selected 7 S-D pairs which are not distributed symmetrically about the cuboidal target. In other words, the determinant condition will be not valid if there exist two S-D pairs among the selected 7 ones are distributed symmetrically about the cuboidal target. For instance, we firstly choose 6 S-D pairs which are S1-D1, S2-D2, S3-D3, S4-D4, S5-D5 and S6-D6 as shown in Figure 5.1. However, we let the 7-th S-D pair locate at $\bar{S}_7 = (8, 12, 0)$ and $\bar{D}_7 = (8, -8, 0)$. Obviously, S6-D6 and S̄7-D̄7 are symmetrical about the cuboidal target such that the 7 S-D pairs selected in this way don't satisfy the determinant condition.

The sensitivity analysis

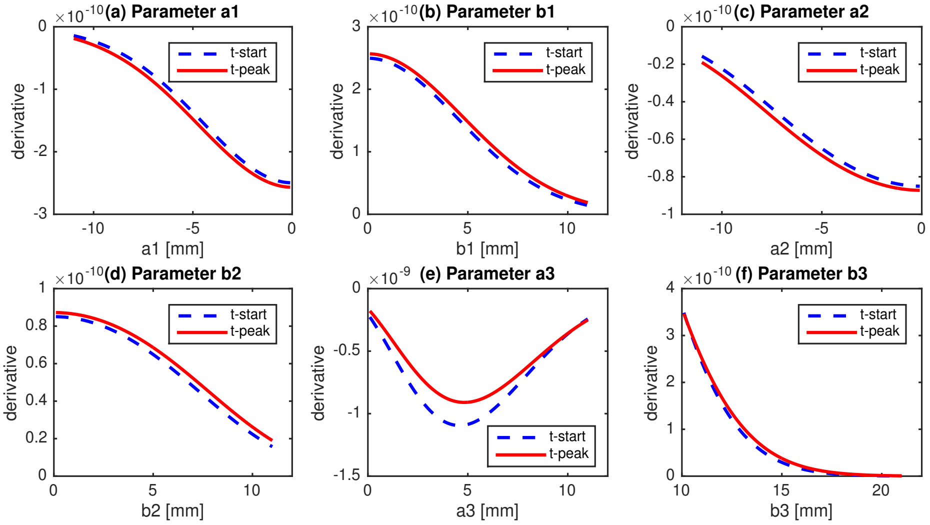

FIGURE 5.2: The sensitivities on different parameters on t_{start} and t_{peak}.

We can easily speculate from LM iteration scheme (5.3.2), the property of sensitivity matrix $\mathcal{F}'$ has some strong influence on recovering the unknown target. To see this take measurement time on t_{peak} and S-D pair ω with point source $S = (0, 10, 0)$, detector

$D = (0, -10, 0)$, and examine the behaviors of $\nabla\widetilde{u}_m(\mathbf{a})(t_{peak}, \omega)$ with different $\mathbf{a}$. From (4.1.13), it is easy to obtain the expressions of $\nabla\widetilde{u}_m(\mathbf{a})(t_{peak}, \omega)$ given in Appendix and $\frac{\partial\widetilde{u}_m(\mathbf{a})}{\partial P}$ is a positive constant. As before, let t_{peak} be the peak time. We consider the sensitivities on different parameters such as $a_1, b_1, a_2, b_2, a_3, b_3$ on time t_{peak} and $t_{start} := t_{peak} - 10\Delta t$ with $\Delta t = 6.67$ ps. The values are shown in Figure 5.2, respectively.

It can be observed from Figure 5.2 that the sensitivities on a_1 and b_1 are symmetric, and the same for parameters a_2 and b_2. This is because the source and detector are symmetric about the target. On the other hand, it can be seen also that how the sensitivity changes with respect to a_3 is not uniform, i.e., it doesn't change monotonically, which makes LM iteration scheme unstable. Hence, recovering the parameters a_3 and b_3 of the unknown cuboidal target is generally difficult, i.e, the recovery of the thickness of the target should be unstable than the recovery of its other geometric information such as the length and width (denoted by $b_1 - a_1$ or $b_2 - a_2$). We will test that in Chapter 6.

Comparison of the set of parameters by SVD

Let $\hat{t} := \{t_1, t_2, \cdots, t_K\} \in \mathcal{T}^K$ be the finite set of measurement times. By Definition 5.1 we say $\{t_1, \cdots, t_K\} \times \{\omega_1, \cdots, \omega_d\}$ is a set of parameters giving the measurements. Then, for given $\mathbf{a} \in \mathcal{B} \subset \mathcal{A} \subset \mathbb{R}^d$, by (5.0.1)-(5.0.3) the sensitivity matrix $\mathcal{F}'$ with respect to the set of parameters is

$$\mathcal{F}'(\hat{t}, \hat{\omega})(\mathbf{a}) := \nabla H, \tag{5.4.2}$$

where $\hat{\omega} := (\omega_1, \omega_2, \cdots, \omega_N)$ and H is given by (5.0.1).

For $\ell = 1, 2$, let $\hat{t}_\ell \in \mathcal{T}^{K_\ell}$, $\hat{\omega}_\ell = (\omega_\ell, \cdots, \omega_{N_\ell})$ and denote $\mathcal{F}'_\ell := \mathcal{F}'(\hat{t}_\ell, \hat{\omega}_\ell)$ be sensitivity matrix with $N_\ell K_\ell$ rows and d columns. Then we introduce the condition

$$\mathcal{F}_1'^{*}\mathcal{F}_1' \geq \mathcal{F}_2'^{*}\mathcal{F}_2' \tag{5.4.3}$$

to say the set of parameters in $\mathcal{F}_1'$ is better than the one in $\mathcal{F}_2'$. For instance, letting the measured time be t_{peak}, we suppose the set of S-D pairs in $\mathcal{F}_1'$ be {S4-D4, S5-D5, S6-D6, S7-D7, S8-D8, S9-D9, S10-D10} shown in Figure 5.1, (a), which are not symmetrical about the cuboidal target. Further we suppose the set of S-D pairs in $\mathcal{F}_2'$ be symmetrical about the cuboidal target but having the same x_1-axis with the one in $\mathcal{F}_1'$. By the SVD test we have that $\mathcal{F}_1'^{*}\mathcal{F}_1' - \mathcal{F}_2'^{*}\mathcal{F}_2$ is positive defined, which means that the condition (5.4.3) is valid. In fact, the symmetrical S-D pairs provide similar information. Hence the set of parameters in $\mathcal{F}_1'$ is better than the one in $\mathcal{F}_2'$.

5.5 Chapter Summary

We considered the local analysis of the cuboid approximation including local solvability and its Lipschitz stability. We also gave a clear framework to our whole argument and useful concepts, conditions which can orient numerical study and interpret the numerical results in following Chapter 6. For example the condition for the convergence of LM algorithm and sensitivity analysis. Concerning the theoretical study of determinant condition, it should be remarked that the numerical verification of this condition suggests the following. If we look at the second term of the asymptotic expansions for $\frac{\partial\widetilde{u}_m}{\partial a_3}$, $\frac{\partial\widetilde{u}_m}{\partial b_3}$ and $\frac{\partial\widetilde{u}_m}{\partial P}$, we may be able to prove the determinant condition theoretically.

Chapter 6

Inversion Strategy and Numerical Inversions Using Simulation Data

In this chapter, based on the discussions given before, we propose an inversion strategy providing an initial guess $\mathbf{a}_0$ in section 6.1, which can guarantee successful recovery and accelerate the speed of convergence of LM iteration scheme. Then we verify the effectiveness of our proposed strategy by numerical inversion using simulated data in section 6.2 and experimental data in Chapter 7.

6.1 Step-wise Inversion Strategy

Our inversion strategy consists of the following three steps:

- **Step 1.** (prior estimation)
  By comparing the emission intensity $\mathbf{I}(\omega)$ defined by (4.3.1) for each S-D pair, we first look for Γ on $\partial\Omega$. Here Γ denotes the projection of the unknown target to $\partial\Omega$.

- **Step 2.** (fitting by cube)
  Let $X = (X_1, X_2, X_3)$ and L denote the center and side length of cube $\mathbf{a}^{\text{cube}}$, respectively. We expect that this cube could be an approximation of the unknown target. Then $\mathbf{a}^{\text{cube}}$ can be described by

  $$\mathbf{a}^{\text{cube}} = (X_1, X_2, X_3, L, Q), \tag{6.1.1}$$

  where $Q > 0$ is the unknown absorption coefficient. Choose the initial guess for X_1, X_2 inside Γ and variate X_1, X_2, X_3, L, Q to fit to the measurement by LM iteration scheme. Then we will get a cube

  $$\mathbf{a}^{\text{cube}}_{\text{rec}} = (X_1^*, X_2^*, X_3^*, L^*, Q^*) \tag{6.1.2}$$

  which gives some good fit to the measurement. The number of iteration used in this scheme will be refered by J with $0 < J \leq J_{max}$.

- **Step 3.** (cuboid approximation)
  Let the recovered cube (6.1.2) in Step 2 be the initial guess $\mathbf{a}_0^{\text{cuboid}}$ in this step, that is

  $$\mathbf{a}_0^{\text{cuboid}} = (X_1^* - \frac{L^*}{2}, X_1^* - \frac{L^*}{2}, X_2^* - \frac{L^*}{2}, X_2^* + \frac{L^*}{2}, X_3^* - \frac{L^*}{2}, X_3^* + \frac{L^*}{2}, Q^*). \tag{6.1.3}$$

  Then by further applying LM iteration scheme again, we numerically recover a cuboid

  $$\mathbf{a}^{\text{cuboid}}_{\text{rec}} = (a_1^*, b_1^*, a_2^*, b_2^*, a_3^*, b_3^*, P^*). \tag{6.1.4}$$

We will refer by N with $0 < N \leq N_{max}$ the number of iteration used in this scheme.

Step 1 provides prior information to set the initial guess for Step 2. The advantages of cube used in Step 2 are that it can be described by just using five parameters and these may not heavily depend on the initial guess. We expect that recovered cube can refine the initial guess obtained in Step 1 so that it can be effectively used as the initial guess in the next step. Using the recovered cube in Step 2 as an initial guess, Step 3 is to recover the cuboid, which will give us the approximate geometric information such as position and size of unknown target. Thus, step by step, we expect to obtain a stable inversion and accelerate the convergence speed.

6.2 Numerical Inversion Using Simulation Data

We will verify our inversion strategy with three steps is essential and effective in detail for the zero-lifetime case ($\tau = 0$). Since the emission light for any fixed $\tau > 0$ is just the convolution of some target-independent function with zero-lifetime emission light $\widetilde{u}_m$, such a numerical verification can also reveal the effectiveness of our inversion strategy for the cases of $\tau > 0$. To be precise we will test two examples. For those, if not specified, we always take the physical parameters as $c = 0.219$ mm/ps, $\mu_s' = 1.0\ \mathrm{mm}^{-1}$, $\mu_a = 0.01\ \mathrm{mm}^{-1}$, $\beta = 0.5493\ \mathrm{mm}^{-1}$, and we will set $\gamma = 1$.

Example 6.1. (ellipsoidal target) *Suppose an ellipsoidal fluorescence target is set at* $(0, 0, 11)$ *and the target is assigned the absorption of light by fluorphore with* $\mu_f = P = 0.02\ \mathrm{mm}^{-1}$ *inside the ellipsoid defined by*

$$E := \left\{(x_1 - x_1^*)^2/A^2 + (x_2 - x_2^*)^2/B^2 + (x_3 - x_3^*)^2/C^2 \leq 1\right\}, \tag{6.2.1}$$

where $A = C = 1.5$ *mm,* $B = 3$ *mm and* $x^* = (x_1^*, x_2^*, x_3^*) = (0, 0, 11)$ *is the center of* E.

Example 6.2. (cylindrical target) *Suppose a cylindrical fluorescence target is set at* $(0, 0, 10)$ *and the target is assigned the absorption of light by fluorphore with* $\mu_f = P = 0.02\ \mathrm{mm}^{-1}$ *inside the cylinder defined by*

$$\tilde{E} := \left\{x \in \Omega : |x_1 - x_1^*| \leq A,\ (x_2 - x_2^*)^2 + (x_3 - x_3^*)^2 \leq R^2\right\}, \tag{6.2.2}$$

where $A = 4$ *mm,* $R = 1$ *mm and* $x^* = (x_1^*, x_2^*, x_3^*) = (0, 0, 10)$ *is the center of* $\tilde{E}$.

6.2.1 Good sets of measurements

For ellipsoidal target, we calculate the photon density of emission light by

$$\widetilde{u}_m^{\mathrm{ellipsoid}} = \gamma PABCD \int_0^t \mathrm{d}s \int_0^R r^2\,\mathrm{d}r \int_0^\pi \sin\varphi\,\mathrm{d}\varphi \int_0^{2\pi} K(x_d, y; t-s) K(y, x_s; s)\,\mathrm{d}\theta, \tag{6.2.3}$$

where $P = 0.02\ \mathrm{mm}^{-1}$ and $y = x^* + r(A\sin\varphi\cos\theta, B\sin\varphi\sin\theta, C\cos\varphi)$. For cylindrical target, its photon density of emission light is calculated by

$$\widetilde{u}_m^{\mathrm{cylinder}} = \gamma PD \int_0^t \mathrm{d}s \int_0^R r\,\mathrm{d}r \int_0^{2\pi} \mathrm{d}\theta \int_{-A}^{A} K(x_d, y; t-s) K(y, x_s; s)\,\mathrm{d}\varphi, \tag{6.2.4}$$

where $P = 0.02\ \mathrm{mm}^{-1}$ and $y = x^* + (\varphi, r\cos\theta, r\sin\theta)$.

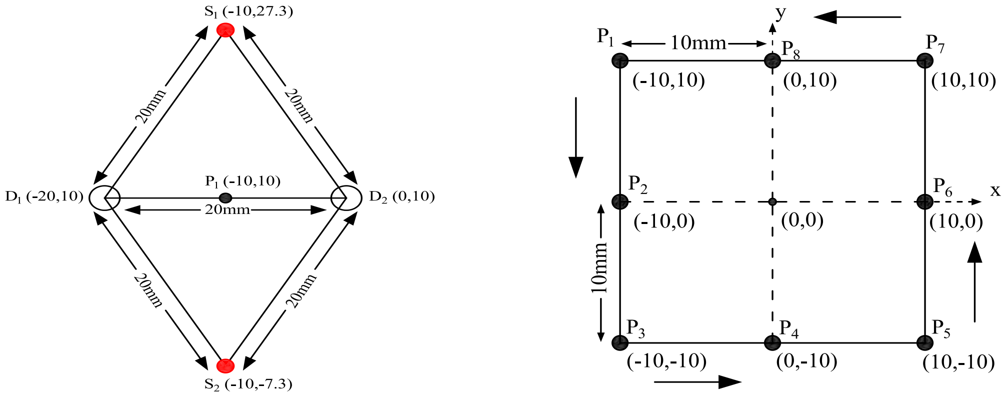

FIGURE 6.1: (Left) The holder of source-detector pairs at a position P_1; (Right) All positions on the boundary surface.

To obtain more data we scan over $\partial\Omega$ and measure several discrete points by moving the holder. This measurement done at each place is called the scan step. The holder has two sources and two detectors. We move this holder without any rotation starting from having its center at P_1 and then moving it to P_2, $P_3, \cdots, P_8$ successively (see the right figure of Figure 6.1). For example, when the center of the holder is at P_1, we conduct measurements for the four source-detector pairs: $(S_1, D_1), (S_1, D_2), (S_2, D_1), (S_2, D_2)$ as shown in the left figure of Figure 6.1. Hence in this scanning we have 8 scan steps and there is four measurements for four source-detector pairs at each scan step. Therefore we have 32 different S-D pairs denoted by $\hat{\omega}$ in total for this scanning. To be precise about the location of sources and detectors, let $P_i = (x^i_{p1}, x^i_{p2}), i = 1, 2, \cdots, 8$ denote the positions of holder in the scanning. Then when the holder center is at P_i, the corresponding sources and detectors are located at

$$S_1 = (x^i_{p1}, x^i_{p2} + 10\sqrt{3}), \quad S_2 = (x^i_{p1}, x^i_{p2} - 10\sqrt{3}), \tag{6.2.5}$$

and

$$D_1 = (x^i_{p1} - 10, x^i_{p2}), \quad D_2 = (x^i_{p1} + 10, x^i_{p2}). \tag{6.2.6}$$

Now we will explain what we think as good sets of measurements in our study of FDOT. For Example 6.1 and Example 6.2, we use data local in time from the temporal point spread function. That is, for each S-D pair, we select the peak time t_{peak} and choose 20 time points $\hat{t} := [t_{peak} - 10\Delta t, t_{peak} + 9\Delta t]$ with time step Δt, such that the measurement data H is a 640-dimensional vector. The noisy data H^δ of H is described by

$$H^\delta = H(1 + \zeta\epsilon), \tag{6.2.7}$$

where $\epsilon > 0$ is a noise level and ζ is the random standard Gaussian noise.

In the succeeding subsections, we will recover the unknown parameters from noisy data (6.2.7). It was shown that local data types are more robust to noise than global data types, and should provide enhanced information to the inverse problem [56]. Furthermore, it is effective to recover the unknown target with good quality by applying a large number of S-D pairs . Because the noise is random in the measurement data, we think that the above sets of measurements are good enough even if they are symmetrically distributed around the target. Hence we will concern about taking such good sets of measurements for the inversion.

In the sequel, we denote by $\mathbf{a}^{\text{cube}}_{\text{exact}}$ and $\mathbf{a}^{\text{cube}}_{\text{noisy}}$ to distinguish the recovered cube by LM iteration scheme in Step 2 using the exact data and noisy data, respectively. Similarly, we make a distinction by $\mathbf{a}_{\text{exact}}^{\text{cuboid}}$ and $\mathbf{a}_{\text{noisy}}^{\text{cuboid}}$ in Step 3. The fluorescence target which we try to recover may have different shapes and we do not know its exact shape. In our cuboid approximation, we will regard $\mathbf{a}_{\text{exact}}^{\text{cube}}$ and $\mathbf{a}_{\text{exact}}^{\text{cuboid}}$ as the optimal approximation to unknown target in Step 2 and Step 3, respectively. Then, to show the accuracy and stability of the recovery using our strategy, we define the approximate L^2 relative error in recoveries by

$$Err := \left\|\mathbf{a}_{\text{exact}}^{\text{cube}} - \mathbf{a}_{\text{noisy}}^{\text{cube}}\right\|_2 \Big/ \left\|\mathbf{a}_{\text{exact}}^{\text{cube}}\right\|_2 \tag{6.2.8}$$

and the approximate L^2 relative error in measurement data by

$$err := \left\|F(\hat{t},\hat{\omega})(\mathbf{a}_{\text{noisy}}^{\text{cube}}) - H^\delta\right\|_2 \Big/ \left\|H^\delta\right\|_2, \tag{6.2.9}$$

where $F(\hat{t},\hat{\omega})(\mathbf{a}_{\text{noisy}}^{\text{cube}})$ is defined by (5.0.3). In parallel, we do the similar definitions for $\mathbf{a}_{\text{exact}}^{\text{cuboid}}$ and $\mathbf{a}_{\text{noisy}}^{\text{cuboid}}$.

Now we are ready to apply our proposed inversion strategy to give our recovery. We will apply the LM algorithm implemented on Matlab. An local minimum can be found as long as arrived at the given number of maximum iterations $J_{max} = N_{max} = 800$, or the length of the calculated step less than 1×10^{-20}, or the reduction of sum of squares of residual fall below the prescribed convergent precision 1×10^{-6}. Further all the computations are performed on a Windows PC or Mac PC.

6.2.2 Results of inversion for ellipsoidal target

In this example we focus on the robustness of our strategy against the initial guesses and the effectiveness of accelerating the convergence speed.

Step 1: We first compare the intensities of zero-lifetime emissions given as (4.3.1) with $T = 3.3$ ns with $\Delta t = 6.67$ ps. The emission intensities of S-D pairs at P_1, P_3, P_5 and P_7 shown in Figure 6.2 are listed in Table 6.1, respectively.

TABLE 6.1: The emission intensities ($\times 10^{-8}$) with different S-D pairs in Ex. 6.1.

P1(-10,10)	P3(-10,-10)	P5(10,-10)	P7(10,10)
S1-D1: 0.100	S1-D1: 3.900	S1-D1: 58.84	S1-D1: 1.610
S1-D2: 1.610	S1-D2: 58.84	S1-D2: 3.900	S1-D2: 0.100
S2-D1: 3.900	S2-D1: 0.100	S2-D1: 1.610	S2-D1: 58.84
S2-D2: 58.84	S2-D2: 1.610	S2-D2: 0.100	S2-D2: 3.900

By the results shown in Figure 4.5 in section 4.3, the emission intensity for S-D pairs near by the target are stronger than the others. From Table 6.1, we can see that the pairs S2-D2, S5-S6, S9-D9 and S14-D13 have the strongest emission intensities. These lead us to a very natural speculation. That is the projection of the center of ellipsoidal target to $\partial\Omega$ should be located in Part 4, Part 1, Part 2 and Part 3 which correspond to the positions of holder at P1, P3, P5 and P7. In fact this is true for Figure 6.2. Thus we speculate that the projection of the center of target to $\partial\Omega$ should be located inside the domain

$$\Gamma := (-10, 10) \times (-10, 10) \subset \partial\Omega, \tag{6.2.10}$$

which is shown in Figure 6.3. In the following inversion, we will use this Γ as a prior information of unknown target, which will be important for the choice of initial guess in

Step 2. Here we note that we only compared the emission intensities with respect to the holder at P1, P3, P5 and P7 which distribute around the edge of tissue surface to obtain the domain Γ. Actually we can further narrow Γ by comparing emission intensities if we have enough scan steps at the boundary surface of tissue.

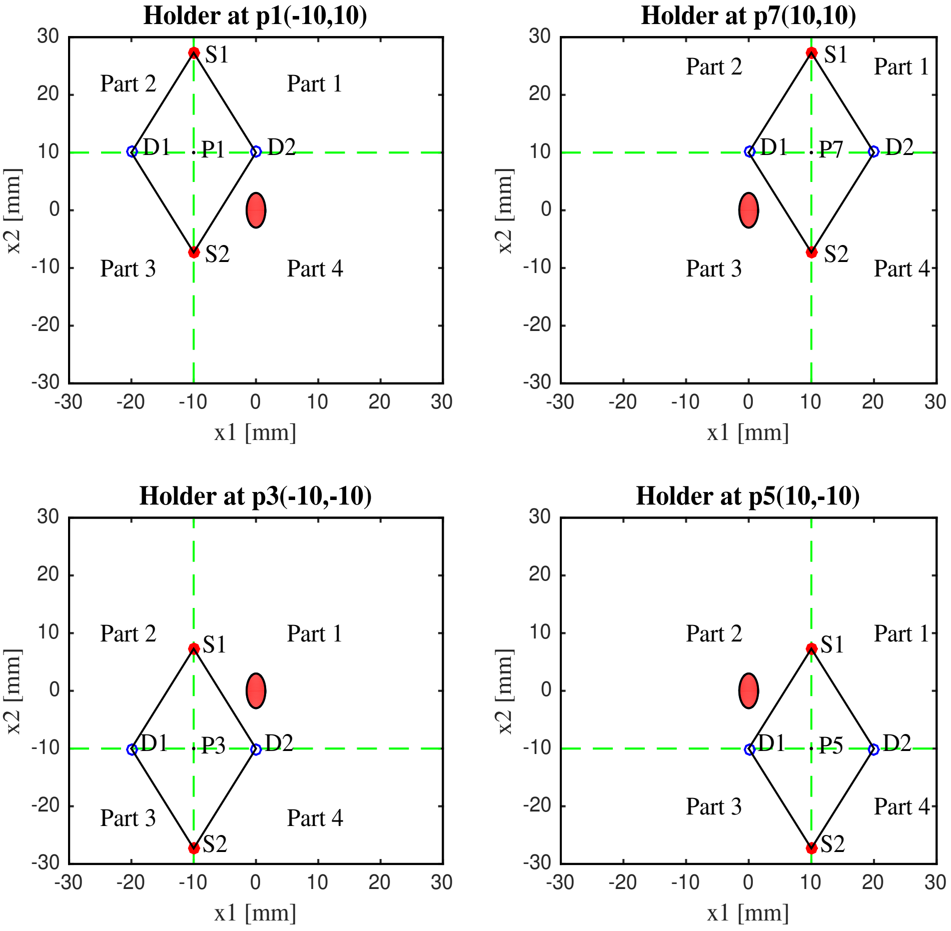
Holder at p1(-10,10)
Holder at p7(10,10)
Holder at p3(-10,-10)
Holder at p5(10,-10)
Part 1
Part 2
Part 3
Part 4
S1
S2
D1
D2
P1
P7
P3
P5
x1 [mm]
x2 [mm]
-30
-20
-10
0
10
20
30

FIGURE 6.2: The S-D pairs corresponding to the positions of holder at P1, P3, P5 and P7 in Ex.6.1, respectively.

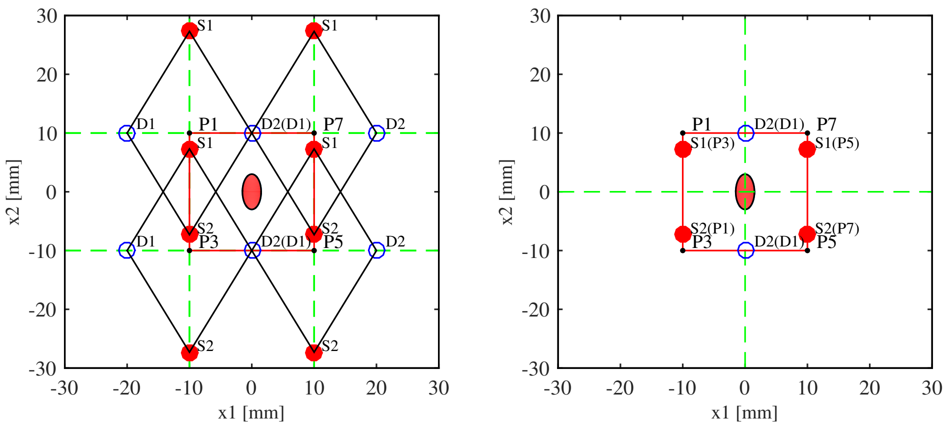
S1
S2
D1
D2
D2(D1)
P1
P7
P3
P5
S1(P3)
S1(P5)
S2(P1)
S2(P7)
x1 [mm]
x2 [mm]
-30
-20
-10
0
10
20
30

FIGURE 6.3: The prior information Γ on the boundary ∂Ω in Ex.6.1.

Step 2: By Γ we set a bound for initial value $\mathbf{a}_0^{\text{cube}} = (X_1^0, X_2^0, X_3^0, L_0, Q_0)$ by

$$(X_1^0, X_2^0) \in \Gamma,\ 0 < X_3^0 < 30,\ 0 < L_0 < \min\{20, 2X_3^0\},\ 0 < Q_0 < 10, \tag{6.2.11}$$

where the bound for X_3^0, L_0 and Q_0 are not precise. Now we apply the LM iteration scheme to fit this $\mathbf{a}^{\text{cube}}$ to the measurement.

By arbitrarily setting the initial guess from the bound (6.2.11), we have

$$\mathbf{a}_{\text{exact}}^{\text{cube}} = (0, 0, 11.24, 4.089, 0.0086)$$

with $err = 3.60e-3$. Using the same measurement with noise level $\epsilon = 5\%$, the recovered results obtained in a similar way with different initial guesses are listed in Table 6.2.

Table 6.2: Recoveries using different initial guesses in Step 2 for Ex. 6.1 ($\epsilon = 5\%$).

$\mathbf{a}_0^{\text{cube}}$	$\mathbf{a}_{\text{noisy}}^{\text{cube}}$	Err	err	J
$(-8, -8, 4, 4, 0.1)$	$(-0.02, 0.01, 11.18, 3.78, 0.011)$	$2.6e-2$	$5.2e-3$	39
$(-15, -15, 4, 4, 0.1)$	$(-0.02, 0.01, 11.18, 3.78, 0.011)$	$2.6e-2$	$5.2e-3$	171
$(-8, -8, 16, 8, 10)$	$(-0.02, 0.01, 11.18, 3.78, 0.011)$	$2.6e-2$	$5.2e-3$	89
$(-15, -15, 16, 8, 10)$	$(-0.02, 0.01, 11.18, 3.78, 0.011)$	$2.6e-2$	$5.2e-3$	189

From Table 6.2, it can be observed that the recovered results (Step 2) do not heavily depend on the initial guesses. Under the same noisy measurement, the inversions from different initial guesses are similar. It means that Step 2 enhanced the robustness of LM algorithm against different initial guesses for noise even if the initial guess of the target is chosen very far away with the target. However, it can be also seen that the choice of initial guess has a strong impact on the iteration number J. For instance, letting $X_3^0 = 4$, $L_0 = 4$ and $Q_0 = 0.1$ are fixed, the iteration number is $J = 39$ for the case $(X_1^0, X_2^0) = (-8, -8) \in \Gamma$ but $J = 171$ for the case $(X_1^0, X_2^0) = (-15, -15) \notin \Gamma$. It means that choosing initial guess $(X_1^0, X_2^0) \in \Gamma$ is effective to save iteration number.

Now we fix the initial guess as

$$\mathbf{a}_0^{\text{cube}} = (-8, -8, 4, 4, 0.1), \tag{6.2.12}$$

which belongs to the bound given by (6.2.11). Since noisy data has random noise, we perform the inversion 10-times from different noisy data to test the numerical stability of recovery. We will denote by $\bar{\mathbf{a}}_{\text{noisy}}^{\text{cube}}$ the average of the results obtained by doing the inversion 10-times. Then Table 6.3 lists $\bar{\mathbf{a}}_{\text{noisy}}^{\text{cube}}$ corresponding to different noise levels, where $\bar{E}rr$ is the average relative error of recovery, $\bar{e}rr$ is the average relative error in measurement data and J_{avr} is the average iteration number. Furthermore, the 10-time recoveries are plotted in Figure 6.4, and Figure 6.5 shows the average recovery for the case the noise level is $\epsilon = 5\%$.

Table 6.3: The average recoveries with different noise level ϵ in Step 2 for Ex. 6.1.

ϵ	$\bar{\mathbf{a}}_{\text{noisy}}^{\text{cube}}$	$\bar{E}rr$	$\bar{e}rr$	J_{avr}
5%	$(0.0004, 0.0067, 11.20, 3.751, 0.0125)$	$2.85e-2$	$1.19e-2$	41.8
1%	$(0.0001, 0.0014, 11.23, 4.032, 0.0090)$	$4.80e-3$	$3.70e-3$	37.4

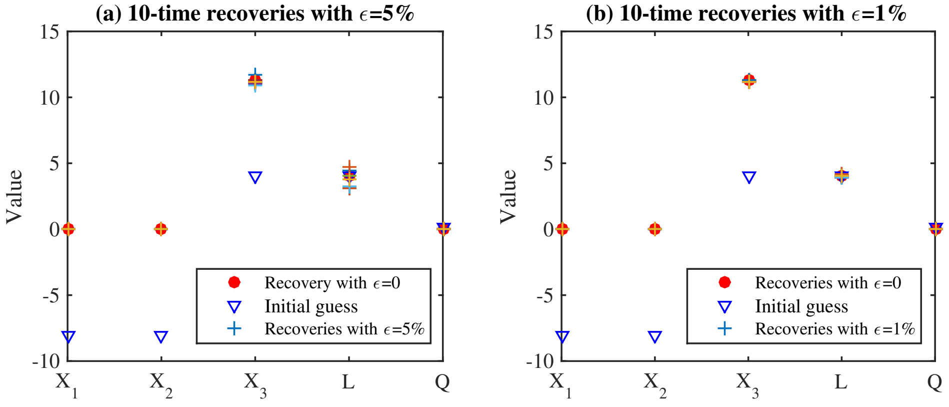

FIGURE 6.4: The 10-times recoveries with different noise levels.

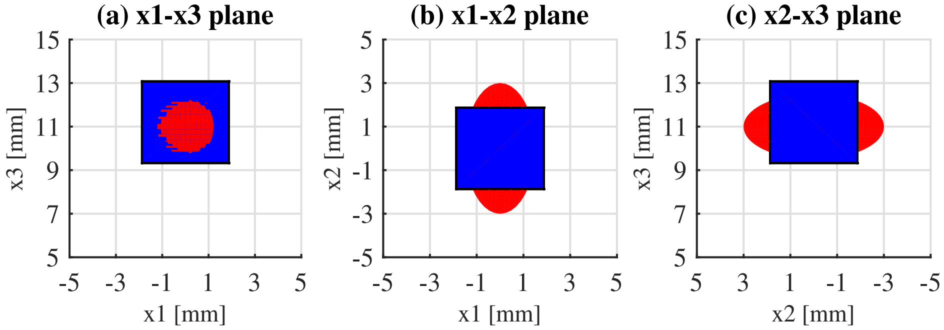

FIGURE 6.5: The different views of exact ellipsoidal target (red) and average recovered cube (blue) ($\epsilon = 5\%$).

From Table 6.3, it can be seen that fitting by cube is numerical stable against the noise in measurement data. We can stably recover even if the noise level is $\epsilon = 5\%$. This step only needs a small number of iteration. Based on the results we have obtained so far in Step 2, we can say that the results of this step do not heavily depend on the initial guess or robust against different initial guesses, but the convergence speed becomes faster if we choose an initial guess with $(X_1^0, X_2^0) \in \Gamma$. Thus, to find Γ in Step 1 is very important.

Step 3: We first discuss about the necessity of fitting by cube (Step 2) for cuboid approximation (Step 3). To this end, we mainly answer the following two questions:

(i) How would be if we just use $\mathbf{a}_0^{\text{cube}}$ as initial guess in Step 3 ?

(ii) How would be the difference in the recoveries between with and without Step 2 ?

Concerning the questions (i) and (ii), we considered the recoveries from exact measurement data with two different initial guesses. One is the initial cube $\mathbf{a}_0^{\text{cube}}$ given by (6.2.12) which is also used as the initial guess in Step 2. The other is the recovered cube $\mathbf{a}_{\text{noisy}}^{\text{cube}}$ which is recovered from (6.2.12) in Step 2. The recovered results are listed in Table 6.4.

TABLE 6.4: Recoveries from exact measured data in Step 3 for Ex.6.1 ($\epsilon = 0$).

$\mathbf{a}_0^{\text{cuboid}}$	$\mathbf{a}_{\text{exact}}^{\text{cuboid}}$	err	N
$\mathbf{a}_0^{\text{cube}}$	$(-1.165, 1.165, -2.321, 2.321, 9.813, 12.20, 0.022)$	$1.62e-5$	468
$\mathbf{a}_{\text{exact}}^{\text{cube}}$	$(-1.165, 1.165, -2.321, 2.321, 9.813, 12.20, 0.022)$	$1.62e-5$	243

Similar recoveries as above for fixed noise level $\epsilon = 5\%$ are listed in Table 6.5. Further the recovered cuboid is plotted in Figure 6.6.

TABLE 6.5: Recoveries from noisy measured data in Step 3 for Ex. 6.1 ($\epsilon = 5\%$).

$\mathbf{a}_0^{\text{cuboid}}$	$\mathbf{a}_{\text{noisy}}^{\text{cuboid}}$	Err	err	N
$\mathbf{a}_0^{\text{cube}}$	$(-1.07, 1.04, -2.15, 2.17, 9.91, 12.02, 0.029)$	$2.15e-2$	$3.80e-3$	528
$\mathbf{a}_{\text{noisy}}^{\text{cube}}$	$(-1.07, 1.04, -2.15, 2.17, 9.91, 12.02, 0.029)$	$2.15e-2$	$3.80e-3$	297

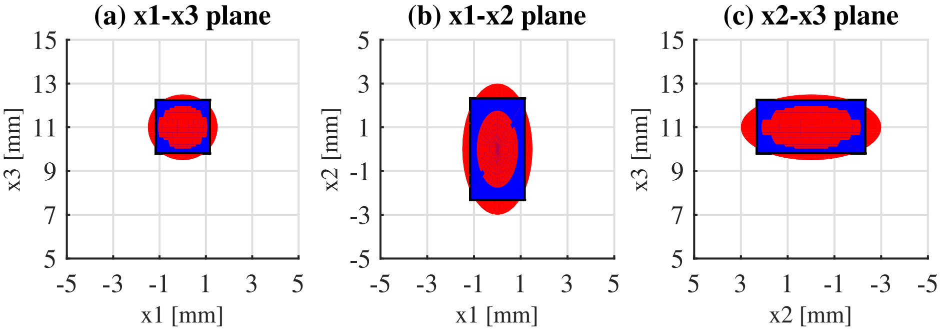

FIGURE 6.6: The different views of exact ellipsoidal target (red) and recovered cuboid (blue) in Ex.1 ($\epsilon = 5\%$). (a) Front view; (b) Vertical view; (c) Side view.

We also carried out 100-time recoveries from different measured data with noise level $\epsilon = 1\%$. The mean and variance of 100-time recoveries for different parameters are listed in Table 6.6, respectively.

TABLE 6.6: The 100-time recoveries from different noisy data sets with $\epsilon = 1\%$ for Ex.6.1.

Index	a_1^*	b_1^*	a_2^*	b_2^*	a_3^*	b_3^*	P^*
$\mathbf{a}_{\text{exact}}^{\text{cuboid}}$	-1.165	1.165	-2.321	2.321	9.813	12.20	0.022
Mean	-1.160	1.160	-2.310	2.310	9.855	12.17	0.036
Variance	0.018	0.018	0.020	0.020	0.085	0.233	$4.10e-3$

Table 6.2 in Step 2 showed that the iteration number J of Step 2 from $\mathbf{a}_0^{\text{cube}}$ to $\mathbf{a}_{\text{noisy}}^{\text{cube}}$ is $J = 39$. Now Table 6.4 and Table 6.5 show that the convergence speed using recovered cube $\mathbf{a}_{\text{noisy}}^{\text{cube}}$ in Step 2 as initial guess becomes faster both for exact and noisy measured data. All the above recoveries show that our inversion strategy with three steps $\Gamma \mapsto \mathbf{a}_{\text{noisy}}^{\text{cube}} \mapsto \mathbf{a}_{\text{noisy}}^{\text{cuboid}}$ is a stable and effective strategy. The recovered cuboid approximately recover the position, shape and size of the unknown ellipsoidal target.

From Table 6.6, it can be observed that the mean of 100-time recoveries are approximately equal to the values of $\mathbf{a}_{\text{exact}}^{\text{cuboid}}$. This means that the recoveries are numerically stable. We remark here that the variance for a_3^* and b_3^* are clearly bigger than those of other parameters, which shows the difficulty to recover the parameters a_3^*, b_3^* and this is consistent to what we observed in the sensitivity analysis given in subsection 5.4. That implies the recovery of thickness of the target should be unstable against the noise for some sets of measurement data. To be precise, we explain more in the following.

We further compare the stability of recovery of the width, length and thickness. First, let L_{width}^j, L_{length}^j and $L_{\text{thickness}}^j$ be the recovered width, length and thickness corresponding to the j-th recovery of the 100-time recoveries and plot its values in Figure 6.7, (a), (b), (c), respectively. Note that $L_{\text{width}}^{\text{mean}} = 2.320$ mm, $L_{\text{length}}^{\text{mean}} = 4.620$ mm and $L_{\text{thickness}}^{\text{mean}} = 2.315$

mm which are the mean of the 100-time recoveries, respectively. Next, we define the relative errors at each recovery by

$$\frac{|L^j_{\text{width}} - L^{\text{mean}}_{\text{width}}|}{|L^{\text{mean}}_{\text{width}}|}, \ \frac{|L^j_{\text{length}} - L^{\text{mean}}_{\text{length}}|}{|L^{\text{mean}}_{\text{length}}|}, \ \frac{|L^j_{\text{thickness}} - L^{\text{mean}}_{\text{thickness}}|}{|L^{\text{mean}}_{\text{thickness}}|}, \quad j = 1, 2, \cdots, 100$$

and plot its values in Figure 6.8, (a), (b), (c), respectively. From Figure 6.7 and Figure 6.8, it can be observed that the recovery of thickness should be more difficult than the recovery of width and length.

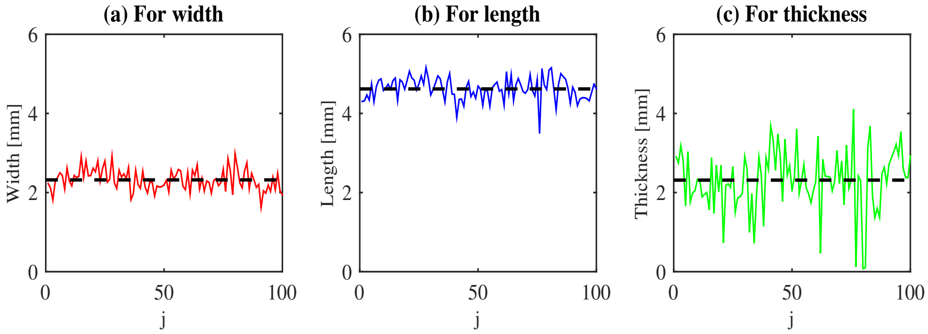

FIGURE 6.7: The recovered width, length and thickness at each recovery of the 100-time recoveries. The black lines are the corresponding mean of the 100-time recoveries.

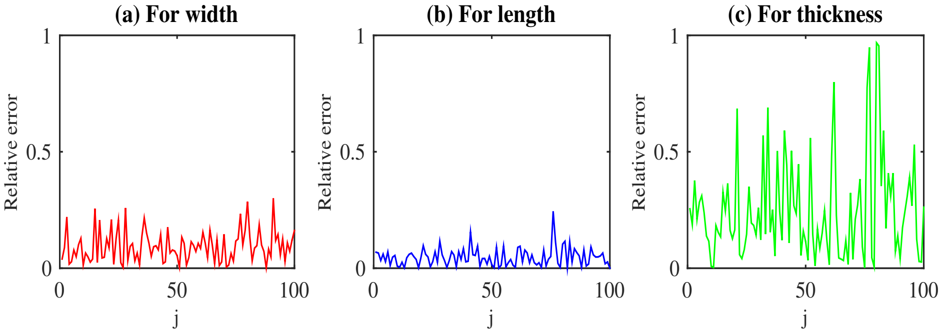

FIGURE 6.8: The relative error for width, length and thickness at each recovery of the 100-time recoveries.

We will give one remark before closing this subsection.

Remark 6.1. *The volume of unknown ellipsoidal target is* $V_{\text{ellipsoid}} = \frac{4\pi}{3}ABC \approx 28.27$ mm^3*, and the absorption coefficient is* $P_{\text{ellipsoid}} = 0.02$ mm^{-1}*. Let* V^j_{rec} *and* P^j_{rec} *be the volume and absorption coefficient corresponding to the j-th recovery of the 100-times recoveries in Table 6.6. Then Table 6.6 shows that*

$$V^j_{\text{rec}} \approx V_{\text{ellipsoid}}, \ P^j_{\text{rec}} \approx P_{\text{ellipsoid}}, \ V^j_{\text{rec}} \times P^j_{\text{rec}} \approx V_{\text{ellipsoid}} \times P_{\text{ellipsoid}}, \quad j = 1, \cdots, 100.$$

6.2.3 Results of inversion for cylindrical target

In this example we focus on the error analysis by cuboid approximation. By comparing the emission intensity with $T = 4$ ns and $\Delta t = 6.1$ ps for different S-D pairs we can also obtain $\Gamma := (-10, 10) \times (-10, 10) \subset \partial\Omega$. Setting the initial cube $\mathbf{a}^{\text{cube}}_0 = (-8, -8, 4, 4, 0.1)$, we have $\mathbf{a}^{\text{cube}}_{\text{exact}} = (0, 0, 10.58, 2.26, 0.05)$ with the approximate L^2 relative error in measurement data $err = 2.46e - 2$. Next, using the same measurement with noise level

$\epsilon = 5\%$, the recovered result obtained in a similar way with same initial guess is

$$\mathbf{a}_{\text{noisy}}^{\text{cube}} = (0.007, -0.032, 10.68, 3.92, 0.01) \tag{6.2.13}$$

with $err = 5.84e-2$. Setting the recovered cube from Step 2 as the initial guess, the recovered cuboid using noisy measurement data with different noise levels ε are listed in Table 6.7, respectively.

TABLE 6.7: Recoveries from noisy measured data in Step 3 for Ex.6.2

ϵ	$\mathbf{a}_{\text{noisy}}^{\text{cuboid}}$	err	Err
0	$(-4.001, 4.001, -0.87, 0.87, 9.13, 10.86, 0.0209)$	$1.69e-6$	
1%	$(-3.999, 3.991, -0.77, 0.78, 9.15, 10.84, 0.0240)$	$1.02e-2$	$9.00e-3$
5%	$(-3.878, 3.864, -1.03, 0.95, 9.60, 10.58, 0.0348)$	$5.14e-2$	$3.03e-2$

We note the center, length and radius of the cylindrical target are (0,0,10), 8 and 1, respectively. Table 6.7 shows that the position and size of cylindrical target can be approximated well by the recovered cuboid. We can see that the values of err defined by (6.2.9) are approximately equal to its corresponding noise levels ϵ, i.e.,

$$err := \frac{\left\| F(\hat{t}, \hat{\omega})(\mathbf{a}_{\text{noisy}}^{\text{cuboid}}) - H^\delta \right\|_2}{\|H^\delta\|_2} \approx \epsilon \approx \frac{\|H - H^\delta\|_2}{\|H^\delta\|_2}$$

due to the description of noisy data H^δ given by (6.2.7), implying the interpretation of measurement data using cuboid was reasonable and $\mathbf{a}_{\text{noisy}}^{\text{cuboid}} \to \mathbf{a}_{\text{exact}}^{\text{cuboid}}$ as $\epsilon \to 0$.

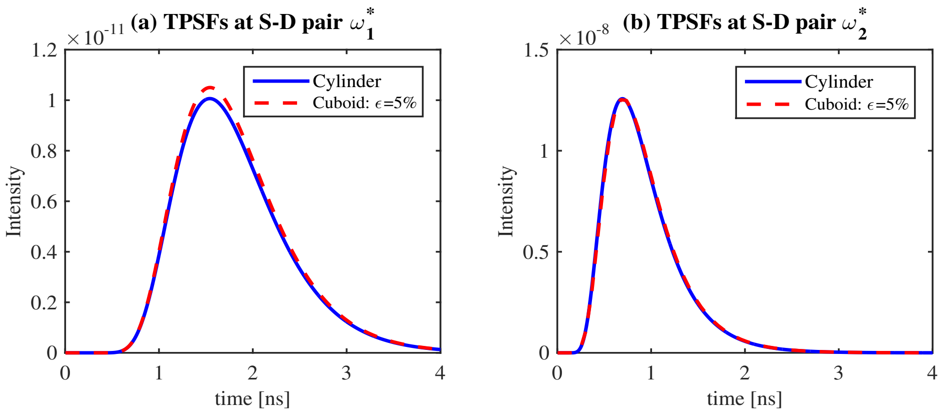

FIGURE 6.9: The TPSFs $\widetilde{u}_m^{\text{cylinder}}(t, \omega)$ (blue line) and $\widetilde{u}_m(\mathbf{a}_{\text{noisy}}^{\text{cuboid}})(t, \omega)$ (red line) to two S-D pairs. Here $\mathbf{a}_{\text{noisy}}^{\text{cuboid}}$ was recovered by the noisy data with $\epsilon = 5\%$.

The error of our method using cuboid approximation consists of two kinds of error: system error and measure error. The former comes from the different shape between cylindrical target and cuboid, and the latter comes from the noise added in the exact measurement. Indeed, the components of measurement from different S-D pairs contribute different for the recovery. The data with stronger intensity are more stable against the measure noise. In other words, the data provided by the S-D pairs close to the target are very important in the data fitting, which determine the accuracy of inversion. To be precise we plot the temporal point spread functions (TPSFs) $\widetilde{u}_m^{\text{cylinder}}(t, \omega)$ and $\widetilde{u}_m(\mathbf{a}_{\text{noisy}}^{\text{cuboid}})(t, \omega)$ to two different S-D pairs in Figure 6.9. See Figure 6.9, (a) for $\omega_1^* := (x_s, x_d) = ((-10, -10-10\sqrt{3}), (-20, -10))$ and Figure 6.9, (b) for

$\omega_2^* := (x_s, x_d) = ((0, -10 + 10\sqrt{3}), (10, -10))$, respectively. ω_1^* is located far away the target while ω_2^* is close to the target. From Figure 6.9, it can be observed for $\epsilon = 5\%$ that $\widetilde{u}_m(\mathbf{a}_{\text{noisy}}^{\text{cuboid}})(t, \omega)$ to ω_2^* is in very good agreement with $\widetilde{u}_m^{\text{cylinder}}(t, \omega)$ and less accurate to ω_1^*. We also note that the peak time for ω_2^* is quit earlier than the one for ω_1^*. Thus by Step 1 we can also select the S-D pairs with strong emission intensity to reduce the number of measurements to save computation. That is possible according to the argument given in Chapter 5 that a small number of measurements could ensure the local solvability of the inverse problem.

Likewise we did for Example 1, we carried out 100-time recoveries from different measured data with noise level $\epsilon = 1\%$. The mean and variance of 100-time recoveries for different parameters are listed in Table 6.8, respectively.

TABLE 6.8: The 100-time recoveries from different noisy data sets with $\epsilon = 1\%$ for Ex.6.2.

Index	a_1^*	b_1^*	a_2^*	b_2^*	a_3^*	b_3^*	P^*
$\mathbf{a}_{\text{exact}}^{\text{cuboid}}$	-4.001	4.001	-0.87	0.87	9.13	10.86	0.021
Mean	-4.000	3.999	-0.82	0.82	9.17	10.84	0.032
Variance	0.002	0.002	0.099	0.099	0.062	0.138	$4.87e-4$

Table 6.8 shows that the mean of 100-time recoveries are approximately equal to the values of $\mathbf{a}_{\text{exact}}^{\text{cuboid}}$, implying the recoveries are numerically stable. Note that the variance for parameters a_1^* and b_1^* are clearly smaller than those of other parameters, and hence know the recoveries for a_1^* and b_1^* should be more stable against the noise in measurement data. On the other hand, due to the nonlinearity and strong ill-posedness of our FDOT inverse problem, although the listed recovered cuboid $\mathbf{a}_{\text{noisy}}^{\text{cuboid}}$ corresponding to $\epsilon = 5\%$ in Table 6.7 is satisfactory, we point out that the recoveries especially for a_3^* and b_3^* may become less stable if the noise level is large. This difficulty of identifying thickness may further influence the accuracy of other geometric information such as the length (denoted by $b_1^* - a_1^*$) and width (denoted by $b_2^* - a_2^*$) of the recovered cuboid. One may improve the stability of recovery against large noise by increasing the number of S-D pairs and letting the S-D pairs distribute more closely around the target.

6.3 Chapter Summary

By giving up the recovery of the detail shape of the target, we could identify the location of the target by identifying only several unknown parameters. Even for these several parameters, the LM method was not stable or only converged slowly unless good initial guesses were used. Thus the proposed procedure of narrowing target domains as $\Gamma \to \mathbf{a}_0^{\text{cubic}} \to \mathbf{a}_0^{\text{cuboid}}$ is important for the iterative method to work, which was confirmed by the results of inversion using simulated data. Our proposed strategy was fast and robust against the choice of initial guess.

Chapter 7

Numerical Inversions Using Experimental Data

In this section, we further verify the effectiveness of our proposed strategy using experimental data obtained from ex vivo beef phantoms.

7.1 Experimental Demonstration with a Beef Phantom

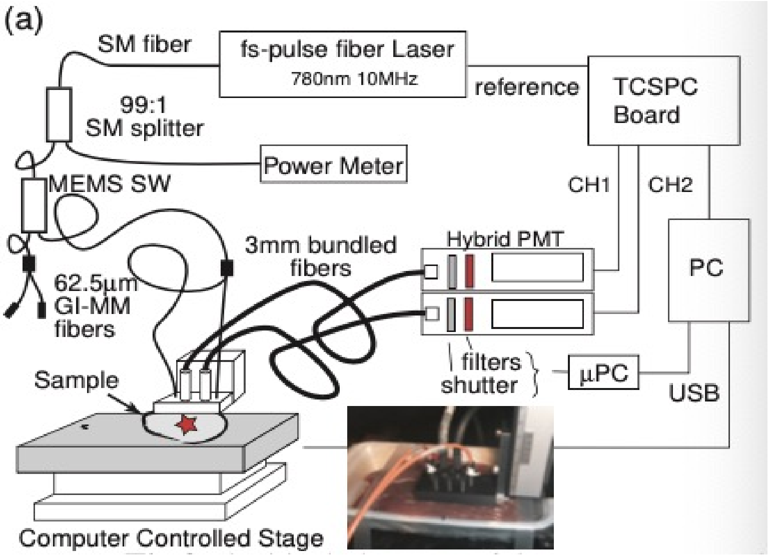
(a)
SM fiber
fs-pulse fiber Laser
780nm 10MHz
reference
TCSPC Board
99:1 SM splitter
Power Meter
MEMS SW
CH1
CH2
3mm bundled fibers
Hybrid PMT
PC
62.5μm GI-MM fibers
Sample
filters
shutter
μPC
USB
Computer Controlled Stage

FIGURE 7.1: The block diagram of the experiment and the geometry of the fibers.

An experiment with a fluorescence target in a beef was conducted to demonstrate our inversion strategy in the medical applications. The beef mimicked human tissue. The experiment was carried out by a picosecond time-domain system as described in our previous paper [62]. Briefly, a picosecond laser at 780 nm with 10 MHz repetition was coupled to an optical fiber. The optical fiber was bifurcated and one branch of them was connected to an extra fiber to get a sufficient delay about 10 ns to separate two excitation pulses in time-domain. The two fibers with a diameter of 62.5 μm excited a fluorescence target implanted in a beef block at different two points. The fluorescence (emission) were collected by two bundled fibers with a diameter of 3 mm and delivered to high-speed hybrid photomultiplier tubes with selectable band pass filters. In this experiment, we selected a filter for the fluorescence wavelength region ($>$ 834 nm) but we also used a filter for the excitation wavelength to measure the IRF and the optical property of meat. The photomultiplier tube was worked in photon counting mode and the timing of the detected photon with respect to the excitation timing was accumulated by a time-correlated single photon counting board to yield the temporal response function of the fluorescence. Two excitation sources were recorded in a same temporal response function at a different time region by the delay. The time step of the temporal response function was 6.1 ps/bin and the time range of the record was about 50 ns and the data was accumulated upto 90 sec. Eventually, temporal profiles at two detection points with two different excitation sources were recorded in two measurement temporal response data. Two temporal profiles with different excitation sources were separated from each measurement temporal response data and the time-axis was calibrated for the analysis.

The IRF (i.e, the function q in (4.1.6)) was measured by a special designed adapter as shown in Figure 7.2, which is basically measuring the scattering of the excitation pulse by a peace of paper at a known distance. The measured temporal response function approximated the IRF of the experimental setup.

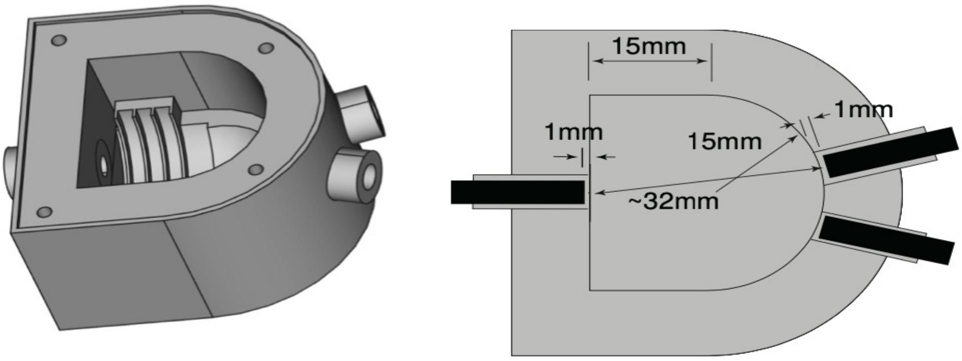

Figure 7.2: The IRF measurement adapter. The adapter holds some attenuation filters and a small diffuser to homogenize the light.

The fluorescence lifetime $\tau = 0.6$ ns was estimated by another experiment [67]. The temporal response function of the background emission was approximated by the function at the lowest emission intensity and the background response was simply subtracted from other measurement data. In following two experiments with a beef meat phantom, the physical parameters determined by another experiment with the excitation light are

$$\tau = 0.6 \text{ ns}, \;\; c = 0.219 \text{ mm/ps}, \;\; \mu_\mathrm{s}' = 0.92 \text{ mm}^{-1}, \;\; \mu_\mathrm{a} = 0.023 \text{ mm}^{-1}, \;\; \beta = 0.50 \text{ mm}^{-1}.$$

We remark that the absolute fluorescence intensity in the experiment is difficult to determine because the intensity is depending on the sensitivity or detectability of the system and the calibration is very difficult. Then, these unknowns are reduced to a proportional constant of μ_f. Therefore, γ can be included in this proportional constant denoted by C_γ. Then, in this section, we consider positive constant $P := C_\gamma \mu_f$ be the unknown absorption coefficient inside approximate cuboid given by (4.1.10). Further, at each iteration in the LM iteration scheme, we will calculate the emission light for $t \in (0, T)$ with $T = 10$ ns by (4.1.7), where the IRF q was convoluted with fluorescence lifetime function shown in (4.1.8).

Now we are ready to apply our proposed inversion strategy to give our recovery.

7.2 Results of Inversion for Beef Experiment I

BEEF EXPERIMENT I: As shown in Figure 7.3, a block meat about $5 \times 10 \times 5$ cm^3 was purchased from a food market and then cut to implant a fluorescence target. The fluorescence target containing a 1 μM indocyanine green (ICG) solution in 1% Intralipid in a small cylinder (2 mm in diameter and 8 mm in length) was implanted at about 16 mm from the measurement surface of the meat sample. Then, the boundary measurements were performed using optical fibers attached to a holder on the top of beef.

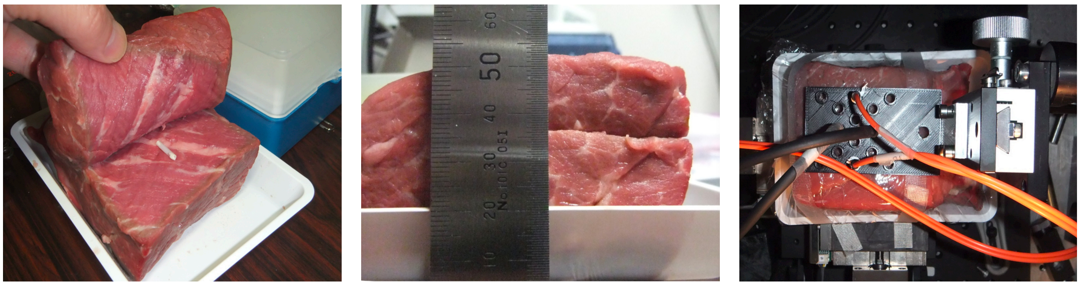

FIGURE 7.3: Beef experiment I: (Left) A cylinder of fluorescence target was placed inside the beef. (Middle) The cylinder was embedded at depth about 16 mm. (Right) Boundary measurements were performed using optical fibers attached to a holder on the top of beef.

The two excitation and two detection fibers were aligned with a fiber holder as shown in the left figure of Figure 6.1. The distance between the excitation and the detection points was fixed to 20 mm in our measurements. Then, the holder was scanned on the meat surface by a motorized stage. We used 16-different fiber holder positions as shown in Figure 7.4, yielding 64-different source-detector (S-D) pairs.

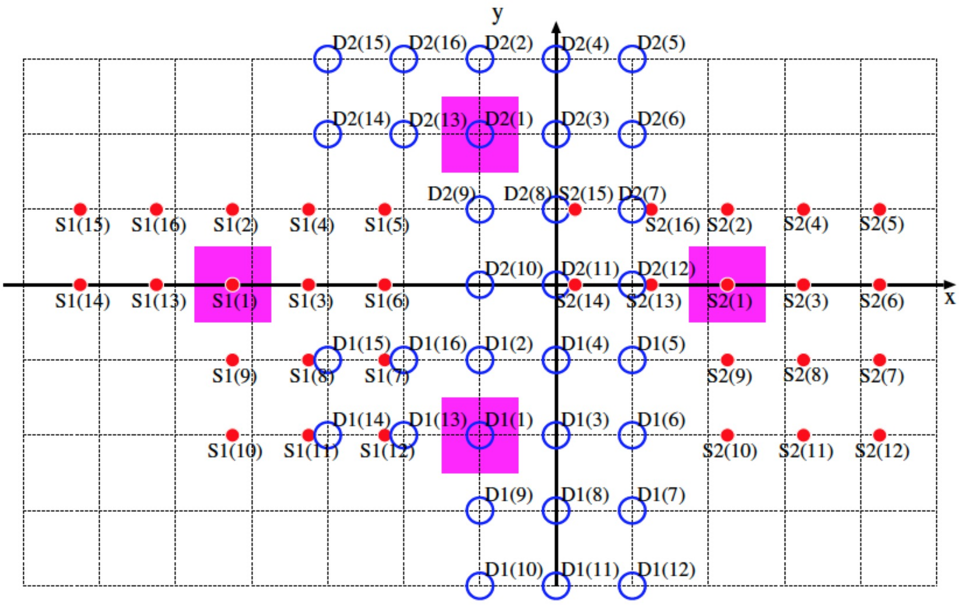
y
D2(15)
D2(16)
D2(2)
D2(4)
D2(5)
D2(14)
D2(13)
D2(1)
D2(3)
D2(6)
D2(9)
D2(8)
S2(15)
D2(7)
S1(15)
S1(16)
S1(2)
S1(4)
S1(5)
S2(16)
S2(2)
S2(4)
S2(5)
D2(10)
D2(11)
D2(12)
S1(14)
S1(13)
S1(1)
S1(3)
S1(6)
S2(14)
S2(13)
S2(1)
S2(3)
S2(6)
x
D1(15)
D1(16)
D1(2)
D1(4)
D1(5)
S1(9)
S1(8)
S1(7)
S2(9)
S2(8)
S2(7)
D1(14)
D1(13)
D1(1)
D1(3)
D1(6)
S1(10)
S1(11)
S1(12)
S2(10)
S2(11)
S2(12)
D1(9)
D1(8)
D1(7)
D1(10)
D1(11)
D1(12)

FIGURE 7.4: The positions of S-D pairs in Beef Experiment I. Red small disks show sources and blue circles show detectors. The sources and detectors for the holder at position P1 (i.e, 1) are distinguished by purple squares.

Step 1: Likewise we did in section 6.2, we can obtain the prior information of unknown target by comparing the emission intensities defined by (4.3.1). For example, we compare the emission intensities with respect to the holder of S-D pairs at P3(0, 0), P4(0, 5), P13(-10, 0) and P16(-10, 5), which are shown in Figure 7.5 and listed in Table 7.1.

TABLE 7.1: The emission intensities ($\times 10^3$ counts) with different S-D pairs.

P3(0,0)	P4(0,5)	P13(-10,0)	P16(-10,5)
S1-D1: 3.0240	S1-D1: 10.118	S1-D1: 0.0950	S1-D1: 0.3490
S1-D2: 33.330	S1-D2: 40.115	S1-D2: 3.0990	S1-D2: 2.5270
S2-D1: 0.7880	S2-D1: 1.5840	S2-D1: 2.2900	S2-D1: 9.0480
S2-D2: 5.6790	S2-D2: 4.7990	S2-D2: 28.976	S2-D2: 33.512

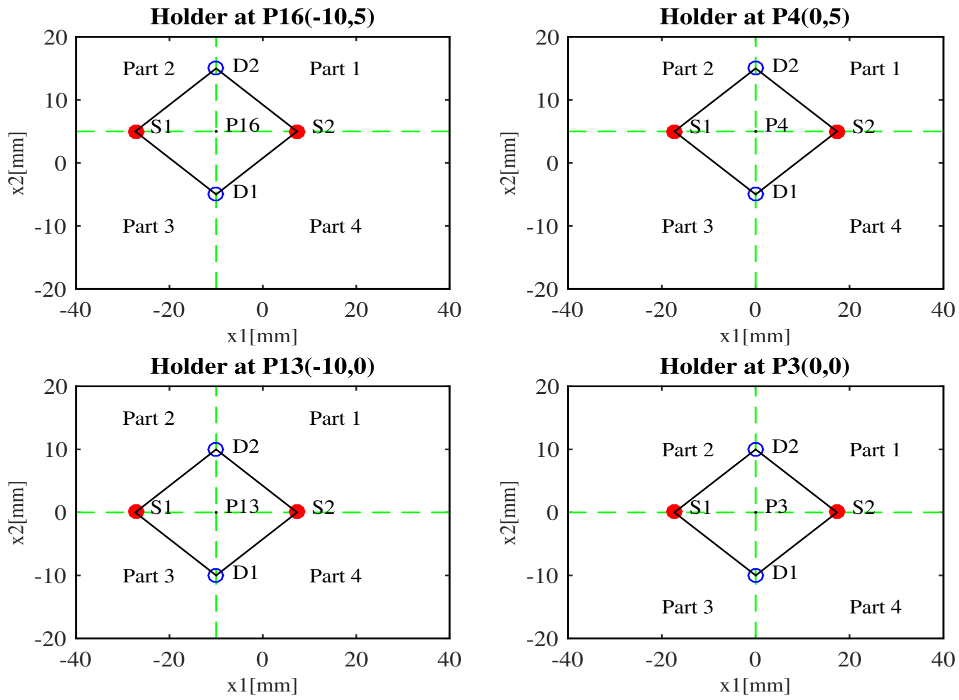

FIGURE 7.5: The positions of holder at P3, P4, P13 and P16 in Experiment I.

From Table 7.1 and Figure 7.5, it can be observed that the emission intensities with S1-D2 pair, S1-D2 pair, S2-D2 pair and S2-D2 pair are stronger than other S-D pairs with respect to the positions of holder at P3, P4, P13 and P16, which means that the projection of the center of unknown approximate cuboid to boundary surface should be located inside

$$\Gamma := (-10, 0) \times (5, 20) \subset \partial\Omega. \tag{7.2.1}$$

By the computation results of emission intensities for each S-D pair, to reduce computation, we perform the inversion using the measured data given by 16 S-D pairs

$$\begin{gathered}
\mathrm{p1} := \mathrm{P01S1D2}, \mathrm{p2} := \mathrm{P01S2D2}, \mathrm{p3} := \mathrm{P02S1D2}, \mathrm{p4} := \mathrm{P02S2D2}, \\
\mathrm{p5} := \mathrm{P03S1D2}, \mathrm{p6} := \mathrm{P04S1D2}, \mathrm{p7} := \mathrm{P05S1D1}, \mathrm{p8} := \mathrm{P05S1D2}, \\
\mathrm{p9} := \mathrm{P06S1D2}, \mathrm{p10} := \mathrm{P07S1D2}, \mathrm{p11} := \mathrm{P08S1D2}, \mathrm{p12} := \mathrm{P13S2D2}, \\
\mathrm{p13} := \mathrm{P14S2D2}, \mathrm{p14} := \mathrm{P15S2D1}, \mathrm{p15} := \mathrm{P15S2D2}, \mathrm{p16} := \mathrm{P16S2D2},
\end{gathered}$$

which have stronger emission intensities than other S-D pairs such that they should be more close to the unknown target. We note here for instance “P01S1D2” denotes the S1-D2 pair corresponding to the position of holder at P1 in Figure 7.4, where the background fluorescence was subtracted from the signal at each S-D pair. Since the emission intensity from the S-D pair at P15S1D2 contains little contribution from the fluorescence target, we used the emission light from p0 as the background fluorescence. The temporal response function after subtracting the background fluorescence to 8 S-D pairs among above 16 S-D pairs are plotted in Figure 7.6. The hump in a very early region less than 1 ns was probably the background response, which could not be removed by the subtraction.

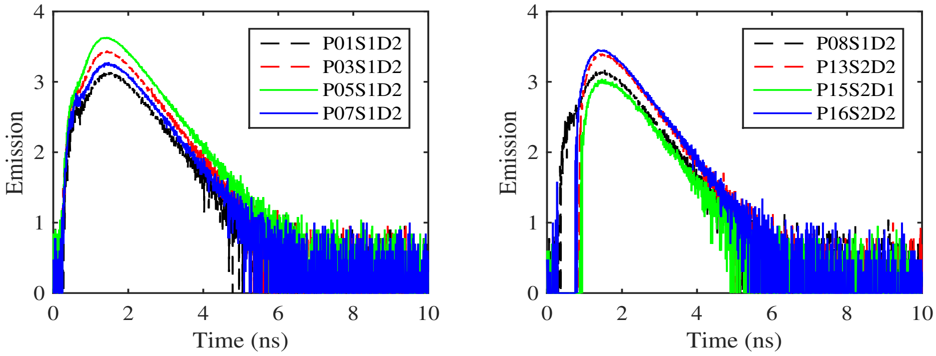

FIGURE 7.6: TPSFs (the logarithm value) with the position of holder at P1, P3, P5, P7, P8, P13, P15 and P16.

Step 2: Likewise we did as before, we choose 20 time points for each S-D pair as the measured time points and perform LM iteration scheme. The results from two different initial guesses are listed in Table 7.2. Furthermore, the initial guess with

$$(X_1^0, X_2^0) = (-5, 10) \in \Gamma \subset \partial\Omega$$

and its responding recovered cube in Step 2 are plotted in Figure 7.7.

TABLE 7.2: The reconstructed results with different initial guesses.

$\mathbf{a}_0^{\text{cube}}$	$\mathbf{a}_{\text{rec}}^{\text{cube}}$	err	$T_{\text{cpu}}(s)/M$
$(-5, 10, 7, 2, 5)$	$(-4.12, 7.72, 17.25, 3.92, 6.1e+4)$	0.1219	3523/85
$(5, 0, 7, 2, 5)$	$(-4.12, 7.72, 17.25, 3.92, 6.1e+4)$	0.1219	7300/182

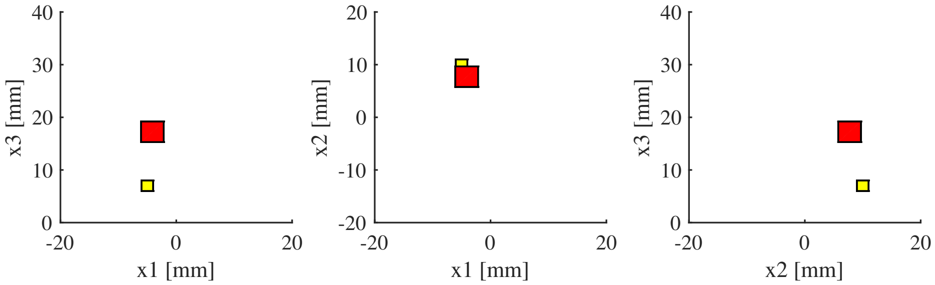

FIGURE 7.7: The initial guess (small yellow cube) and recovery (big red cube) in Step 2.

By the results in Step 1, it can be observed that even for the inversion using detected experimental data, Step 1 is still essential for Step 2. Applying the initial guess with $(X_1^0, X_2^0) \in \Gamma$ for example $(X_1^0, X_2^0) = (-5, 10)$ can accelerate the convergence speed.

Step 3: Setting the recovered cube $\mathbf{a}_{\text{rec}}^{\text{cube}}$ in Step 2 as the initial guess in this step, the recovered cuboid is

$$\mathbf{a}_{\text{rec}}^{\text{cuboid}} = (-5.16, -3.11, 3.83, 12.03, 16.05, 16.34, 5.36e+4). \tag{7.2.2}$$

We compare the recovered cuboid and unknown cylinder target in Table 7.3. Furthermore, the initial guess (the recovered cube in Step 2) and recovered cuboid are plotted in Figure 7.8 and Figure 7.9..

TABLE 7.3: The exact cylinder and recovered cuboid (unit: mm).

Unknown target	Diameter	Length	Depth
Cylinder	2.0	8.0	16.0
Recovery	Width	Length	Depth
Cuboid	2.05	8.21	16.05

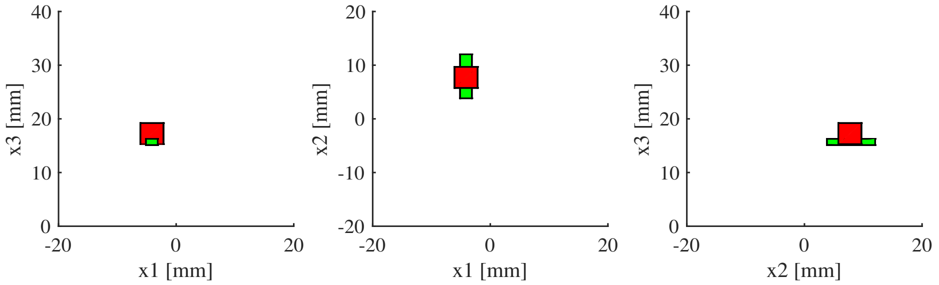

FIGURE 7.8: The initial guess (red cube obtained from Step 2) and recovery (green cuboid) in Step 3.

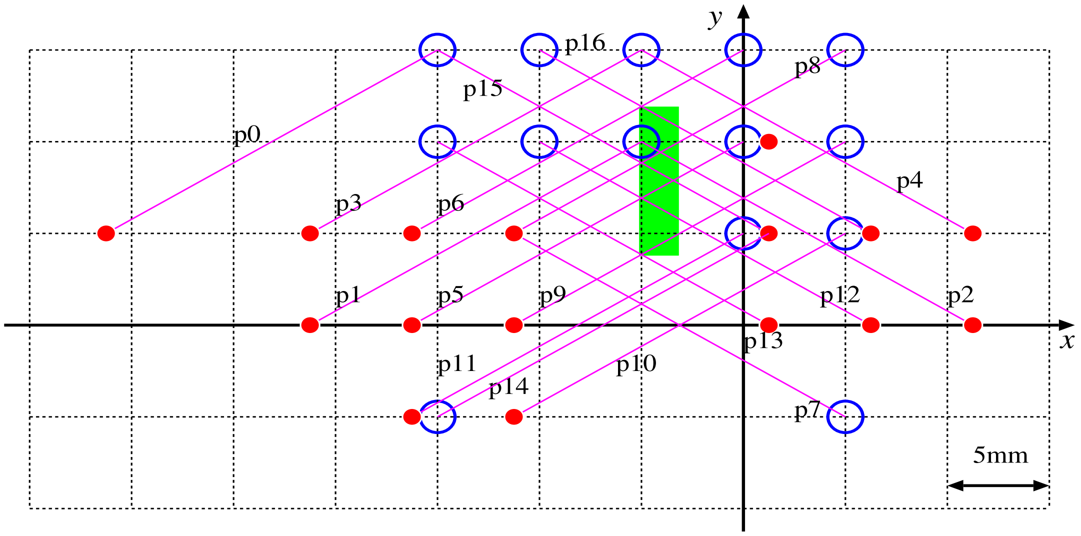

FIGURE 7.9: Schematic figure of measurements on the boundary. Red small disks show sources and blue circles show detectors. The source-detector pairs are denoted by pink lines. The green rectangle shows the position of the reconstructed tube projected on the x-y(x_1-x_2) plane.

Figure 7.7 and Figure 7.8 plotted the initial guesses and recoveries in each steps in our inversion strategy, which clearly showed the process of redefining initial guess such that the algorithm was stable and robust. The position of the recovered cuboid (7.2.2) is what we expected. The exact position of the embedded cylinder in beef is not known. If the cylinder target is parallel to the y-axis as the green rectangle in Figure 7.9, it can be observed from Table 7.3 that the recovered cuboid approximately recover the shape and size of the unknown cylinder target, which shows the effectiveness of our proposed method again.

7.3 Results of Inversion for Beef Experiment II

We consider the inversion using our proposed strategy for another beef experiment, for which the *prior-position* of target is known.

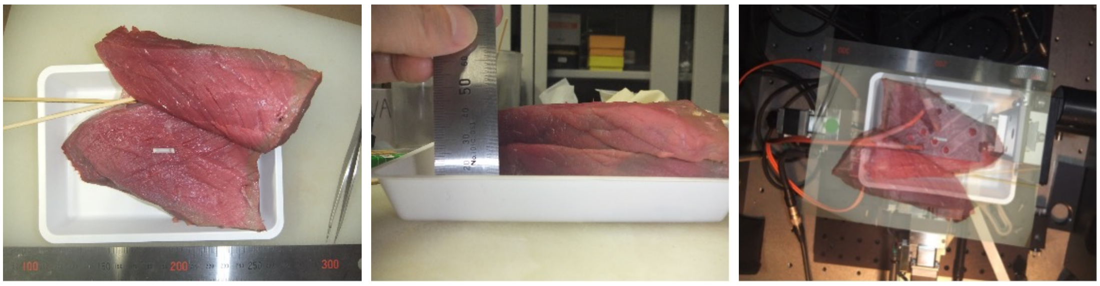

FIGURE 7.10: Beef experiment II: (Left) A cylindrical fluorescence target was inserted in the beef meat. (Middle) The cylinder was embedded at depth about $x_3 = 10$ mm. (Right) Scanned on the meat surface to obtain the boundary measurements.

BEEF EXPERIMENT II: As shown in Figure 7.10, the fluorescence target containing a 1 μM indocyanine green (ICG) solution in 1% Intralipid in a small cylinder (2 mm in diameter and about 8 mm in length) was implanted at depth about $x_3 = 10$ mm from the measurement surface of the meat sample. We setup the stage axis almost parallel to the target. The center position of the target was at about $(x_1, x_2) = (0, 5)$ which is also the position of holder at P13 shown in Table 7.4. The longer axis of target was set aligned to x_1-axis.

The two excitation (S_1 and S_2) and two detection (D_1 and D_2) fibers were aligned with a fiber holder as shown in the left figure of Figure 6.1. The distance between the excitation and the detection points was fixed to 20 mm in our measurement such that the exact locations of excitation and detection corresponding to different positions of holder are also (6.2.5) and (6.2.6), respectively. Then, the holder was scanned on the meat surface by a motorized stage. We used 16-different fiber holder positions as shown in Table 7.4, yielding 64-different source-detector (S-D) pairs.

TABLE 7.4: The positions of the holder in Beef Experiment II (unit: mm).

P01(-15,15)	P05(-20,5)	P09(-10,15)	P13(0,5)
P02(-20,15)	P06(-15,5)	P10(-5,15)	P14(0,0)
P03(-15,10)	P07(-10,5)	P11(-5,10)	P15(0,10)
P04(-20,10)	P08(-10,10)	P12(-5,5)	P16(0,15)

In the experiment, at each iteration in the LM iteration scheme, we will calculate the emission light for $t \in (0, T)$ with $T = 4.78$ ns by (4.1.7), where the IRF q was convoluted with fluorescence lifetime function shown in (4.1.8).

Step 1: Likewise we did as before, we can obtain $\Gamma := (-10, 10) \times (0, 10) \subset \partial\Omega$ by comparing the emission intensities. To reduce the computation, by the numerical results for Example 2 in subsection 6.2.3 we perform the inversion using the measured data given by the following 10 S-D pairs

$$\begin{aligned} &\mathrm{P03S2D2}, \mathrm{P06S1D2}, \mathrm{P06S2D2}, \mathrm{P07S1D2}, \mathrm{P07S2D2}, \\ &\mathrm{P09S2D2}, \mathrm{P12S2D2}, \mathrm{P13S2D2}, \mathrm{P15S2D2}, \mathrm{P16S2D2}, \end{aligned} \tag{7.3.1}$$

which have stronger emission intensities than other S-D pairs such that they should be more close to the unknown target. We note here for instance "P03S2D2" denotes the S2-D2 pair corresponding to the position of holder at P03 in Table 7.4. We used the emission light from P01S1D2 as the background fluorescence, which contains little contribution from the target fluorescence. The TPSFs after subtracting the background fluorescence to above 10 S-D pairs are plotted in Figure 7.11, respectively.

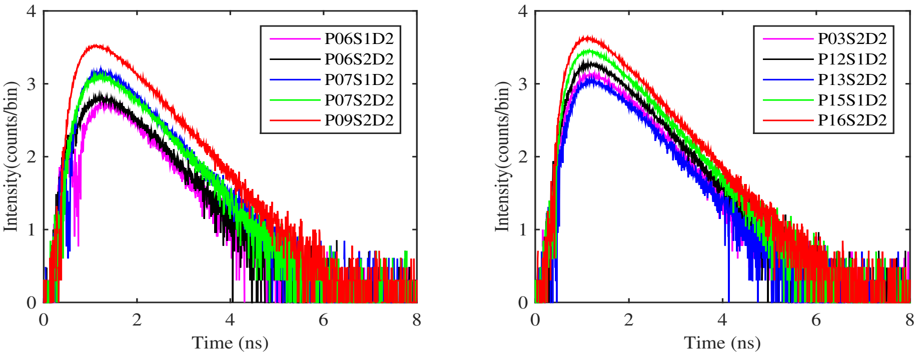

FIGURE 7.11: The TPSFs (the logarithm value) to above 10 S-D pairs given in (7.3.1).

Step 2: We choose 20 time points $\hat{t} := [t_{peak} + 6\Delta t, t_{peak} + 25\Delta t]$ for each S-D pair as the measured time points and perform LM iteration scheme. The result from the initial guess $\mathbf{a}_0^{\text{cube}} = (-2, 7, 10, 3, 1e + 5)$ is

$$\mathbf{a}_{\text{rec}}^{\text{cube}} = (0.49, 5.53, 14.0, 6.53, 1.90e + 4) \tag{7.3.2}$$

with iteration number $J = 83$ and relative error in measurements $err = 8.7e - 2$.

Step 3: Setting (7.3.2) as the initial guess in this step, the recovered cuboid is

$$\mathbf{a}_{\text{rec}}^{\text{cuboid}} = (-5.34, 6.37, 4.39, 6.00, 9.68, 10.48, 8.35e + 4) \tag{7.3.3}$$

with $err = 5.14e - 2$. We compare the recovered cuboid (7.3.3) and unknown cylindrical fluorescence target in Table 7.5 and plot them in Figure 7.12, respectively.

TABLE 7.5: The exact cylinder and recovered cuboid (unit: mm).

Unknown target	Expected center	Diameter	Length	Depth
Cylinder	$(0, 5, 10)$	2.0	8.0	10.0
Recovery	Recovered center	Width	Length	Depth
Cuboid	$(0.52, 5.20, 10.08)$	1.61	11.71	10.08

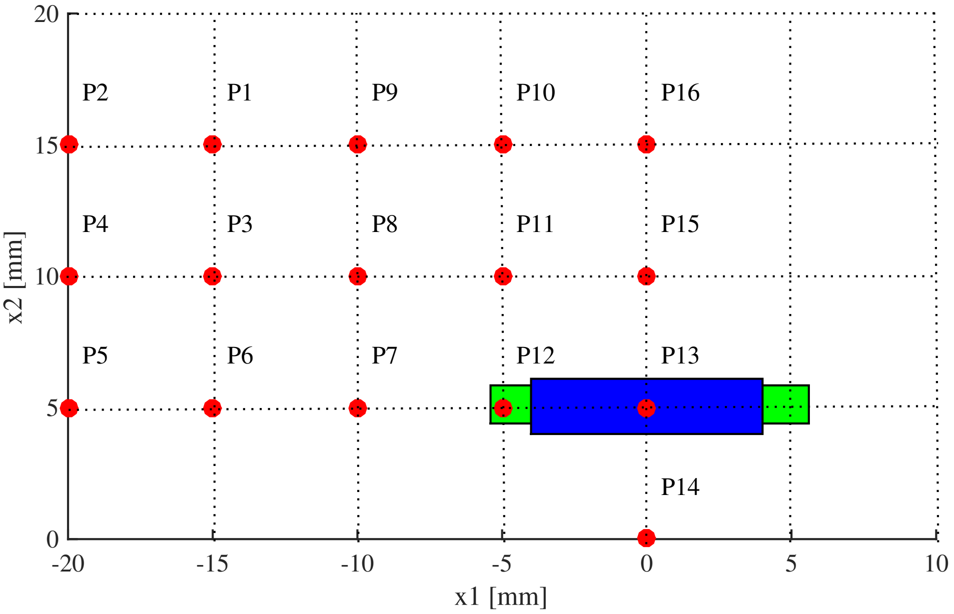

FIGURE 7.12: Red disks show the positions of holder. The blue and green rectangular are the positions of the expected cylinder target and recovered cuboid projected on the boundary plane, respectively.

By Table 7.5 we can see that the center and depth of the unknown cylindrical fluorescence target can be recovered well by $(\frac{a_1^*+b_1^*}{2}, \frac{a_2^*+b_2^*}{2}, \frac{a_3^*+b_3^*}{2})$ and $\frac{a_3^*+b_3^*}{2}$. The shape and size of the target can also be approximated by the recovered cuboid. We can recover the longer axis of target. Although the recovered thickness $b_3^* - a_3^* = 0.8$ mm is thinner than the expected value, it is satisfactory in views of the difficulty of recovering the parameters a_3^* and b_3^* as we analyzed before. We point out that the recovered length $b_1^* - a_1^* = 11.71$ mm is longer than the expected one. In light of the fact that the length of cylinder was stably and correctly recovered in Table 6.7 and Table 6.8, here the reason for the longer recovered length may be attributed to the less number and positions of S-D pairs and measurement noise.

7.4 Chapter Summary

We further confirmed our proposed step-wise algorithm is effective to accelerate the speed of convergence by using real experimental data. We could exactly recover the location of unknown target by assuming cuboid shape. By the results of Chapter 5 and Chapter 6 it is possible to ensure the solvability of inverse problem just using a small number of measurements and the measured data from the S-D pairs near by the target contributed more than others to the inversion. Thus we applied the time-series data from those S-D pairs close to the target as measurement in the inversion.

In our tested examples, we fixed the unknown targets aligned to x_1-axes and x_2-axes, and approximated them using seven unknown parameters. The remained problem to be solved in the future is how to approximate the unknown target using cuboid, if it is not aligned to x_1-axes and x_2-axes or has a general shape. For these cases, we are planing to consider the approximation using the cuboid with some rotation, which implies to identify nine unknowns including the angles of cuboid with horizontal and vertical planes.

Chapter 8

Conclusion and Remark

We first described the diffusion approximation from RTE to linearized DE. The error estimations were established for such a model approximation based on the analytic expression for excitation and emission. We also theoretically analyzed the identifiability of inverse absorption coefficient of flourophore (target).

Then, by using the diffusion equation as a model equation for FDOT, we investigated the inverse problem of FDOT which is to recover the distribution of the absorption coefficient as well as its interface in three-dimensional half space Ω from the measured data at the boundary. Our aims were to provide both theoretical and numerical arguments which could be useful for practical applications. More precisely we not only gave a very efficient numerical inversion strategy for the inverse problem but also some theoretical analysis which can support the numerical arguments and interpret the numerical results. We tried to put everything mathematically logical as much as possible.

By assuming the unknown flourophore (target) has cuboidal shape, we could identify the location of the unknown target by recovering only several unknown parameters, which made the computation fast at each iteration of Levenberg-Marquardt algorithm (LM algorithm). Furthermore, to select a good set of parameters giving the measurement data and find a good initial guess to accelerate the speed of convergence of iteration in LM algorithm, a procedure of narrowing target domains as $\Gamma \mapsto \mathbf{a}_0^{\text{cube}} \mapsto \mathbf{a}_0^{\text{cuboid}}$ was proposed. The results of inversion using simulated data and experimental data showed the efficiency of the proposed strategy. More precisely, our strategy gave successful recoveries and robustness against initial guesses and noise, and even accelerated the convergence speed of LM algorithm.

We gave a precise formula of the analytical solution for our the forward problem of FDOT. Also, we provided the theoretical analysis behind our numerical studies. It can give clear framework to our whole argument and useful concepts, conditions which can orient numerical study and interpret the numerical results. For example the condition for the convergence of LM algorithm and sensitivity analysis.

Finally we give some remarks on our study. Although we assumed that the turbid media in which the light propagates is just a half space in this paper and made use of an analytical solution to the diffusion equation, the proposed algorithm works also in more general cases where diffusion equations must be solved numerically by finite difference method or finite element method [54]. The proposed algorithm can be applied not only to the iterative scheme of LM algorithm but also to other iterative schemes such as the conjugate gradient method and the Gauss-Newton method.

Appendix A

The Gradient of Zero-lifetime Emission

In this Appendix, we provide the gradient $\nabla \widetilde{u}_m$ of $\widetilde{u}_m(\mathbf{a})(x_d, t; x_s)$ with respect to $\mathbf{a} := (a_1, b_1, a_2, b_2, a_3, b_3, P)$ for given detector $x_d \in \partial\Omega$, time t and excitation source $x_s \in \partial\Omega$. By the expression (4.1.13) of $\widetilde{u}_m$, they are given as follows.

$$
\begin{aligned}
\frac{\partial \widetilde{u}_m}{\partial a_1} &= PC(x_{d1}, x_{s1}, x_{d2}, x_{s2}, t) \int_0^t \frac{-\sqrt{t}}{s(t-s)\sqrt{\pi c D}} e^{-\frac{(t(a_1 - x_{s1}) - s(x_{d1} - x_{s1}))^2}{4cDts(t-s)}} \\
&\times \widetilde{u}_2(x_{d2}, x_{s2}, t, s; a_2, b_2)\widetilde{u}_3(t, s; a_3, b_3)ds, \\
\frac{\partial \widetilde{u}_m}{\partial b_1} &= PC(x_{d1}, x_{s1}, x_{d2}, x_{s2}, t) \int_0^t \frac{\sqrt{t}}{s(t-s)\sqrt{\pi c D}} e^{-\frac{(t(b_1 - x_{s1}) - s(x_{d1} - x_{s1}))^2}{4cDts(t-s)}} \\
&\times \widetilde{u}_2(x_{d2}, x_{s2}, t, s; a_2, b_2)\widetilde{u}_3(t, s; a_3, b_3)ds, \\
\frac{\partial \widetilde{u}_m}{\partial a_2} &= PC(x_{d1}, x_{s1}, x_{d2}, x_{s2}, t) \int_0^t \frac{-\sqrt{t}}{s(t-s)\sqrt{\pi c D}} e^{-\frac{(t(a_2 - x_{s2}) - s(x_{d2} - x_{s2}))^2}{4cDts(t-s)}} \\
&\times \widetilde{u}_1(x_{d1}, x_{s1}, t, s; a_2, b_2)\widetilde{u}_3(t, s; a_3, b_3)ds, \\
\frac{\partial \widetilde{u}_m}{\partial b_2} &= PC(x_{d1}, x_{s1}, x_{d2}, x_{s2}, t) \int_0^t \frac{\sqrt{t}}{s(t-s)\sqrt{\pi c D}} e^{-\frac{(t(b_2 - x_{s2}) - s(x_{d2} - x_{s2}))^2}{4cDts(t-s)}} \\
&\times \widetilde{u}_1(x_{d1}, x_{s1}, t, s; a_2, b_2)\widetilde{u}_3(t, s; a_3, b_3)ds, \\
\frac{\partial \widetilde{u}_m}{\partial a_3} &= PC(x_{d1}, x_{s1}, x_{d2}, x_{s2}, t) \int_0^t \frac{-1}{\sqrt{s(t-s)}} \widetilde{u}_1(x_{d1}, x_{s1}, t, s; a_1, b_1) \\
&\times \widetilde{u}_2(x_{d2}, x_{s2}, t, s; a_2, b_2)K_3(0, a_3; t-s)K_3(a_3, 0; s)ds, \\
\frac{\partial \widetilde{u}_m}{\partial b_3} &= PC(x_{d1}, x_{s1}, x_{d2}, x_{s2}, t) \int_0^t \frac{1}{\sqrt{s(t-s)}} \widetilde{u}_1(x_{d1}, x_{s1}, t, s; a_1, b_1) \\
&\times \widetilde{u}_2(x_{d2}, x_{s2}, t, s; a_2, b_2)K_3(0, b_3; t-s)K_3(b_3, 0; s)ds, \\
\frac{\partial \widetilde{u}_m}{\partial P} &= C(x_{d1}, x_{s1}, x_{d2}, x_{s2}, t) \int_0^t \frac{1}{\sqrt{s(t-s)}} \widetilde{u}_1(x_{d1}, x_{s1}, t, s; a_1, b_1) \\
&\times \widetilde{u}_2(x_{d2}, x_{s2}, t, s; a_2, b_2)\widetilde{u}_3(t, s; a_3, b_3)ds,
\end{aligned}
$$

respectively, where $C(x_{d1}, x_{s1}, x_{d2}, x_{s2}, t)$ is a constant for given $x_{d_1}, x_{s1}, x_{d2}, x_{s2}, t$ and $\widetilde{u}_i$, $i = 1, 2, 3$ are defined in (4.1.13) respectively. Here note that by Theorem 4.1, $\widetilde{u}_3(t, s; a_3, b_3)$ is a function both flat at $s = 0$ and $t = s$.

Bibliography

[1] M. Mycek, B. W. Pogue, Handbook of Biomedical fluorescence, Marcel Dekker, New York, 2003.

[2] V. Nitziachristos, C. Tung, C. Bremer, R. Weissleder, Fluorescence-mediated tomography resolves protease activity in *vivo*, *Nat. Med.*, 8, 757–761, 2002.

[3] V. Nitziachristos, J. Ripoll, L. Wang and R. Weissleder, Looking and Listening to light: the evolution of whole-body photonic imaging, *Nat. Biotechnol.*, 23, 313–320, 2005.

[4] M. Rudin, Molecular imaging: basic principles and applications in Biomedical research, 2nd ed., Imperial College Press, London, 2013.

[5] G. Alberti, On local constraints and regularity of PDE in electromagnetics & Applications to hybrid imaging inverse problems, *PhD thesis*, University of Oxford, 2014.

[6] J. Hadamard, Lectures on the Cauchy Problem in Linear Partial Differential Equations, Yale University Press, New Haven, 1923.

[7] A. Kirsch, An Introduction to the Mathematical Theory of Inverse Problems, Vol. 120 of Applied Mathematical Series, Springer-Verlag, New York, 1996.

[8] Ivo W. Kwee, Towards a Bayesian Framework for Optical Tomography, *PhD thesis*, University College London, 1999.

[9] W. Rudin, Principles of mathematical analysis, 3th ed., McGraw-Hill Book Company, Inc., New York-Toronto-London, 1953.

[10] M. V. de Hoop, L. Y. Qiu and O. Scherzer, Local analysis of inverse problems: Hölder stability and iterative reconstruction, *Inverse Problems*, 28, 045001, 2012.

[11] J. Baumeister, B. Kaltenbacher and A. Leitao, On Levenberg-Marquardt-Kaczmarz iterative methods for solving systems of nonlinear ill-posed equations, *Inverse Problems and Imaging*, 4, 335–350 2010.

[12] M. Donald, An algorithm for least-squares estimation of nonlinear parameters, *SIAM Journal on Applied Mathematics*, 11(2), 431–441, doi:10.1137/0111030.

[13] M. Hanke, A regularizing Levenberg-Marquardt scheme with applications to inverse ground- water filtration problems, *Inverse Problems*, 13, 79–95, 1997.

[14] K. Levenberg, A method for the solution of certain non-Linear problems in least squares, *Quarterly of Applied Mathematics*, 2, 164–168, 1944.

[15] E. Zauderer, Partial Differential Equations of Applied Mathematics, John Wiley & Sons, Inc., New York, 1989.

[16] B. Kaltenbacher, A. Neubauer and O. Scherzer, Iterative regularization methods for nonlinear ill-posed problems, Walter de Gruyter GmbH, Berlin-New York, 2008.

[17] C. L. Sun, G. Nakamura, G. Nishimura, Y. Jiang, J. J. Liu and M. Machida, Fast and robust reconstruction algorithm for fluorescence diffuse optical tomography assuming a cuboid target, *J. Opt. Soc. Am. A*, 37(2), 231–239, 2020.

[18] S. Chandrasekhar, Radiative transfer, Dover, New York, 1960.

[19] F. Marttelli, S. D. Bianco, A. Ismaelli and G. Zaccanti, light propagation through biological tissue and other diffusive media: theory, solutions, software, SPIE Press, Bellingham, Washington, 2010.

[20] L. Ryzhik, G. Papanicolaou and J. B. Keller, Transport equations for elastic and other waves in random media, *Wave Motion*, 24, 327–370, 1996.

[21] H. C. van Hulst, Multiple Light Scattering, Vol.1 and Vol.2, Academic Press, New York, 1980.

[22] S. R. Arridge, M. Cope, and D. T. Delpy, The theoretical basis for the determination of optical pathlengths in tissue: temporal and frequency analysis, *Phys. Med. Biol.*, 37(7):1531–1560, 1992.

[23] S. R. Arridge, Optical tomography in medical imaging, *Inverse Problems*, 15, R41-93, 1999.

[24] S. R. Arridge and J. C. Schotland, Optical tomography: forward and inverse problems, *Inverse Problems*, 25, 123010, 2009.

[25] T. Durduran, R. Choe, W. B. Baker and A. G. Yodh, Diffuse optics for tissue monitoring and tomography, *Rep. Prog. Phys.*, 73, 076701, 2010.

[26] H. B. Jiang, Diffuse optical tomography: principles and applications, CRC Press, Taylor & Francis Group, Boca Raton, 2011.

[27] G. H. Bryan, An application of the method of iamges to the conductive heat, *Proc. London Math. Soc.*, 22, 424–430, 1891.

[28] A. H. Hielscher, S. L. Jacques, L. Wang, F. K. Tittel, The influence of boundary conditions on the accuracy of diffusion theory in time- resolved reflectance spectroscopy of biological tissues, *Phys. Med. Biol.*, 40(11), 1957–1975, 1995.

[29] K. R. Ayyalasomayajula and P. K. Yalavarthy, Analytical solutions for diffuse fluorescence spectroscopy/imaging in biological tissues. Part I: zero and extrapolated boundary conditions, *J. Opt. Soc. Am. A*, 30, 537–552, 2013.

[30] R. C. Haskell, L. O. Svaasand, T. T. Tsay, et al, Boundary conditions for the diffusion equation in radiative transfer, *J. Opt. Soc. Am. A*, 11(10), 2727-2741, 1994.

[31] A. Ishimaru, Wave Propagation and Scattering in Random Media, IEEE Press, New York, 1997.

[32] K. M. Yoo, F. Liu and R. R. Alfano, When does the diffusion approximation fail to describe photon transport in random media? *Phys. Rev. Lett.*, 64, 2647-2650, 1990.

[33] S. Keren, O. Gheysens, C. S. Levin and S. S. Gambhir, A comparison between a time domain and continuous wave small animal optical imaging system, *IEEE Trans Med Imaging*, 27, 58–63, 2008.

[34] A. H. Hielscherfl, S. L. acques, L. H. Wang, F. K Tittelt, The influence of boundary conditions on the accuracy of diffusion theory in time-resolved reflectance spectroscopy of biological tissues, *Phys. Med. Biol.*, 40, 1957–1975, 1995.

[35] A. Yodh and B. Chance, Spectroscopy and imaging with diffusing light, *Phys. Today*, 48, 34-40, 1995.

[36] J. C. Baritaux, K. Hassler, and M. Unser, An efficient numerical method for general L_p regularization in fluorescence molecular tomography, *IEEE Trans. Med. Imag.*, 29, 1075–1087, 2010.

[37] D. Han, J. Tian, S. Zhu, J. Feng, C. Qin, B. Zhang, and X. Yang, A fast reconstruction algorithm for fluorescence molecular tomography with sparsity regularization, *Opt. Exp.*, 18, 8630–8646, 2010.

[38] D. Han, X. Yang, K. Liu, C. Qin, B. Zhang, X. Ma, and J. Tian, Efficient reconstruction method for L1 regularization in fluorescence molecular tomography, *Appl. Opt.*, 49, 6930–6937, 2010.

[39] P. Mohajerani, A. A. Eftekhar, J. Huang, and A. Adibi, Optimal sparse solution for fluorescent diffuse optical tomography: theory and phantom experimental results, *Appl. Opt.*, 46, 1679–1685, 2007.

[40] A. Behrooz, H.-M. Zhou, A. A. Eftekhar, and A. Adibi1, Total variation regularization for 3D reconstruction in fluorescence tomography: experimental phantom studies, *Appl. Opt.*, 51, 8216–8227, 2012.

[41] J. F. P.-J. Abascal, J. Chamorro-Servent, J. Aguirre, S. Arridge, T. Correia, J. Ripoll, J. J. Vaquero, M. Desco, Fluorescence diffuse optical tomography using the split Bregman method, *Med. Phys.*, 38, 6275–6284, 2011.

[42] V. Ntziachristos and R Weissleder, Experimental three-dimensional fluorescence reconstruction of diffuse media by use of a normalized Born approximation, *Opt. Lett.*, 26, 893–895, 2001.

[43] N. Ducros, C. D. Andrea, A. Bassi and F. Peyrin, Fluorescence diffuse optical tomography: Time-resolved versus continuous–wave in the reflectance configuration, *IRBM*, 32, 243–250, 2011.

[44] I. Gannot, A. Garashi, G. Gannot, V. Chernomordik and A.Gandjbakhche, *In vivo* quantitative three-dimensional localization of tumor labeled with exogenous specific fluorescence markers, *Appl.Opt.*, 42, 3073–3080, 2003.

[45] S. V. Patwardhan, S.R. Bloch, S. Achilefu and J.P. Culver, Time-dependent whole-body fluorescence tomography of probe bio-distributions in mice, *Opt.Express*, 13, 2564–2577, 2005.

[46] D. Wang, J. He, H. Qiao, X. Song, Y. Fan and D. Li, High-performance fluorescence molecular tomography through shape-based reconstruction using spherical harmonics parameterization, *PLOS ONE*, 9, e94317, 2014.

[47] A. Corlu, R. Choe, T. Durduran, M. A. Rosen, M. Schweiger, S. R. Arridge, M. D. Schnall and A. G. Yodh, Three-dimensional *in vivo* fluorescence diffuse optical tomography of breast cancer in humans, *Opt. Exp.*, 15, 6696–6716, 2007.

[48] J. Lee and E.M. Sevick-Muraca, Three-dimensional fluorescence enhanced optical tomography using referenced frequency-domain photon migration measurements at emission and excitation wavelength, *J.Opt.Soc.Am. A*, 19, 759–771, 2004.

[49] A. B. Milstein, J. J. Stott, S. Oh, D. A. Boas, R. P. Millane, C. A. Bouman and K. J. Webb, Fluorescence optical diffusion tomography using multiple-frequency data, *J. Opt. Soc. Am. A*, 21, 1035–1049, 2004.

[50] V. Nitziachristos, and R. Weissleder, Experimental three-dimensional fluorescence reconstruction of diffuse media by use of a normalized Born approximation, *Opt.Lett.*, 26, 893–895, 2001.

[51] N. Ducros, A. D. Silva, J. M. Dinten et al, A time–domain wavelet–based approach for fluorescence diffuse optical tomography, *Med. Phys.*, 37(6), 2890–2900, 2010.

[52] F. Gao, H. Zhao, L. Zhang, Y. Tanikawa, A. Marjono and Y. Yamada, A self-normalized full time-resolved method for fluorescence diffuse optical tomography, *Opt. Exp.*, 16, 13104–13121, 2008.

[53] M. J. Niedre, R.H. de Kleine, E.Aikawa, D.G. Kirsch, R. Weissleder, and V.Ntziachristos, Early photon tomography allows fluorescence detection of lung carcinomas and disease progression in mice in vivo, *Proc.Nat.Acad.Sci. USA*, 105, 19126–19131, 2008.

[54] Q. Zhu, H. Dehghani, K. M. Tichauer, R. W. Holt, K. Vishwanath, F. Leblond and B. W. Pogue, A three-dimensional finite element model and image reconstruction algorithm for time-domain fluorescence imaging in highly scattering media, *Phys. Med. Biol.*, 56, 7419–7434, 2011.

[55] K. Prieto and G. Nishimura, A new scheme of the time-domain fluorescence tomography for a semi-infinite turbid medium, *Optical Review*, 24, 242–251, 2017.

[56] J. Riley, M. Hassan, V. Chernomordik and A. Gandjbakhche, Choice of data types in time-resolved fluorescence enhanced diffuse optical tomography, *Med. Phys.*, 34(12), 4890–4900, 2007.

[57] S. Lam, F. Lesage and X. Intes, Time domain fluorescent diffuse optical tomography: analytical expressions, *Opt. Exp.*, 13, 2263–2275, 2005.

[58] L. G. Henyey, J. L. Greenstein, Diffuse radiation in the galaxy, *Astrophys. J.*, 93, 70-83, 1941.

[59] M. M. R. Williams, The Milne problem with Fresnel reflection, *J. Phys. A: Math. Gen.*, 38, 3841-3856, 2005.

[60] A. T. N. Kumar, J. Skoch, B. J. Bacskai, D. A. Boas, and A. K. Dunn, Fluorescence-lifetime-based tomography for turbid media, *Opt. Lett.*, 30, 3347–3349, 2005.

[61] A. T. N. Kumar, S. B. Raymond, G. Boverman, D. A. Boas, and B. J. Bacskai, Time resolved fluorescence tomography of turbid media based on lifetime contrast, *Opt. Exp.*, 14, 12255–12270, 2006.

[62] G. Nishimura, Contrast improvement in Indocyanine green fluorescence sensing in thick tissue using a time-gating method, *Biomed. Opt. Exp.*, 10, 1234–1249, 2019.

[63] C. L. Hutchinson, J. R. Lakowicz and E. M. Sevick-Muraca, Fluorescence lifetime based sensing in tissues: a computational study, *Biophys. J.*, 68, 1574–1582, 1995.

[64] M. Machida and G. Nakamura, Born series for the photon diffusion equation perturbing the Robin boundary condition, *J. Math. Phys.*, 61: 013502, 2020.

[65] J. J. Liu, M. Machida, G. Nakamura, G.Nishimura and C.L. Sun, On fluorescence imaging: diffusion equation model and recovery of absorption coefficient of fluorophores, submitted.

[66] J. Mobley and T. Vo-Dinh, Optical properties of tissue, Chapter 1-2, page 2–75, in Biomedical Photonics Handbook. T. Vo-Dinh ed. CRC Press LLC, Boca Raton, Florida, 2003.

[67] G. Nishimura, K. Awasthi and D. Furukawa, Fluorescence lifetime measurements in heterogeneous scattering medium, *J. Biomed. Opt.*, 21, 075013, 2016.

[68] M. S. Patterson and B. W. Pogue, Mathematical models for time resolved and frequency domain fluorescence spectroscopy in biological tissues, *Appl. Opt.*, 33, 1963–1974, 1994.

[69] E. M. Sevick and C. L. Burch, Origins of phosphorence signals reemitted from tissues, *Opt. Lett.*, 19 1928–30, 1994.

[70] M. Sadoqi, P. Riseborough and S. Kumar, Analytical models for time resolved fluorescence spectroscopy in tissues, *Phys. Med. Biol.*, 46, 2725, 2001.

[71] A. Kienle, M. S. Patterson, Improved solutions of the steady-state and the time-resolved diffusion equations for reflectance from a semi-infinite turbid medium, *J. Opt. Soc. Am. A.*, 14(1), 246-254, 1997.

[72] L. Wang, S. L. Jacques, L. Zheng, MCML-Monte Corlo modeling of light transport in multi-layered tissues, *Computer Meth. and Programs in Biomedicine*, 47, 131-146, 1995.

[73] E.Alerstam, T.Svensson, S.A.Engles, Prallel computing with graphics processing units for high-speed Monte Carlo simulation of photon migration, *J. Biomed. Opt.*, 13, 060504, 2008.

[74] K. Furutsu and Y. Yamada. Diffusion approximation for a dissipative random medium and the applications. *Phys. Rev. E.*, 50(5), 3634–3640, 1994.

[75] T. Farrell and M. Patterson, A diffusion theory model of spatially resolved, steady-state diffuse reflectance for the noninvasive determination of tissue optical properties in *vivo*, *Med. Phys.*, 19(4): 879–888, 1992.

[76] J. M. Varah, Pitfalls in the numerical solution of linear ill-posed problems, *SIAM J. Sci. Stat. Comput.*, 4, 164–176, 1983.

[77] J. B. Keller, Inverse Problems, American Mathematical Monthly, 83 107–118, 1976.

[78] A. N. Tikhonov, Regularization of incorrectly posed problems, *Sov. Doklady*, 4, 1624–1627, 1963.

[79] A. N. Tikhonov, Solution of incorrectly formulated problems and the regularization method, *Sov. Doklady* , 4, 1035–1038, 1963.

[80] C. R. Vogel, An overview of numerical methods for nonlinear ill-posed problems, Inverse and Ill-posed Problems (Engl H W and Groetsch C W eds), Academic Press, London, 109–117, 1987.

[81] A. Tarantola, Inverse Problem Theory, Elsevier, 1987.

[82] B. Hoffmann, Regularization of nonlinear problems and the degree of ill-posedness, Inverse Problems: Principles and Applications in Geophysics (Anger G, Gorenflo R, Jochmann H, Moritz H and Webers W, eds), Akademie Verlag, Berlin, 1993.

[83] J. J. Liu, The regularization methods for ill-posed problems and its applications, Science press, in Chinese, 2005.